Measurement of the modulation transfer function with an edge phantom at megavoltage energies

A DISSERTATION PRESENTED
IN PARTIAL FULFILLMENT OF THE REQUIREMENTS
FOR THE DEGREE OF

Dr. rer. nat.

IN THE SUBJECT OF
Physics

TO
The Department of Physics at
TU Dortmund University, Germany
BY

Katharina Loot

2020

©2020 – Katharina Loot

Diese Dissertation wurde der Fakultät für Physik der Technischen Universität Dortmund zur Erlangung des akademischen Grades eines Doktors der Naturwissenschaften vorgelegt.

Erstgutachter:	Prof. Dr. Andreas Block
Zweitgutachter:	Prof. Dr. Bernhard Spaan
Vorsitzender der Prüfungskommission:	Prof. Dr. Shaukat Khan
Vertretung der wiss. Mitarbeiter:	PD Dr. Alex Greilich
Datum der Einreichung der Dissertation:	23.07.2020
Datum der mündlichen Prüfung:	12.11.2020

Measurement of the modulation transfer function with an edge phantom at megavoltage energies

Abstract

The quality of a medical imaging system is determined by how well it transfers diagnostically important information. In terms of spatial resolution, the performance of a system can be objectively characterized by the modulation transfer function (MTF), which describes the transfer of image structures as a function of spatial frequency. MTF measurements at MV energies have previously been conducted with a wide variety of phantoms. The partly contradictory reports raise the question whether the MTF is influenced by the phantom design and, if so, what size of systematic error to expect. This thesis presents MTF measurements on a clinical MV portal imaging system used during radiation therapy. The influences of geometric unsharpness, absorption unsharpness and scatter on the measurement are investigated using Monte Carlo simulations. To quantify the impact of the phantom design on the MTF, a new method is developed that calculates the systematic error in an MTF measurement based on Monte Carlo simulations of the detector input signal. Several edge phantoms are presented which provide high measurement accuracy for a 6 MV photon beam. The results are applicable to all MV imaging devices operated with a comparable beam quality.

Die Qualität eines medizinischen Bildgebungssystems wird dadurch bestimmt, wie gut es diagnostisch relevante Informationen überträgt. In Bezug auf die Ortsauflösung lässt sich ein Systems objektiv durch die Modulationsübertragungsfunktion (MTF) charakterisieren, die die Wiedergabe von Bildstrukturen als Funktion der Ortsfrequenz beschreibt. MTF-Messungen bei MV-Energien wurden in der Vergangenheit mit einer Vielzahl von Phantomen durchgeführt. Die zum Teil widersprüchlichen Ergebnisse werfen die Frage auf, ob die MTF durch das Phantom-Design beeinflusst wird und in welcher Größenordnung der systematische Fehler liegt. In dieser Arbeit werden MTF-Messungen an einem klinischen Portal-Imaging-System in der Strahlentherapie vorgestellt. Die Einflüsse von geometrischer Unschärfe, Absorptionsunschärfe und Streuung auf das Messergebnis werden mithilfe von Monte-Carlo-Simulationen untersucht. Um den Einfluss des Phantom-Designs auf die MTF zu quantifizieren, wird eine neue Methode entwickelt, die den systematischen Fehler in einer MTF-Messung auf der Grundlage von Monte-Carlo-Simulationen des Detektor-Eingangssignals berechnet. Es werden mehrere Phantome vorgestellt, die eine hohe Messgenauigkeit für 6 MV-Photonenstrahlung bieten. Die Ergebnisse sind auf alle MV-Bildgebungssysteme mit einer vergleichbaren Strahlqualität anwendbar.

Publication related to this work

Loot K, Block A. "Technical Note: Accuracy of MTF measurements with an edge phantom at megavoltage x-ray energies." *Medical Physics.* 2019;6:163. doi:10.1002/mp.13843.

Acknowledgments

I would first like to thank Prof. Dr. Andreas Block, my supervisor and mentor of the last years. I am glad we met at the crossroads in Vienna, many years ago.

In addition, I want to thank Prof. Dr. Bernhard Spaan for agreeing to be my second referee, as well as Prof. Dr. Manfred Bayer for providing valuable feedback and support.

My special thanks go to Dr. Ralf Rohn, along with the entire radiation therapy team at Klinikum Dortmund, whom I have had the great fortune to join. Without the close connection to clinical work, this work would not only have been impossible, but also meaningless.

The dedication of this thesis is split four ways:

To my mother,
for the confidence
she sowed in me.

To my colleagues at ISP,
who have taught me much more
than they can possibly
imagine.

To Sedef,
the kindest and
most lovable creature
I know.

And to him,
who has stuck with me
until the very end.

Contents

List of Abbreviations

AMFPI ..... active matrix flat-panel imager
DIS ..... detector input signal
EPID ..... electronic portal imaging device
ESF ..... edge spread function
FFF ..... flattening filter free
HVL ..... half value layer
kV ..... kilovoltage
LSF ..... line spread function
LSI ..... linear shift-invariant
MC ..... Monte Carlo
MLC ..... multi-leaf collimator
MTF ..... modulation transfer function
MU ..... monitor units
MV ..... megavoltage
NEM ..... noise-equivalent modulation
NPS ..... noise power spectrum
OTF ..... optical transfer function
PDD ..... percentage depth dose
PSF ..... point spread function
PTF ..... phase transfer function
ROI ..... region of interest
SID ..... source-to-imager distance
SNR ..... signal-to-noise ratio
SSD ..... source-to-surface distance

1

Introduction

There is no denying that cancer is a leading cause of death worldwide. On the other hand, the scientific progress made over the last decades has ensured that the outlook for cancer patients is brighter today than it ever has been. And while we are far from possessing a cure for all kinds of cancer, at the same time we are closer to this goal than ever before. Cancer has been called the "Emperor of All Maladies", a tribute to its ever-changing nature, ever-adapting strategies, relentless warfare. [1] The genetic diversity of cancer is countered with an ensemble of treatment modalities, including surgery, chemotherapy - and radiation therapy.

Radiation has the potential to chemically break bonds in a cells DNA through the creation of highly reactive radicals in the intracellular material. The cell will lose the ability to reproduce, which eventually results in cell death. [2] As this affects all cells, the art of radiation therapy lies in the balance between tumor control and injury to normal tissue. Many, if not most, technological developments in the field are driven by the desire to reduce the radiation-induced morbidity. If successful, this would allow an escalation of the dose to the tumor and thereby an increase in tumor control probability. [3]

The first application of x-rays for cancer treatment took place mere months after their discovery by Röntgen in 1895. According to historical sources, the equipment included sheet lead from a Chinese tea chest to protect the healthy tissue. [4] Over the decades, the technological advances in the field have been enormous. Today, most radiation therapy treatments use high-energy photons delivered by a linear accelerator. The beam

quality, beam directions, shape and intensity profiles of the treatment fields are based on 3D computed tomography (CT) images, possibly supplemented by other imaging modalities. Organs at risk in proximity to the tumor are shielded with sub-millimeter accuracy using multileaf collimators (MLC). Modern accelerators can produce a high-intensity output (FFF beam), which reduces beam-on time and thereby intra-fractional organ motion. Then there were important developments on the software side, such as optimization algorithms for intensity-modulated techniques (IMRT and VMAT) or more recently the introduction of Monte Carlo based dose calculation.

Crucial in terms of normal tissue sparing as well as tumor control was the introduction of various imaging techniques into the radiation therapy process (image-guided radiation therapy, IGRT).[5] At the linear accelerator, imaging is used to position the patient with respect to the incoming beam to mimic the initial CT scan. The expected residual setup error is compensated during treatment planning by a setup margin around the delineated clinical tumor volume. If the positioning accuracy increases, the safety margin can be reduced and normal tissue can be spared.

The earliest form of image guidance at the linear accelerator, yet still in use, is portal imaging. It uses the treatment beam as radiation source to acquire a megavoltage (MV) image of the patient anatomy and compare it with the anatomy used for treatment planning. The MV radiation was originally recorded with industrial x-ray films, which were later replaced by electronic portal imaging devices (EPID), nowadays in the form of amorphous silicon flat panel detectors.

Although modern linear accelerators are typically equipped with an additional gantry-mounted kilovoltage (kV) imaging system, which allows for higher soft-tissue contrast while reducing the imaging dose, portal imaging is still used to match bony anatomy and to provide intra-fractional fluoroscopic images during special techniques such as respiratory-gated and stereotactic radiotherapy.[6] In addition, the introduction of complex intensity-modulated treatment fields has found the MV detector with its high spatial resolution and dose linearity to be the perfect tool for pre-treatment quality assurance, such as checking MLC positions and the linear accelerator output (portal dosimetry).[7]

The quality of any medical imaging system is determined by how well it transfers diagnostically important information. In terms of spatial resolution, the performance of a system can be objectively described by the modulation transfer function, which specifies the transfer of image structures as a function of their spatial frequency components. There has never been much investigation into the image quality of MV systems, presumably as they are based in a therapeutic, rather than diagnostic context. For measurements of the modulation transfer function, existing techniques for kV systems were adapted for use with MV radiation. This is generally a sound approach, as the underlying physical concepts are the same. However, the impact of beam quality on the imaging process must be understood to ensure an accurate result.

This thesis discusses the measurement of the modulation transfer function at MV energies using an edge phantom. It demonstrates the challenges imposed by the beam quality and outlines a method to quantify the systematic measurement error arising from the phantom design. It discusses the underlying causes of the systematic error and proposes edge phantom designs for measurements with high accuracy.

2

The modulation transfer function

At the heart of imaging, there is the contrast. In a square wave grating for diagnostic x-ray systems (Fig. 2.1), the contrast is provided by the difference in x-ray interaction between the lead foil and the surrounding PMMA. Where the lead foil is present, the x-ray attenuation is higher, which is depicted by higher grey values in the image. The inherent *object contrast* is based on the physical properties of the material in combination with the characteristics of the x-ray beam. Based on the maximum and minimum photon fluence which exits the object in a region of interest (I_{max} and I_{min}), the contrast can be mathematically expressed as

$$C = \frac{I_{max} - I_{min}}{I_{max} + I_{min}}. \tag{2.1}$$

This definition is also known as Michelson contrast or contrast modulation. [8] It can equally be used to calculate the *image contrast*, in this case based on the maximum and minimum image intensity. The performance of an imaging system is determined by how accurately it is able to reproduce the object, i.e. to transfer the object contrast into an image contrast.

There are a dazzling number of metrics to quantify image quality, but in essence there are two main culprits, noise and spatial resolution, and they both work by decreasing the contrast on the way from object to image. Noise adds random fluctuations to the primary signal, increasing both I_{max} and I_{min}, which effectively dimin-

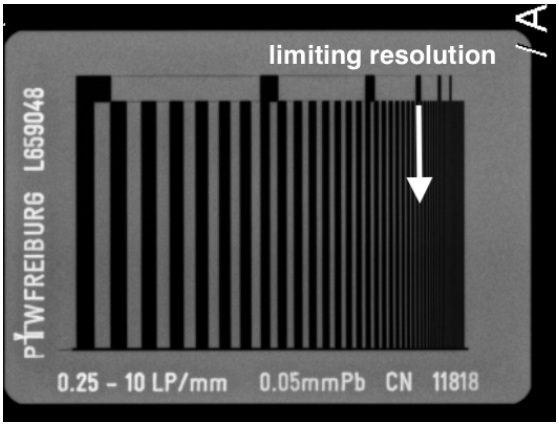

Figure 2.1: Radiograph of a square wave grating, consisting of PMMA and an inlaid lead foil. The limiting resolution marks the highest spatial frequency that can be resolved by the observer.

ishes the image contrast. When spatial resolution is low, photons from object areas of high and low attenuation are mapped onto the same detector area. I_{max} and I_{min} converge, equally diminishing the contrast. The impact of spatial resolution depends on the size of the image detail in question. Broad lines in a square wave grating are easily distinguishable. As the lines draw closer together, all that remains in the image are indistinguishable shades of gray. This is an obvious example to illustrate that the performance of an imaging system must be specified as a function of spatial frequency.

Routine tests used for quality assurance employ square wave gratings to determine the limiting resolution of the system, i.e. the highest spatial frequency present in the grating that can still be resolved by a human observer. Similarly, noise assessment is conducted by the simple metric of the signal-to-noise ratio (SNR), which tracks by how much the useful signal surpasses the background noise. Both the SNR and the limiting resolution reduce the system's performance to a single number. A more detailed description can be achieved by describing the system characteristics in the spatial frequency domain. For noise, this is the noise power spectrum (NPS). For spatial resolution, this is the modulation transfer function (MTF).

The square wave grating can serve as an example to illustrate the MTF (Fig. 2.2). The contrast in the object, defined by the maximum and minimum intensity values, is constant for all spatial frequencies. In the image, the contrast decreases with spatial frequency. The transfer from object to image contrast is described by the MTF.

Amongst other things, the MTF can be used to objectively compare different imaging systems in terms of spatial resolution. Two systems may have equal limiting resolution, i.e. fall below the noise-equivalent modulation (NEM) at the same spatial frequency, but perform very different before this point.

The concepts of transfer function analysis were developed in electronics and communication theory. Before applying them in the context of clinical MV imaging systems, the mathematical tools for a Fourier-based analysis of image resolution are described. Two characteristics are required in order to properly define the modulation transfer function for a system: linearity and spatial invariance.

Figure 2.2: Intensity distribution of a square wave object and image. The modulation transfer function describes the loss in contrast during the imaging process as a function of spatial frequency.

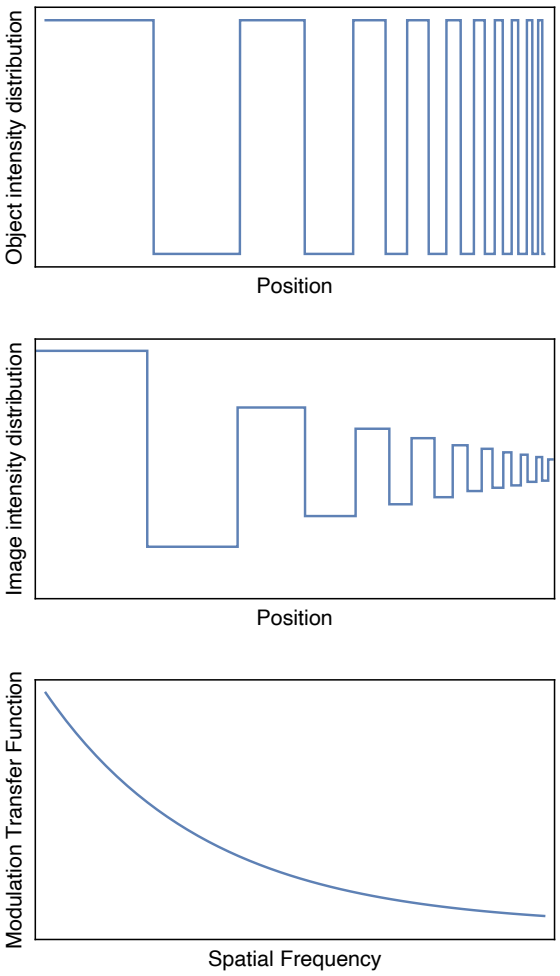

A two-dimensional physical system, such as an imaging system, can be represented by an operator $S\{\}$, which acts on an input function $f(x,y)$ to produce an output function $g(x,y)$:[9]

$$g(x,y) = S\{f(x,y)\} \tag{2.2}$$

The input function $f(x,y)$ can be thought of as a linear combination of weighted and displaced delta functions

$$f(x,y) = \int_{-\infty}^{\infty}\int_{-\infty}^{\infty} f(x',y')\delta(x-x')\delta(y-y')\,\mathrm{d}x'\,\mathrm{d}y' \tag{2.3}$$

using the sifting property of the delta function. If the system behaves linear, such that

$$S\{a_1\cdot f_1(x,y) + a_2\cdot f_2(x,y)\} = a_1\cdot S\{f_1(x,y)\} + a_2\cdot S\{f_2(x,y)\}, \tag{2.4}$$

the functionality of the operator $S\{\}$ can be written as

$$g(x,y) = S\left\{\int_{-\infty}^{\infty}\int_{-\infty}^{\infty} f(x',y')\delta(x-x')\delta(y-y')\,\mathrm{d}x'\,\mathrm{d}y'\right\} \tag{2.5}$$

$$= \int_{-\infty}^{\infty}\int_{-\infty}^{\infty} f(x',y')S\{\delta(x-x')\delta(y-y')\}\,\mathrm{d}x'\,\mathrm{d}y' \tag{2.6}$$

$$= \int_{-\infty}^{\infty}\int_{-\infty}^{\infty} f(x')h(x,y;x',y')\,\mathrm{d}x'\,\mathrm{d}y'. \tag{2.7}$$

The expression $h(x,y;x',y') = S\{\delta(x-x')\delta(y-y')\}$ is called the *impulse response function*.[9] The intelligence drawn from Eq. (2.6) is that the system is fully characterized by its response to a delta function input.

A linear system is said to be shift-invariant if the impulse response function only depends on the difference $x-x'$ or $y-y'$ and not on the individual variables, so that $h(x,y;x',y') = h(x-x',y-y')$. Applied in the context of imaging, the system is shift-invariant if the response to a point source remains the same, regardless of the position of the point source relative to the imaging plane. In this case, Eq. (2.7) can be identified as a convolution integral

$$g(x,y) = \int_{-\infty}^{\infty}\int_{-\infty}^{\infty} f(x',y')h(x-x',y-y')\,\mathrm{d}x'\,\mathrm{d}y' = f(x,y)\star h(x,y), \tag{2.8}$$

where $\star$ denotes the convolution operation.[9]

In switching from the spatial to the spatial frequency domain, i.e. by applying Fourier transform techniques,

the process of convolution in Eq. (2.8) can be replaced by straightforward multiplication:

$$\mathscr{F}(g(x,y)) = \mathscr{F}(f(x,y) \star h(x,y)) \tag{2.9}$$

$$G(\xi,\eta) = F(\xi,\eta) \cdot H(\xi,\eta). \tag{2.10}$$

$F(\xi,\eta)$ denotes the input spectrum, $G(\xi,\eta)$ denotes the output spectrum and $H(\xi,\eta)$, which relates the input and output spectra, is called a *transfer function*.[9] Though no new information has been generated, the simplicity of describing a linear and spatially invariant (LSI) system using Eq. (2.10) is appealing.

In the case of a digital imaging system with a pixelated detector array, the input is given in the sampled and therefore discrete representation $h(x,y) \widehat{=} h(m\Delta_x, n\Delta_y) =: h_{mn}$, with $M \times N$ sampled values and the sampling distances Δ_x and Δ_y. The discrete Fourier transform[10] can be approximated as

$$H_{kl} = \int_{-\infty}^{\infty}\int_{-\infty}^{\infty} h(x,y) e^{-i2\pi(\xi_k x + \eta_l y)} \mathrm{d}x\mathrm{d}y \approx \sum_{m=0}^{M-1}\sum_{n=0}^{N-1} h_{mn} e^{-i2\pi(\frac{km}{M} + \frac{ln}{N})}, \tag{2.11}$$

with the discrete frequency values

$$\xi_k \widehat{=} \frac{k}{M\Delta_x}, \qquad k = 0, 1, \ldots, M, \tag{2.12}$$

$$\eta_l \widehat{=} \frac{l}{N\Delta_y}, \qquad l = 0, 1, \ldots, N. \tag{2.13}$$

The conceptual change from the spatial to the frequency domain is a powerful tool to describe the inherent imaging quality of a system. Applied to a two-dimensional x-ray imaging system, the input consists of the photon distribution created through partial absorption of x-rays by the object. In this context, the impulse response function introduced in Eq. (2.7) is more commonly known as the *point spread function* (PSF).[11] The above relation Eq. (2.8) thus states that the final image $im(x,y)$ is equal to the input function describing the object $obj(x,y)$, convoluted with the point spread function:

$$\mathrm{im}(x,y) = \mathrm{obj}(x,y) \star \mathrm{PSF}(x,y) \tag{2.14}$$

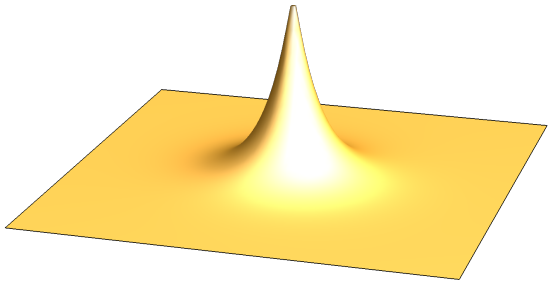

Figure 2.3: The point spread function of an imaging system reveals the system's performance by its deviation from a delta distribution.

An ideal imaging system has an impulse response $\mathrm{PSF}(x,y) = \delta(x,y)$, which produces an image $\mathrm{im}(x,y)$=$\mathrm{obj}(x,y)$ that is an exact replica of the input distribution. The term "point spread function" refers to the ability of a system to form a point image of a point object (Fig. 2.3). The area under the point spread function is defined to be unity:

$$\int_{-\infty}^{\infty}\int_{-\infty}^{\infty} \mathrm{PSF}(x,y)\,\mathrm{d}x\,\mathrm{d}y = 1 \tag{2.15}$$

It follows that the spatial resolution properties of the system will be closely linked to the shape of the point spread function. The convolution operation can be interpreted as taking the finely sampled detector input and creating a set of weighted impulse responses, the superposition of which creates the image (Fig. 2.4). An increased spread of the point spread function will thus ultimately obscure fine details in the image.

A word of caution: The following concept of the modulation transfer function is entirely based on the assumption that the imaging system under investigation behaves linear and spatially invariant, so that the imaging process can be described as a convolution operation. Contrary to the general belief, most imaging systems do not satisfy this condition.[12] An obvious example for non-linearity are screen-film systems, where the optical

density based on the exposure is sigmoid in shape. Furthermore, imaging systems with pixelated detectors are not spatially invariant, because the response to a point source will differ depending on the position of the point source relative to the pixel grid. In order to profit from the benefits of linear systems theory, certain measures need to be taken to transform originally unsuitable systems into LSI systems. For example, the output of a screen-film combination can be linearized, if the measured optical density is related to the exposure by way of a characteristic curve. Furthermore, pixelated systems can be regarded as spatially invariant as long as the sampling aperture is small compared to the size of the detail structures.[13] Linearity and spatial invariance for the imaging system presented in this thesis will be discussed in the following chapter.

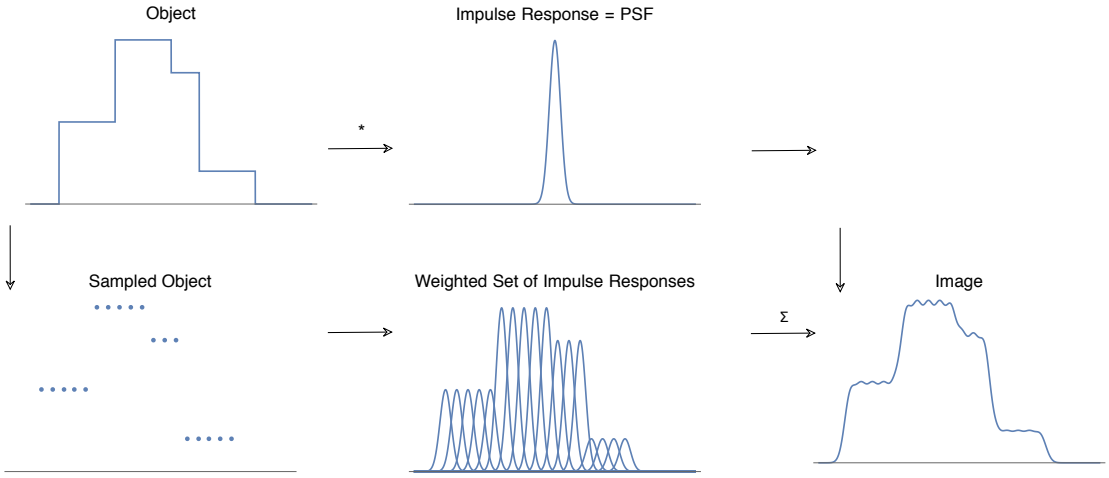

Figure 2.4: Convolution in the imaging process: The image of each discrete point in the object is an impulse response at the conjugate image-plane location, which is weighted by the intensity distribution at the respective point in the object. This is equivalent to a convolution of the object distribution with the impulse response of the system. Adapted from Boreman.[14]

2.3 The modulation transfer function

When Eq. (2.14) is transferred to the spatial frequency domain, we obtain the following expressions:

$$\mathscr{F}(\mathrm{im}(x,y)) = \mathscr{F}(\mathrm{obj}(x,y) \star \mathrm{PSF}(x,y)) \tag{2.16}$$

$$\mathrm{IM}(\xi,\eta) = \mathrm{OBJ}(\xi,\eta) \cdot \mathrm{OTF}(\xi,\eta). \tag{2.17}$$

The normalized Fourier transform of the point spread function is the *optical transfer function* (OTF), which can be separated into its magnitude and phase

$$\mathrm{OTF}(\xi,\eta) = |\mathrm{OTF}(\xi,\eta)| \cdot \mathrm{e}^{-i\theta(\xi,\eta)} \tag{2.18}$$

$$= \mathrm{MTF}(\xi,\eta) \cdot \mathrm{e}^{-i\mathrm{PTF}(\xi,\eta)}. \tag{2.19}$$

The magnitude of the optical transfer function is the *modulation transfer function* (MTF), which is directly related to the resolution power of the system.[14] Combining Eq. (2.19) and Eq. (2.14), we obtain

$$\mathrm{MTF}(\xi,\eta) = |\mathscr{F}(\mathrm{PSF}(x,y))|. \tag{2.20}$$

The MTF is normalized to have unit value at zero spatial frequency. The spatial frequencies ξ and η are expressed in line pairs per millimeter, lp/mm, or simply mm^{-1}.

The complex phase portion, which is called the *phase transfer function*, (PTF), is responsible for phase shifts in the image. It is important in optics, e.g. describing the effects of lens aberrations, because it reveals if the PSF is anisotropic or off-center. For a clinical x-ray imaging system, the phase transfer function is of minor interest, as its contribution is only significant at very high spatial frequencies, which are outside our range of interest.[15]

The degradation of image resolution happens in several steps along the imaging chain, each of which is assumed to be an individual subsystem.[14] To describe such a concatenated imaging system, the overall point spread function can be written as

$$\mathrm{PSF}_{total}(x,y) = \mathrm{PSF}_1(x,y) \star \mathrm{PSF}_2(x,y) \star \ldots \tag{2.21}$$

By moving the discussion to the spatial frequency domain, the influence of the various subsystems can be comfortably separated:

$$\mathrm{MTF}_{total}(\xi,\eta) = \mathrm{MTF}_1(\xi,\eta) \cdot \mathrm{MTF}_2(\xi,\eta) \cdot \ldots \tag{2.22}$$

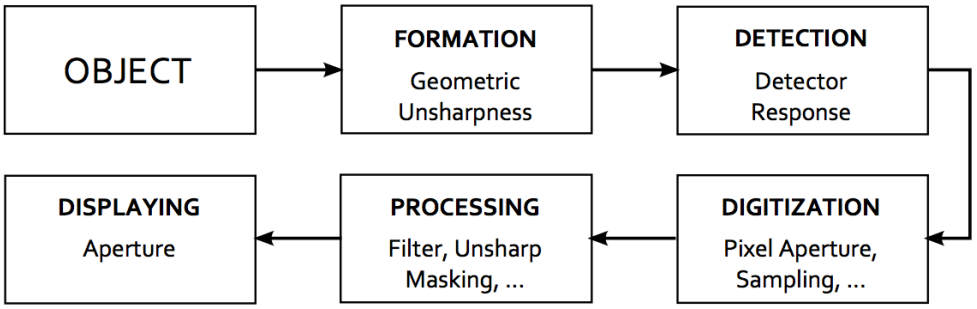

Figure 2.5: The imaging chain, illustrating the influences on the spatial resolution. Each step in the chain can be interpreted as a subsystem with individual transfer function. Adapted from Giger et al. [13]

The main steps in the imaging chain of a digital x-ray system are image formation, detection, digitization, processing and displaying (Fig. 2.5). [13] During image formation, the size and shape of the focal spot, as well as the imaging geometry and the resulting magnification determine the sharpness of detail structures. As the imaging geometry is different for every patient, so is the geometric unsharpness (GU) introduced during this step. The detector response (DR) comprises such effects as x-ray scattering and light diffusion in the detector system, depending on the physical structure of the system. At the digitization stage, the system is influenced by the averaging effect of the sampling aperture (S), as well as the sampling procedure. The latter is expressed by a convolution operation with a comb function that depends on the sampling distances Δx and Δy. The last two steps in the image chain contain influences from post-processing or filtering (F) and the display aperture (D). The overall MTF can be written as

$$\mathrm{MTF}(\xi,\eta) = \left\{ \left(\mathrm{MTF}_{GU}(\xi,\eta) \cdot \overbrace{\mathrm{MTF}_{DR}(\xi,\eta) \cdot \mathrm{MTF}_{S}(\xi,\eta)}^{\mathrm{MTF}_{PRS}\text{: presampled detector MTF}} \right) \star \sum_{m=-\infty}^{+\infty} \sum_{n=-\infty}^{+\infty} \delta\left(\xi - \frac{m}{\Delta x}, \eta - \frac{n}{\Delta y}\right) \right\} \cdot \mathrm{MTF}_{F}(\xi,\eta) \cdot \mathrm{MTF}_{D}(\xi,\eta) \tag{2.23}$$

To measure the intrinsic properties of the detector, guidelines of the International Electrotechnical Commission (IEC) recommend the *presampled* detector MTF (MTF_{PRS}). [16] It includes the detector response (DR) and the effect of the sampling aperture (S). Additional influences such as the imaging geometry or post-processing are deliberately excluded. The sampling stage (convolution with comb function) is also excluded from the MTF measurement, as it can potentially corrupt the measurement result (more on this in Section 2.5.1). Even though it is not always explicitly stated, measurements reported for digital x-ray imaging systems generally refer to the presampled detector MTF.

2.4 Measuring the modulation transfer function

The MTF was motivated in two different ways, first as the loss in contrast from object to image, then as the spatial frequency spectrum of the impulse response. Both ways can be and have been used to measure the MTF.

2.4.1 Sine and square wave response

The earliest measurements of the modulation transfer function, although it did not yet go by that name, can be traced back Selwyn in the late 1940s.[17] In his optical laboratory, Selwyn found that the photographic image of a sine wave bar pattern was always another sine wave bar pattern of the same spatial frequency, but with reduced contrast and adjusted spatial phase. Selwyn stated that a system's limiting resolution can be determined by finding the intersection of the sine wave response with a frequency-dependent threshold curve showing the least detectable modulation. His research can be seen as the first measurement of the optical transfer function. The changes in modulation and phase would these days be called the modulation and phase transfer functions.

For an x-ray system, it is practically impossible to manufacture a sine wave grating with the required accuracy, so square wave bar patterns are used instead.[18] For this purpose, Coltman related the square wave response $r(\xi)$ to the desired sine wave response $R(\xi)$ by what is these days known as Coltman's Formula[19]:

$$R(\xi) = \frac{\pi}{4}\left[r(\xi) + \frac{r(3\xi)}{3} - \frac{r(5\xi)}{5} + \frac{r(7\xi)}{7} + \dots\right] \tag{2.24}$$

While theoretically sound, application of the formula requires the measurement of several higher harmonics to achieve a good estimate, which can be difficult for high resolution imaging systems.[20] It also requires a large number of test patterns, as each frequency that is to be measured must have a set of additional bar patterns for the higher harmonics. For this reason, we mainly see studies in which the modulation transfer function is measured at a handful of frequencies and subsequently interpolated. Especially the low frequency range tends to be neglected.[21] Despite these disadvantages, the bar pattern certainly has a legitimacy as a simple test tool for quality assurance and is for that purpose commercially available.[22] As MV imaging systems tend to possess a low limiting resolution, they are potentially suited for analysis with a bar pattern. This technique was described in a publication by Gopal and Samant, which can serve as a guideline for the interested reader.[23]

2.4.2 Spread function methods

The sine wave response finally received the name *modulation transfer function* around 1962 from Kurt Rossmann, a pioneer in radiologic imaging research.[24,25] Rossmann was familiar with linear systems theory and added a sound mathematical framework to the formerly empirical analysis of contrast, image sharpness and

noise. He introduced several fundamental analysis tools, most notably the point spread function, the line spread function, the modulation transfer function and the Wiener spectrum.[11,26] Based on his ideas, the MTF can be determined with a simple edge or slit phantom.

The obvious method to measure the MTF according to Eq. (2.20) is to use a point source, mathematically represented by a two-dimensional delta function

$$\mathrm{obj}(x, y) = \delta(x, y), \tag{2.25}$$

in which case the MTF can be extracted from the image of the point source as

$$\begin{aligned} \mathrm{MTF}(\xi, \eta) &= |\mathscr{F}(\mathrm{PSF}(x, y))| && (2.26)\\ &= |\mathscr{F}(\delta(x, y) \star \mathrm{PSF}(x, y))| && (2.27)\\ &= |\mathscr{F}(\mathrm{im}(x, y))|. && (2.28) \end{aligned}$$

In practice, it is typically inconvenient to employ a point source, as the resulting photon fluence is very small.[27] Instead, we measure the response to a line source, given by a delta function in x-direction and a constant in y-direction:

$$obj(x, y) = \delta(x)1(y). \tag{2.29}$$

This allows us to obtain the MTF in the direction perpendicular to the orientation of the line source, in this case the x-direction:

$$\begin{aligned} \mathrm{MTF}(\xi) &= |\mathscr{F}(\delta(x)1(y) \star \mathrm{PSF}(x, y))| && (2.30)\\ &= |\mathscr{F}(\mathrm{LSF}(x))|. && (2.31) \end{aligned}$$

The photon distribution provided by a slit phantom acts as a line source. The profile of the intensity distribution (Fig. 2.6a) perpendicular to the line, is called the *line spread function* (LSF).

Alternatively, a step function input

$$\mathrm{obj}(x, y) = \mathrm{H}(x)1(y) \tag{2.32}$$

can be created by means of an edge phantom. Based on the intensity distribution of the edge image (Fig. 2.6b), the profile perpendicular to the edge transition is defined as the *edge spread function* (ESF). By definition, the

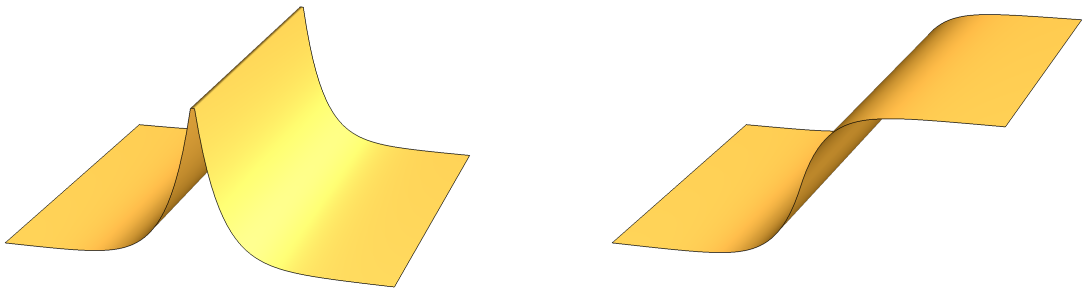

(a) Intensity distribution of a slit image.

(b) Intensity distribution of an edge image.

Figure 2.6: The MTF can be calculated from a line or edge spread function, extracted from the image of a slit or edge phantom.

LSF is the spatial derivative of the ESF:

$$\mathrm{ESF}(x) = \mathrm{H}(x)1(y) \star \mathrm{PSF}(x,y) = \int \mathrm{LSF}(x)\,\mathrm{d}x. \tag{2.33}$$

We obtain the MTF similar to Eq.(2.30), with an additional differentiation step:

$$\mathrm{MTF}(\xi) = \left| \mathscr{F}\left(\frac{\mathrm{d}}{\mathrm{d}x}\mathrm{ESF}(x) \right) \right| \tag{2.34}$$

$$= |\mathscr{F}(\mathrm{LSF}(x))|. \tag{2.35}$$

Both slit and edge method have been used with x-ray imaging systems. The obvious difference is the additional differentiation for the edge method. For the discrete image data, this step is performed with a finite-element technique which approximates the true derivative by the slope between neighboring pixels. The error introduced by this approximation can be corrected by dividing the MTF by the frequency response of the finite-element differentiation (see page 47).[28] Differentiation also increases the noise in the image data, which leads to a noisier MTF and can potentially introduce a bias error (more on this in Section 4.1.2). However, this disadvantage can be overcome by acquiring edge images with a higher exposure or averaging several edge images, both of which reduce the noise level in the ESF.[29]

MTF measurements with a slit phantom pose several challenges: Firstly, the slit must be precisely aligned with the central axis of the radiation, otherwise the photon fluence which leaves the phantom is too small to be detected. This requires an iterative procedure with several test images prior to the measurement. Poor alignment will introduce an error in the MTF.[30] The slit phantom only acts as a line source if the width of the slit is small compared to the FWHM of the detector response. In general, a correction for the slit width needs to be applied. This requires knowledge of the exact slit width, e.g. through film measurements or simulations.[31,32] Another

major concern is the normalization of the resulting MTF. By definition, the zero frequency component of the MTF is defined as the integral over the LSF:

$$\mathrm{MTF}(0) = |\mathscr{F}(\mathrm{LSF}(x))|_{\xi=0} = \int_{-\infty}^{\infty} \mathrm{LSF}(x)\,\mathrm{d}x \tag{2.36}$$

If there is an offset in the LSF, the Fourier transform passes this offset on to MTF(0), the DC component. As the MTF is scaled to its zero frequency value, the offset will bias the MTF at all other frequencies. This means that the measurement must produce an accurate estimate for the LSF integral. Problems arise from three sides: Firstly, the signal can be influenced by radiation that is transmitted through the blocks forming the slit phantom. This will prevent the LSF tails from dropping to zero and therefore requires subtraction of a closed-slit image.[33] Secondly, if the LSF has a longer range than the region of interest used for MTF analysis, the resulting truncation error affects the LSF integral in a similar fashion.[34,35] Thirdly, the noise in the signal can make it difficult to estimate the true LSF baseline.[33]

Measurements with a slit phantom can produce accurate results, but the procedure is challenging and prone to errors. On the other hand, the edge method has been shown to be robust against phantom misalignment by several centimeters[30] and is considered to be superior for measuring the low-frequency response.[36] These findings went into the IEC 62220-1 report, which recommends the edge method for MTF measurements at kV energies.[16] As will become evident from the literature review, no consensus has yet been formed for MTF measurements in the therapeutic energy range. Based on the above considerations however, the experiments and simulations presented in this thesis were entirely focused on the edge method.

2.5 Influences on the measurement

This thesis will investigate the accuracy of MTF measurements at MV energies which are conducted with an edge phantom. Below follows a brief summary of factors which might influence MTF measurements and will appear repeatedly during this work.

2.5.1 Sampling and Aliasing

The size of the pixel aperture is an important detector characteristic. Modern radiotherapy employs EPIDs that are based on active matrix flat panel imaging (AMFPI) technology.[37] For these systems, the size of a detector element and thereby the sampling distances are finite. The incoming photon fluence is spatially averaged over the area of one pixel. Expressed in one dimension, spatial averaging over a detector element of width Δ is equivalent to convolving the input $\mathrm{obj}(x)$ with a rectangular function of width Δ:

$$\mathrm{im}(x) = \mathrm{obj}(x) \star \mathrm{rect}(x/\Delta) \tag{2.37}$$

Transferred to the spatial frequency domain, the frequency filter produced by the pixel aperture is a sinc function (Fig. 2.7) with the first zero at $\xi_0 = 1/\Delta$:

$$\mathrm{MTF}_S(\xi) = |\mathrm{sinc}(\pi\xi\Delta)| = \left|\frac{\sin(\pi\xi\Delta)}{\pi\xi\Delta}\right| \tag{2.38}$$

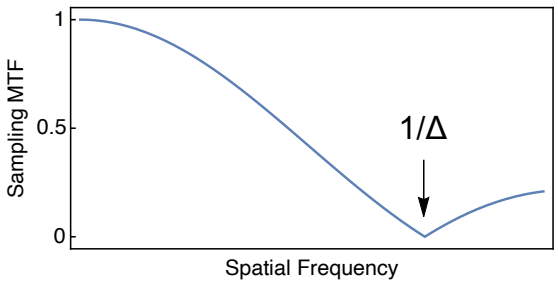

Figure 2.7: Sinc function MTF for detector elements (pixels) of width Δ, insert arrow. At $\xi_0 = 1/\Delta$, the pixel aperture extends over one period of the signal, so that the contrast modulation is entirely extinguished

On a related note, the finite size of the detector elements also affects the data acquisition in terms of sampling. If we assume negligible dead space between adjacent pixels, i.e. if the pixel pitch coincides with the pixel aperture Δ, the incoming signal can only be sampled reliably for frequencies below the Nyquist limit ξ_{Ny}:

$$\xi < \frac{1}{2\Delta} = \xi_{Ny}. \tag{2.39}$$

For the MV detector mentioned in this thesis (Varian PortalVision aS1200) with a pixel pitch of 0.336 μm, the

Nyquist frequency is $1/2\Delta$=1.49 mm^{-1}.

The Nyquist condition states that an unambiguous reconstruction of a frequency component requires more than two samples per cycle. If the signal is undersampled, any frequency $\xi \geq \xi_{Ny}$ will be misinterpreted and fit into the region $0 \leq \xi < \xi_{Ny}$. The resulting image artefact is called *aliasing*.[38]

Aliasing breaks the spatial invariance of the system. Section 3.3.1 describes the steps taken to artificially increase the Nyquist frequency, so that the entire frequency range present in the incoming signal can be sampled without aliasing.

2.5.2 Geometric Unsharpness

The term *geometric unsharpness* refers to the loss of definition in a radiographic image caused by the finite size f of the radiation source (instead of an ideal point source).[39] Due to the extrafocal radiation, a single point in the object is projected onto different positions in the detector plane (Fig. 2.8a). Based on the imaging geometry,

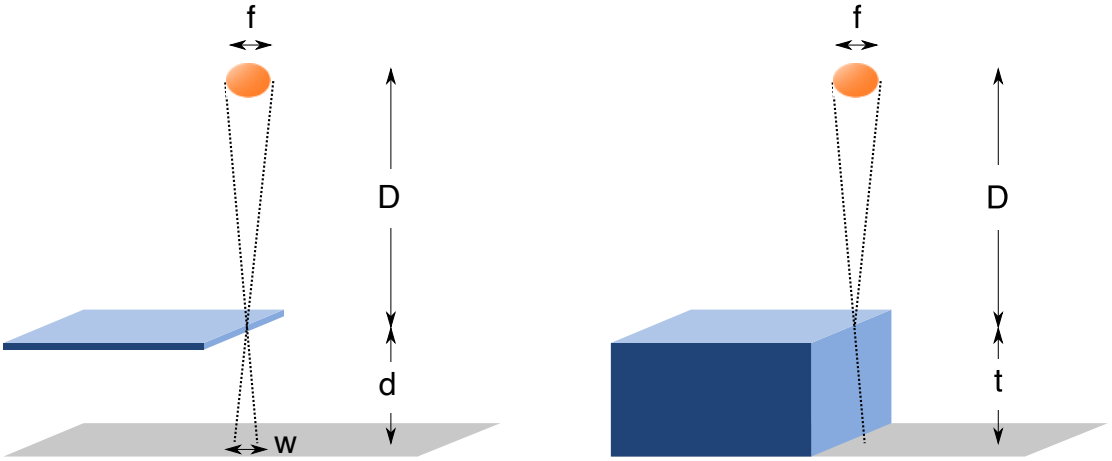

(a) The edge of a thin, radiopaque plate, suspended in mid-air, appears as a penumbra over the width w in the edge image. Source size exaggerated for illustration.

(b) The penumbra for a solid edge phantom, where the entrance plane is at a distance t (=phantom thickness) from the detector, has not yet been investigated.

Figure 2.8: Geometric unsharpness is introduced when a point in the object is projected onto different points in the image, depending on the size of the radiation source. It is more severe when the distance between object and detector is large.

the geometric unsharpness w caused by a uniform source size f can be calculated as

$$w = f \cdot \frac{d}{D}, \tag{2.40}$$

where the source-object distance D and the object-detector distance d are large compared to the thickness t of the object.[39] The edge of an object appears as a linear transition from low to high image intensities, called

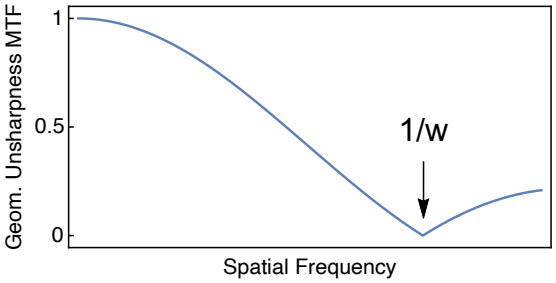

Figure 2.9: The MTF component for geometric unsharpness is a sinc function. At $\xi_0 = 1/w$ spatial frequency, the width of the penumbra equals the width of one line pair.

the *penumbra*. The standard operating procedures for clinical x-ray imaging avoid geometric unsharpness by positioning the patient as closely as possible to the detector (or vice versa) and maximizing the source-to-imager distance (SID=$D + t + d$). The same applies to the acquisition of test images for quality assurance, where the test object is placed in direct contact with the detector to eliminate geometric unsharpness. [40]

Typical source sizes for linear accelerators are in the range of 1 - 2 mm [41], compared to effective focal spot of 0.3 - 1.2 mm [42] in diagnostic radiography systems. Extrafocal radiation acts on the imaging signal in the same way as averaging the signal with a rectangular window of width w. Consequently, the MTF of geometric unsharpness, MTF_{GU}, is also represented by a sinc function (Fig. 2.9):

$$\mathrm{MTF}_{GU}(\xi) = |\mathrm{sinc}(\pi\xi w)| = \left|\frac{\sin(\pi\xi w)}{\pi\xi w}\right|. \tag{2.41}$$

Rossmann and Lubberts have validated this formula for kV imaging systems. [39] Whether the above description is equally applicable to MV systems will be investigated during the course of this work. The size of the radiation source is seldom measured for a linear accelerator and there are conceptual differences compared to the focal spot of an x-ray tube. In addition, the special case of geometric unsharpness for a solid edge phantom will be considered, which is in direct with the detector ($d = 0$) but whose entrance plane is at the distance t from the detector surface (Fig. 2.8b).

2.5.3 Absorption unsharpness

The radiation beam of a linear accelerator is divergent, with the field size being defined at the isocenter. Imaging with a divergent beam can introduce unsharpness, because the divergence causes variations in the absorption length (Fig. 2.10). This unsharpness was termed *absorption unsharpness*. [43,44] Although the term itself is seldom used, the effect is well known, e.g. as the cause of the heel effect in an x-ray tube. In contrast to geometric unsharpness, it is not the distance from the detector which determines the unsharpness, but the shape of the object in relation to the divergence angle of the beam. [40] A cone with the edges parallel to the diverging beam will be free from absorption unsharpness, while the outline of an object with uniform thickness will appear

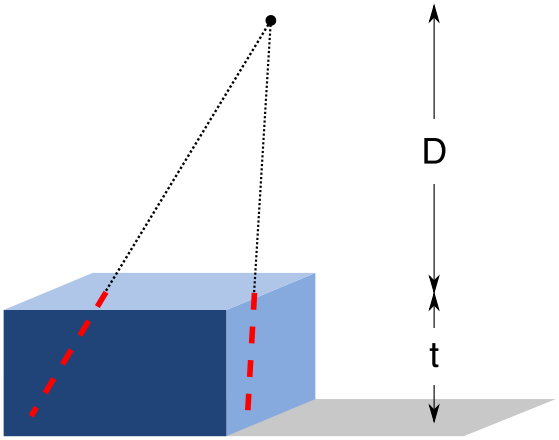

Figure 2.10: Divergent x-rays passing through an edge phantom of uniform thickness might introduce a trend in the signal due to different absorption lengths.

blurred.

For an edge phantom, there is the possibility of a decline in signal intensity for areas further away from the central axis. However, the MTF is calculated from the central image region only. Whether the variations of absorption length within the phantom are relevant depends on the beam divergence angle and thereby on the relation between the size of the central image region and the source-to-detector distance. The role of absorption unsharpness in MTF measurements has not yet been investigated and will be a subject of discussion in the course of this work.

2.5.4 Scatter

In the photon energy range employed in radiotherapy, the relevant x-ray interaction processes are photoelectric absorption, incoherent scatter due to the Compton effect and pair production (Fig. 2.11). The photon beam of a linear accelerator will inevitably generate secondary radiation. It has been shown that the role of electrons in forming the MV image is minor [45,46], so that the secondary radiation consists mainly of Compton scattered photons and bremsstrahlung.

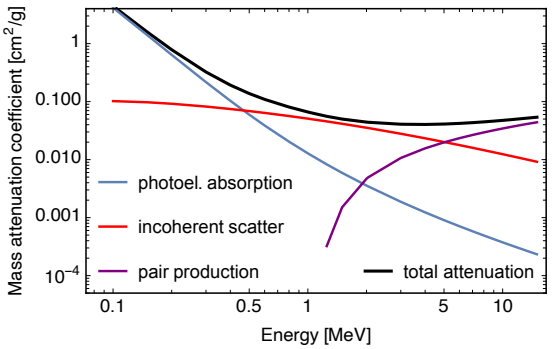

Figure 2.11: Relative probability of x-ray interaction as a function of photon energy for a Tungsten absorber, showing the therapeutic energy range. Data according to NIST database. [?]

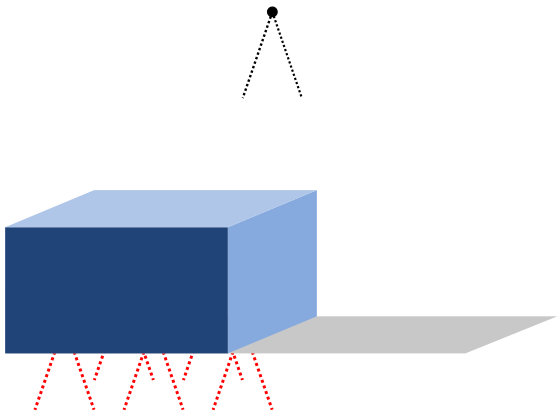

Figure 2.12: Interaction of the radiation with the edge phantom introduces secondary radiation, which can potentially reach the detector.

Scatter enters the imaging chain as an additional signal, not as a convolution operation. As it is created within the phantom itself, it is mainly present in the area below the phantom, but may also extend into the open field due to its angular distribution (Fig. 2.12). The implications of scatter in MTF measurements have been described in an important publication by Neitzel et al., which discussed the impact of edge phantom thickness on MTF measurement accuracy at kV radiation quality (20-120 keV).[47] It showed that the scatter distribution behind an edge phantom resembles a step function in the opposite direction of the primary radiation, with overall lower intensity and a more gradual slope (Fig. 2.13). From this work followed the IEC 62220-1 recommendation to use a 1 mm tungsten edge phantom for MTF measurements at kV energies.[16]

The model developed by Neitzel et al. describes the interaction of x-ray radiation with a homogeneous, thin edge phantom. The radiation that reaches the detector is either unattenuated incident radiation with intensity I_0, transmitted radiation I_t or scattered radiation I_s (Fig. 2.13). Scatter can be modeled as rotationally symmetric scatter point spread functions PSF_{scat} which emanate from every point of the edge phantom, normalized so that

$$\int_0^\infty 2\pi r \cdot \mathrm{PSF}_{scat}(r)\,\mathrm{d}r = S, \tag{2.42}$$

with the scatter fraction $S = I_s/I_0$ and the fraction of attenuated radiation $A = 1 - I_t/I_0$.[48,49] When this photon distribution is used as a detector input signal, it can be shown that the measured MTF is larger than the actual detector MTF at all spatial frequencies:

$$\mathrm{MTF}_{det}(\xi) = \left(1 - \frac{S}{A}\right) \cdot \mathrm{MTF}_{meas}(\xi). \tag{2.43}$$

The model has been experimentally validated for standard radiation qualities (RQA). There was good agreement for the IEC-specified beam qualities RQA 3 to RQA 7, while measurements with the higher-energetic

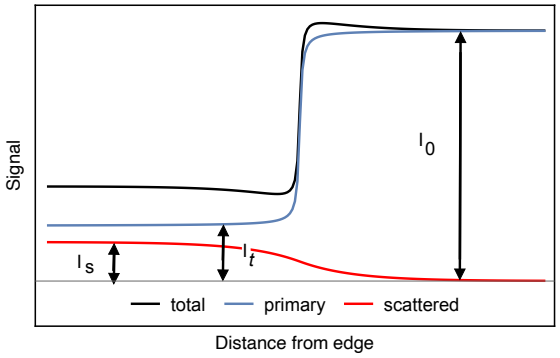

Figure 2.13: The intensity distribution behind the edge phantom is described by the ratio of primary to secondary input signal.

RQA 9 returned even greater values for the measured MTF than predicted with the model. There have been no reports of similar investigations at MV beam qualities. We can expect significantly higher scatter fractions due to the prevalence of Compton interaction, as well as photons being predominantly emitted in forward direction. In addition, MTF measurements at higher energies are typically carried out with several centimeter thick edge phantoms to achieve an adequate level of attenuation, while this model assumes a phantom between 0.1 mm and 1.0 mm in thickness.

Part of this work will be to characterize the scattered radiation emitted by an edge phantom at MV energies and determine the influence on the measured MTF.

2.6 Literature review

An overview of all publications featuring MTF measurements on MV systems up to July 2020 can be found on pages 29 and 30. Most of the reports focused on the development of new detector systems and merely employed the MTF as a tool to demonstrate the improvements in image quality. However, some publications contained additional insights concerning the MTF measurement itself. These are discussed in the following review to unearth the open questions that remain to be explored.

The fist MTF measurements of a medical x-ray system were conducted by Kurt Rossmann in the Kodak Research Laboratories. [24,20] The system operated with a diagnostic beam quality of 70 kVp and 3 mm aluminium filter (HVL: 3mm Al). Rossmann formed thin slits made from uranium (0.9 mm thickness) and platinum (2 mm thickness). His reports explicitly express the concern that the phantom may introduce geometric and absorption unsharpness. Thus, it was suggested that the phantom should be as thin as possible. [50,26,51]

Ronald Droege reported the first MTF measurement of an MV imaging system in 1979. [31,32] He investigated the imaging properties of metal screen-film detectors, which were the most common form of radiation treatment verification at the time. Droege had observed a significant deterioration in image quality as the x-ray energy increased above 1 MeV and suspected the image resolution to be at least partially responsible. [52] In adapting Rossmann's measurements for screen-film systems, Droege experienced the key problems arising from MV beam quality: low absorption of the photon beam by the phantom and a high level of noise in the image. Droege showed that the ratio of peak-to-background signal for a 1 mm thick tungsten phantom can reach more than 100:1 at kV energies, while a tungsten phantom of 1.6 cm thickness only yields a ratio of about 2:1 in combination with MV radiation. Furthermore, the film grain noise in metal screen-film systems increases from around 1 % for kV radiation to 10 % for MV radiation, which hinders the evaluation of the LSF. To counter these effects, Droege used 1.6 cm thick tungsten blocks to form the slit phantom. The increased phantom thickness led to higher x-ray absorption and reduced the overall noise level. [32] Droege advised against increasing the phantom thickness beyond this point, though for practical reasons: The high rising sides of the tungsten blocks would complicate the alignment of the phantom with the beam, as well as partially obscure the radiation source. Droege does not mention the potential influence of geometric and absorption unsharpness - whether it escaped his notice or he thought these influences to be negligible remains unclear.

Some years later, Munro et al. reported an MTF measurement for a similar detector, acquired with a 10.5 cm thick tungsten slit phantom - a six times increase in phantom thickness. [53] Munro found that, while a thick phantom reduces the x-ray transmission through the slit, the background intensity decreases even more strongly (provided backscatter can be eliminated). Therefore, the peak-to-background ratio will actually increase in thicker phantoms. In terms of the phantom design, this study laid the foundation for all MTF measurements on MV

detectors which followed during the next decades. Future works continued to increase the phantom thickness still further, limited only by the more and more cumbersome phantom alignment.

When metal screen-film systems were replaced by digital fluoroscopic systems, Munro et al. published an update which extended the MTF analysis to pixellated imaging systems.[54] A subsampling technique restored the spatial invariance of the imaging system and allowed the determination of the pre-sampled MTF without aliasing effects (more on this in Section 3.3). Munro's method became the guideline for measuring the MTF of digital fluoroscopic systems and later also of amorphous silicon megavoltage detectors. We find references to this approach in the works of Bissonnette et al. (1994)[55], Munro and Bouius (1998)[45], Falco and Fallone (1998)[56], El-Mohri et al. (2001)[57], Cremers et al. (2004)[58], Sawant et al. (2005,2006,2007)[59,33], Samant and Gopal (2006,2008)[60,61,23] and Rottmann et al. (2016)[62]. The specific design of the phantoms varied greatly, with steel, tungsten or lead as the phantom material and the slit thickness ranging between 5 cm and 40 cm. However, all these publications were based on the underlying assumption that the thickest phantom is likely to yield the most accurate measurement results.

In one of his first publications, Rossmann stated that, depending on the energy of the radiation and the phantom in question, "varying amounts of secondary radiation" may be introduced by the phantom during the measurement.[44] Similar remarks were made by other groups which used the edge method. Earnhart et al. noted that the MTF was influenced by scatter from the edge phantom, but did not include a quantitative survey.[63] Star-Lack et al. described the effect of scatter generated by a 0.5 mm thick tantalum edge: The tails of the ESF were sloped, leading to a negative baseline for the LSF and presumably to deviations in the MTF. The authors attributed this to forward-scattered photons, induced by the phantom itself. The deviations occurred when the phantom was placed in direct contact with the detector and were reduced when the edge phantom was elevated several centimeters from the detector surface.[64]

Sawant et al. published one of the few studies focusing on the accuracy of the MTF measurement.[33] With a combination of measurements and Monte Carlo simulations, the design of a slit phantom was optimized in terms of slit width and thickness to minimize the effect of absorption unsharpness. The experimental study showed comparable MTF results for a 40 cm thick steel and a 19 cm thick tungsten phantom. The Monte Carlo study confirmed that, while thin phantoms induce a higher noise level, the various MTFs showed no significant differences. This lead the authors to the conclusion that a high measurement accuracy can be achieved regardless of the phantom thickness. This is contradictory to the findings of Min et al., who showed that a 40 cm thick steel edge and a 19 cm thick tungsten edge phantom produce different results for the detector MTF.[65,66,67] Gopal et al. attempted a comparison of previously reported MTF results and found great variations.[23] As there have been so few reports of MTF measurements, the authors compared clinical systems to various prototype stages. This implies that there were small changes in the detector geometry, which might have shown in the

MTF. However, the differences were so pronounced (e.g. MTF_{20} varying between 0.55 mm^{-1} and 0.8 mm^{-1}) that the authors were hesitant to attribute them to the detector models alone and speculated upon the possible influence of the imaging geometry and the beam quality.

Authors	Year	Phantom	Material	Thickness	Slit width	SID	Geometry	Processing
Hu et al. [68,69]	2018	Slit	Tungsten	12 cm	100 μm	150 cm	Contact	1,2,3
Rottmann et al. [62]	2016	Slit	Tungsten	18.7 cm	100 μm	151.5 cm / 153 cm	Contact	1,2,3,5
Star-Lack et al. [64]	2015	Edge	Tantalum	0.5 mm	-	320 cm	Air Gap	6
Son et al. [67]	2014	Edge	Tungsten	19 cm	-	132 cm	Contact	
Min et al. [66,65]	2014	Edge	Tungsten	19 cm	-	unknown	Contact	1,2,3
			Steel	40 cm				
Gopal and Samant [23]	2008	Slit	Steel	16 cm	40 μm	132 cm	Contact	7
		Edge	Steel	16 cm	-	132 cm	Contact	
		Bar pattern	Tungsten	0.2 cm	-	isocentric setup	Air Gap	
Sawant at al. [33,59]	2007/	Slit	Tungsten	19 cm	100 μm	138 cm	Contact	2,3,5,8
	2006		Steel	40 cm				
Samant and Gopal [61]	2006	Slit	Steel	16 cm	100 μm	unknown	Contact	8,12
Samant and Gopal [60]	2006	Slit	Lead	20 cm	40 μm	unknown	Contact	5,12
Sawant et al. [70]	2005	Slit	Steel	5 cm	100 μm	86 cm	Contact	1,2,3,5,8
Cremers et al. [58]	2004	Slit	Tungsten	10 cm	100 μm	100 cm	Contact	5,8,12
El-Mohri et al. [57]	2001	Slit	Steel	40 cm	100 μm	130 cm	Contact	2,3,6,9
Falco and Fallone [56]	1998	Slit	Steel	16 cm	25 μm	131 cm	Contact	5,8,10,11,12,13
Munro et al. [45]	1998	Slit	Steel	5 cm	80 μm	unknown	Contact	2,5,6,8,9,10
Earnhart et al. [63]	1997	Edge	Lead	7.6 cm	-	212 cm	Contact	2,3,12,14
Bissonnette et al. [55]	1994	Slit	Steel	5 cm	88 μm	unknown	Contact	5,11,12
Munro et al. [54]	1990	Slit	Steel	5 cm	30-200 μm	unknown	Contact	5,12,13

Munro et al.[53]	1987	Slit	Tungsten	10.5 cm	25 μm	60-90 cm	Contact	4,5,6,10,11,12,13
Droege et al.[31]	1979	Slit	Tungsten	1.6 cm	25 μm	3-4 m	Both	5,6,10,12,13,15
Droege[32]	1979	Slit	Tungsten	1.6 cm	25 μm	3-4 m	Both	5,10,12,13,15

Table 2.1: This is a complete list of all MTF measurements at MV energies reported in the literature up to July 2020. There is a great variance regarding the phantom design, the setup geometry and the processing techniques of the acquired images.
Legend of processing techniques:
1 - Dead pixel correction
2 - Darkfield correction
3 - Gain correction
4 - Linearization
5 - Averaging of several ESF/LSF estimates
6 - Baseline correction of ESF/LSF
7 - Smoothing of ESF/LSF
8 - Subtraction of image from closed slit
9 - Normalization of LSF to area under the curve
10 - Folding around center and averaging of LSF
11 - Extrapolation of LSF tails
12 - Correction of MTF for finite slit width
13 - Correction of MTF for width of scanning aperture
14 - Correction for finite element differentiation
15 - Smoothing of MTF

2.7 The aim of this work

The above survey revealed that MTF measurements at MV energies have been conducted with a wide variety of phantom designs. There are hints, but no quantitative analyses, that geometric unsharpness, absorption unsharpness and scatter are the three main influencing factors with regard to MTF accuracy. The few and partly contradictory reports raise the question whether the MTF is influenced by the phantom design and, if so, what size of systematic error to expect. If the factors contributing to the systematic error are known, it is possible to contrive phantom designs in which the error is minimal. To arrive at this point, one fundamental question must be answered first: How can we quantify the accuracy of an MTF measurement for a given phantom?

This thesis presents MTF measurements on a clinical MV portal imaging system, which aim to reveal the differences caused by the phantom design. The influences of geometric unsharpness, absorption unsharpness and scatter on the accuracy of the measurement result are investigated using Monte Carlo simulations. Based on the results, several phantom designs are presented which provide high accuracy at 6 MV beam quality. The technique developed to quantify the systematic error in an MTF measurement is based upon the analysis of the detector input signal and can be put to use with other detector models, phantoms or beam qualities.

3

Methods and Materials

The first part of this work is an experimental investigation in which the MTF of a single representative imaging device is measured with various phantom designs. Further insights are gained by Monte Carlo simulations of the detector input signal. An analysis program was written for both experimental and simulated edge images.

3.1 MTF measurement with an EPID

The measurements presented in this thesis were performed with the photon beam of a Varian TrueBeam linear accelerator (v.2.5). The linear accelerator was calibrated such that 100 monitor units (MU) deliver 1 Gy of dose in water at 100 cm distance from the source at the depth of maximum dose for a 10 cm $\times$ 10 cm field. The EPID used for image acquisition was the PortalVision aS1200 MV imaging system, an active matrix flat panel imager (AMFPI).

Patient imaging for setup is generally performed using the lowest available energy to maximize the image contrast. In many clinics today, that is the 6 MV beam (Fig. 3.1), which is also a common choice for treatment. The experiments and simulations presented in this work are therefore based on a 6 MV beam.

As a starting point, recommendations for MTF measurements at kV energies were employed. The IEC

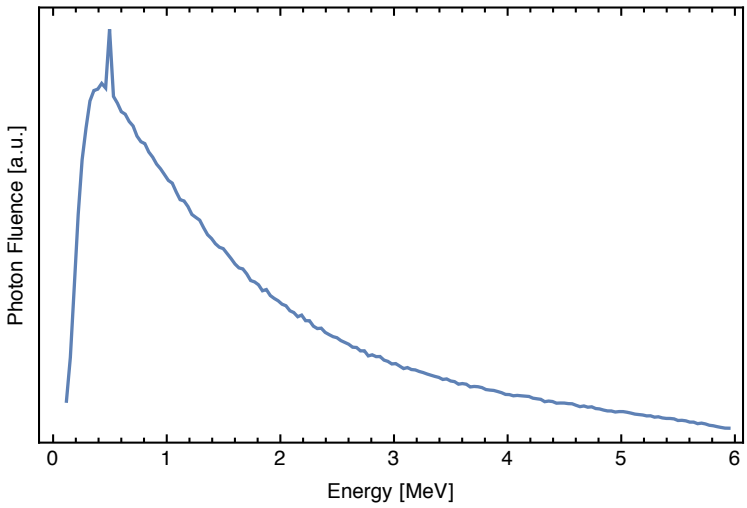

Figure 3.1: Energy spectrum of the 6 MV photon beam of a Varian TrueBeam linear accelerator (obtained from Monte Carlo simulation). The peak at 512 keV results from bremsstrahlung photons originating from the collimating jaws. Relative photon fluence.

report 62220-1 states that the phantom should be placed in direct contact with the detector and the source-to-imager distance (SID) enlarged as much as possible.[16] Both instructions aim to minimize the geometric unsharpness.

The images of the experimental setup, with the gantry in up-down position (0°) and the phantom sitting on the extended MV detector, give a general idea of the geometry and dimensions (Figure 3.2a). The detector is attached to the gantry and can be vertically translated to allow variable SIDs. During clinical use, a plastic cover with integrated collision protection prevents mechanical damage to the detector. The cover was removed during measurements to reveal the front plate of the detector, which is situated 12 mm in front of the image plane.

The SID was set to 180 cm, which is the maximum for TrueBeam machines. Additional measurements and calculations were included for Elekta machines, where the SID is fixed to 160 cm (see page 80). The field size, collimated by jaws, was adjusted to cover the entire active area of the detector (43 cm x 43 cm) without irradiating the electronics (e.g. 22.5 cm x 22.5 cm at SID 180 cm). Using the light field, the edge phantom was aligned with the central axis, then rotated to create a slight angle with respect to the detector array ($\approx 2°$, realized by collimator rotation, Fig. 3.2b). This is based on an idea by Fujita et al., which enables us to record the ESF at a higher sampling rate.[71] Details on this technique will be given while discussing the image analysis (see page 45).

(a) Varian TrueBeam accelerator with extended PortalVision aS1200 megavoltage detector (cover removed).

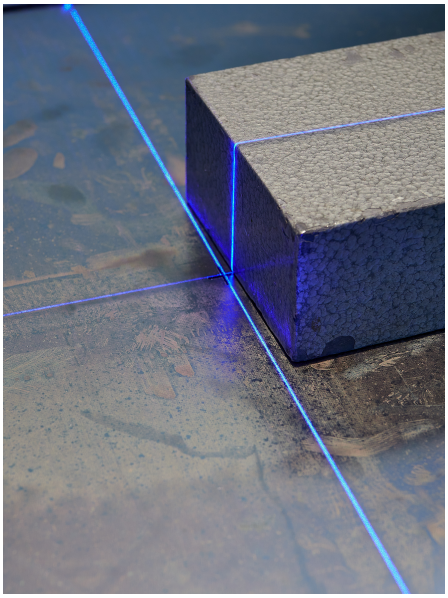

(b) The edge phantom (here: lead, 5.0 cm thick) is positioned in the center at a slight angle ($\approx 2°$) to the pixel array.

Figure 3.2: Setup for MTF measurements on a Varian TrueBeam machine. Measurements were conducted at the Center for Radiotherapy at Klinikum Dortmund.

3.1.1 The PortalVision aSi200 MV detector

Ionizing radiation can be detected with direct or indirect detectors. Although the radiation response of direct detectors has been shown to be conveniently close to that of ionization chambers, the combination of high-energy radiation and a thin sensor array makes for very low radiation sensitivity.[7] The PortalVision aS1200 is built as an indirect detection system. In an indirect detection system, high-energy photons are converted into optical photons by use of a scintillator (Fig. 3.3).

The aS1200 detector consists of a copper plate (1 mm thickness) and a 290 μm thick layer of terbium doped gadolinium oxysulfide as scintillation material (134 mg/cm^2 Gd_2O_2S:Tb).[72] The copper plate shields the detector from scattered radiation and acts as buildup material. An aluminum plate below the photodiode array shields the detector from backscatter arising from the steel and copper components of the supporting MV detector arm. The array of photodiodes, which are implanted on an amorphous silicon panel, detects the low energy photons with high efficiency. On the other hand, the spreading of high-energy and optical photons in the phosphor screen leads to a loss of spatial resolution, also known as *glare*.[73]

The photodiode array contains 1280×1280 pixels with 0.336 mm pixel pitch.[72] Images were acquired with full resolution (Mode: High Resolution). The detector can be used for high-intensity applications such as

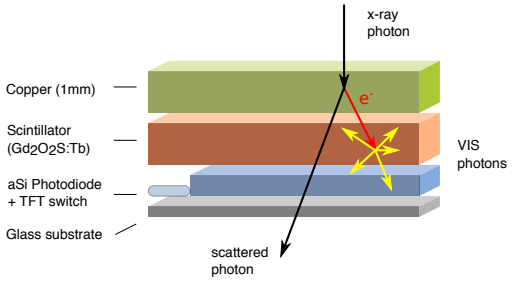

Figure 3.3: Sectional view of the PortalVision aS1200 detector.

portal dosimetry of flattening filter free (FFF) beams with dose rates of 2400 MU/min. In the context of portal dosimetry, the detector has been shown to display a linear response to exposure over the entire dynamic range. The maximum nonlinearity is 0.5% for low exposure (5 MU) and decreases to less than 0.1% for exposures above 30 MU.[62]

Regarding the exposure to be used for image acquisition, we cannot refer to the IEC report, and there are no recommendations in previous studies. Images for verification of patient positioning are typically acquired with an exposure of about 3 MU. For phantoms, the imaging dose is of no importance and images can be acquired with much higher exposure, which will reduce the noise in the image. Unless explicitly stated otherwise, all reported measurements were acquired with 40 MU (in several frames to avoid saturation) at 600 MU/min dose rate. As will be discussed, this exposure allowed to determine the MTF with ± 0.01 standard error of the mean for spatial frequencies up to 1 mm^{-1} (see Section 4.1.3).

Prior to the measurements, the MV detector was calibrated to update the dark field and flood field correction maps. Apart from gain, offset and dead pixel correction, no post-processing was applied. See page 45 for details on the analysis of experimentally obtained edge images.

3.1.2 The edge phantoms

Four edge phantoms were compared during measurement, consisting of rectangular lead blocks, with 1.3 cm, 3.3 cm, 5.0 cm, and 10.0 cm thickness. Based on previously published reports (compare Table 2.1), each of the four phantoms should be suitable for MTF measurement with a 6 MV photon beam. Transmission of radiation through the phantoms was 53 %, 24 %, 12 %, and 3 %, respectively (see page 56). Width and length of the phantoms differed slightly, with values ranging between 6 cm and 10 cm. This was of no consequence, as only the central image region containing only the edge transition was used for analysis.

Experiments and simulations were performed using either of two possible geometries: In *contact geometry*, the phantom is placed in direct contact with the detector (Fig. 3.4a), as described in the IEC 62220-1 report. In *air gap geometry*, the phantom is elevated several centimeters above the detector (Fig. 3.4b), following an approach by Star-Lack et al.[64]. The air gaps were created by positioning the phantoms on styrofoam blocks

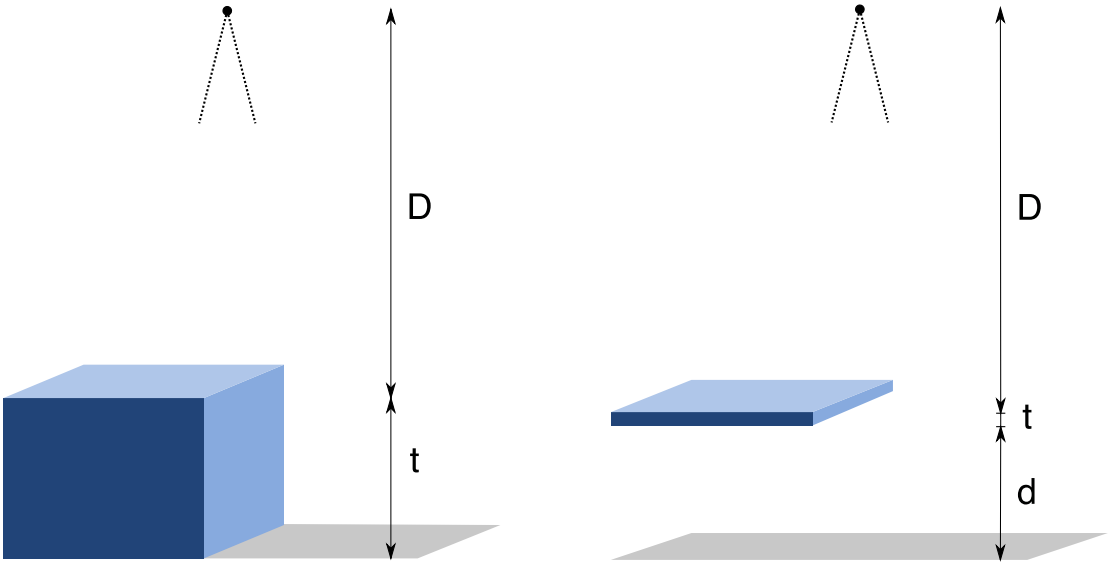

(a) Contact geometry.

(b) Air gap geometry.

Figure 3.4: Measurements and simulations were conducted with the phantom either in direct contact with the detector, or elevated to create an air gap. Phantom dimensions exaggerated for illustration.

with cutouts. The source-to-imager distance (SID) equals the sum of the source-to-phantom distance D, the phantom thickness t and, if applicable, the distance d between phantom and image plane.

3.2 Monte Carlo simulation using EGSnrc

Monte Carlo simulations allow the investigation of physical processes during irradiation with diagnostic and therapeutic photon beams by faithful simulation of particle transport processes. Interactions of photons with surrounding matter can be sorted into four main categories:

1. Photo-electric absorption
2. Incoherent scattering / Compton scattering with atomic electrons
3. Pair production in the electromagnetic field of a nucleus and surrounding atomic electrons (possibly also triplet creation)
4. Coherent scattering / Rayleigh scattering with atoms or molecules

Interactions of electrons with surrounding matter fall into three main categories:

1. Inelastic collision with atomic electrons
2. Radiative energy loss from bremsstrahlung or positron annihilation
3. Elastic collision with atomic nuclei

The statistical behavior of this many-particle system can be described by the Boltzmann transport equation. In the lists above, the majority of interactions involves an energy transfer from photons to electrons or vice versa. These couplings between electron and photon radiation fields prevent an analytical solution of the electromagnetic shower unless severe approximations are made. The Monte Carlo (MC) technique is the only known method which can be applied to solve these integro-differential equations at any energy range of interest.[74] Monte Carlo methods provide statistical solutions for macroscopic quantities of a many-particle system. They approximate the expected value of a quantity with an empirical mean of independent samples. The accuracy increases with the number of drawn samples, as stated by the law of large numbers.[75]

There are three main ingredients for a Monte Carlo simulation: physics, statistics and geometry. The physics of the many-particle system is mainly contained within cross section tables for the particle interactions. The algorithm derives the probability of future events from the cross sections and finally determines which event takes place by use of a random number generator (at least 10^{100} uncorrelated pseudo-random numbers). The way in which the geometry is constructed varies greatly between the different Monte Carlo programs. Some offer a range of prebuilt geometry modules which can be combined, others allow the import of a CAD geometry.

The simulations in this thesis were carried out using the EGSnrc Code system[74] (EGSnrc v2017, commit `29add4c`). "EGS" stands for Electron Gamma Shower, as the software models particle showers which are induced by the passage of photons, electrons and positrons in homogeneous materials. EGSnrc is particularly

popular in the Medical Physics community, as it is well suited for modeling of linear accelerators and x-ray systems, dose calculations or calculations of correction factors for ionization chambers. A simulation with EGSnrc starts by creating particles ("hatching" in EGSnrc terms) dependent on the particle distribution provided by the radiation source. Based on the total interaction cross section, the particles travel a certain distance until an interaction takes place. At this point, the particles change their energy and/or direction, and new particles are created if applicable. This is repeated until all particles are either absorbed or have left the geometry. The path of one particle from creation to end point is called a particle "history" (also "shower" or "case"). In order to extract a physical quantity from the simulation, the average is calculated over a set of particle histories.[76] Following an approach by Sempau et al.[77], the statistical uncertainty $s_{\bar{X}}$ of a quantity X is calculated from the outcome of each history i as

$$s_{\bar{X}} = \sqrt{\frac{1}{N-1}\left(\frac{\sum_{i=1}^{N} X_i^2}{N} - \left(\frac{\sum_{i=1}^{N} X_i}{N}\right)^2\right)}. \tag{3.1}$$

It depends on the number N of particle histories and usually decreases as $1/\sqrt{N}$, as stated by the central limit theorem.[74]

Monte Carlo simulation of electron transport constitutes a major challenge. For a single electron history, thousands of inelastic collisions must be mapped, which severely increases the computation time. As a single collision of an electron with an atom will only cause a small alteration of the electron's energy and direction, Berger presented an idea to group large numbers of transport and collision processes into a single simulation step.[78] This is called the "condensed history" (CH) technique, which is implemented in EGSnrc. Electrons will undergo several multiple scattering steps (soft collisions) in which a continuous energy loss according to the Bethe-Bloch equation is assumed, until the next catastrophic event (hard collision or radiative collision) with a high energy transfer takes place (Figure 3.5a). The condensed history technique requires a thorough implementation of multiple scattering theory in order to determine the angular distribution of the condensed history steps. While this technique is extremely efficient and absolutely necessary to obtain meaningful results within an acceptable time frame, it can cause severe problems when describing the electron transport across the boundary of two media. In this case, the step size of the condensed history technique needs to be reduced, so that electrons are transported across the boundary in single scatter mode (Figure 3.5b).

Several Monte Carlo programs for radiation transport are available today, the most commonly known are Geant4, MCNP, Penelope, EGSnrc and Fluka. All of these programs use some form of condensed history technique. However, there are great differences in the treatment of electron transport across boundaries. An indicator for the quality of the electron transport is the Fano test.[79] The Fano theorem states that under charged

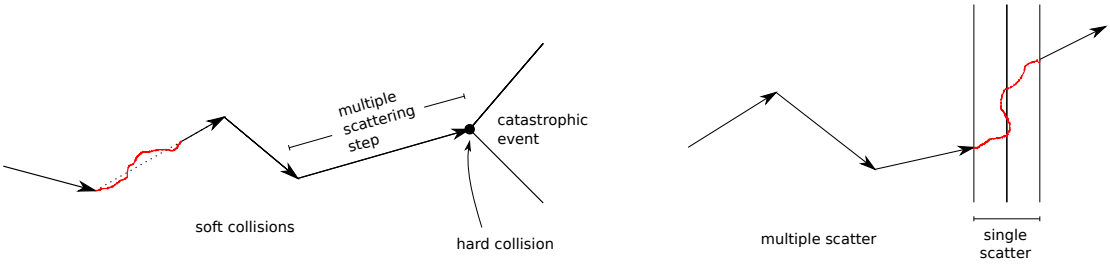

(a) Soft collisions are modeled as a single CH step with continuous energy loss according to the Bethe-Bloch equation. Hard collisions and radiative collisions are simulated as single scatter events.

(b) The boundary crossing algorithm in EGSnrc decreases the step size near a boundary so that particles are transported across the boundary in single scattering mode.

Figure 3.5: Illustration of the condensed history (CH) technique. Several electron interactions with low energy transfer (soft collisions) are grouped into a single condensed history step. The angular distribution of the condensed history steps is derived from multiple scattering theory.

particle equilibrium, the fluence of the charged particles is independent of the mass density of the media, if the cross sections of the media are uniform.[80] With regard to Monte Carlo simulations, this implies that the absorbed dose should equal the photon fluence times the mass energy absorption coefficient for each medium. Thus, the Fano test will show whether the absorbed dose is scored accurately during condensed history steps. At the moment, only Penelope and EGSnrc provide the required algorithms that allow the calculation of dosimetric quantities with high accuracy. EGSnrc has been shown to be accurate in condensed history steps to within 0.1% for maximum fractional energy losses of 0.05 to 0.25 per step.[81,82]

The EGSnrc distribution contains several user codes for various applications. All simulations in this thesis are based on the BEAMnrc user code. (The only exception is the beam data verification with a water phantom simulation (Fig. 3.7), which was performed with the DOSXYZnrc user code.) The BEAMnrc user code was specifically written for simulations of radiotherapy sources. For detailed information, the reader is referred to the original publication and the BEAMnrc Users Manual.[83,84]

A simulation with the BEAMnrc user code can be broken down into four parts (Fig. 3.6): First, the accelerator is constructed as a sequence of component modules (CM) that form different geometric parts of the accelerator. Second, an input file is provided, which contains specifications such as the materials and dimensions of the CMs, as well as general settings like the number of particle histories to be used in the simulation. The accelerator simulation is run by launching the executable code in combination with the input file and a pegs file that contains the cross section data. The simulation result is a phase space file, which contains data relating to the position, direction, charge and energy of each particle that crosses the specified scoring plane. The simplest way of analyzing a phase space file is via the BEAMdp GUI, which is part of the EGSnrc installation and allows access to spectra, fluence distributions, mean energies, angular distributions, etc. The following sec-

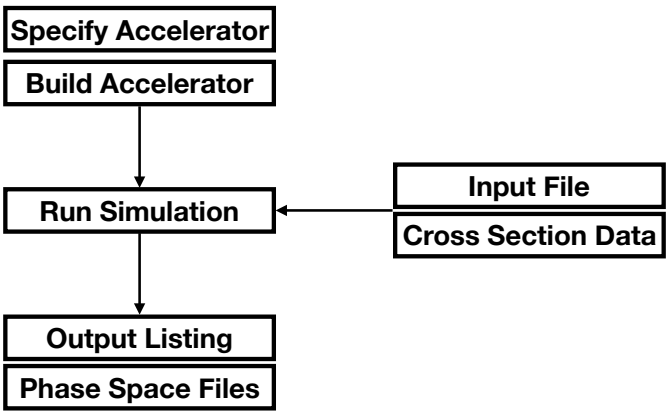

Figure 3.6: The four main steps of a BEAMnrc simulation: Constructing a generic accelerator, reading in the input file with geometry specifications and radiation transport parameters along with the cross section data, running the simulation and analyzing the output. Adapted from the original BEAMnrc publication.[83]

tions describe the implementation of a suitable radiation source, the geometry of the performed edge phantom simulations, and the procedure used to transfer the resulting phase space files into digital edge images.

3.2.1 Modeling the Varian TrueBeam

To mimic the experimental situation, the output of a Varian TrueBeam linear accelerator was used as the radiation source for all Monte Carlo simulations. Note that the simulations are expected to return similar results for other medical linear accelerators at the same beam quality.

Varian Medical Systems give confidential access to a Monte Carlo package that allows the simulation of a treatment beam for research purposes.[85] The package contains phase space files for the field-independent part of the treatment head, i.e. scored just above the collimating Y and X jaws. The mean energy and spectral width of the provided phase-space files are tuned such that open field dose distributions match the generic Varian TrueBeam. The photon beam is collimated by the Y and X jaws. While the X jaws follow a linear trajectory, the Y jaws move along a circular arc to keep the edge focused. However, it was shown that the Y jaws can be assumed to follow a linear trajectory, as long as both jaw faces remain focused on a 0.3 cm $\times$ 0.3 cm square at the location of the target.[86] The jaws were therefore modeled as tungsten blocks with divergent edges, corresponding to a field size of 10×10 cm^2 in the isocenter plane (Fig. 3.7). With respect to the confidential agreement with Varian Medical Systems, further details about the geometry of the jaws are not published in this thesis.

Previous works have occasionally modeled the linear accelerator as a point source[33] or a parallel beam[58] with an underlying photon spectrum. It will later be demonstrated that an accurate Monte Carlo simulation of the detector input signal requires use of the actual particle distribution, including extra-focal radiation.

To validate the implementation of the TrueBeam phase space for further use in subsequent calculations, the output was verified by scoring depth dose curves and profiles in a water phantom and comparing them to

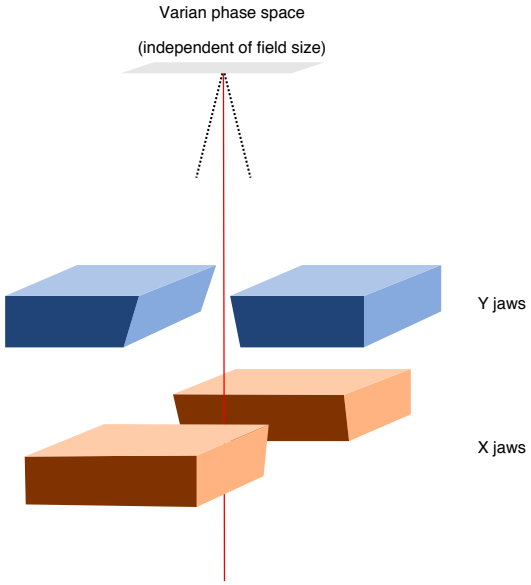

Figure 3.7: Schematic representation of the TrueBeam model for field-specific simulations, showing the field-independent Varian phase space and the Y and X jaws. Geometry details were provided by Varian Medical Systems as confidential information.

the TrueBeam Golden Beam Data (dosimetric reference dataset provided by Varian Medical Systems [87]), as well as dose measurements for the Varian TrueBeam machine on which the MTF measurements were conducted. The user code DOSXYZnrc [88] was set up to simulate a water phantom (40 cm × 40 cm × 40 cm) that was irradiated in source-to-surface distance (SSD) 100 cm with a 6 MV photon beam and 10 cm × 10 cm field size. Analysis of the 3D dose distribution was performed with the STATDOSE user code. [89] The comparison of the percentage depth dose curve (PDD) and the cross-plane and in-plane beam profiles shows that simulated and vendor-provided dose distributions coincide (Fig. 3.8) and further agree with the measured dose distribution. The agreement in both the PDD and the profiles was within 2%, which would also be clinically acceptable.

The number of particle histories used in a simulation can be related to the number of monitor units (MU) by simulating the dose distribution in a water phantom. [90] In analogy to the absolute dosimetry of a linear accelerator, the maximum dose value $D_{max,ref}$ on the central beam axis is compared with the calibration protocol of the accelerator (here: 100 MU equal 1 Gy at d_{max} for reference field of 10 cm × 10 cm). Although this approach neglects the influence of backscatter from the jaws on the monitor chamber, it has been shown that the result is accurate within 2%. [91] The above described simulation of a water phantom in DOSXYZnrc requires $6 \cdot 10^7$ particles to reach a dose of 1 Gy at the dose maximum, which is equivalent to 100 MU. The effective number of 10^{10} particle histories used for edge phantom simulations therefore equals approximately 167 MU.

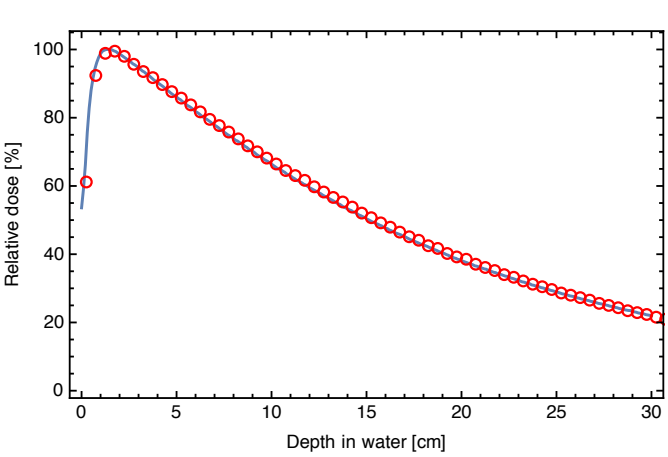

(a) Percentage depth dose curve.

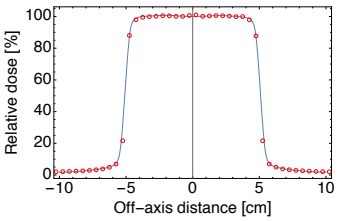

(b) Cross-plane beam profile.

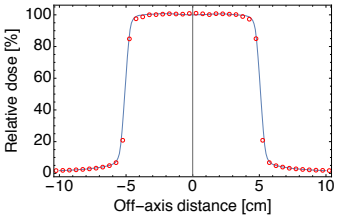

(c) In-plane beam profile.

Figure 3.8: A comparison of MC simulated (red) and vendor-distributed (blue) PDD and profiles, scored in depth of maximum dose d_{max}, for a 6 MV photon beam with 10 cm $\times$ 10 cm field size. Data was normalized to d_{max} for the PDD, and to the central axis value for the profiles. Profiles and PDD agree within 2%.

3.2.2 Monte Carlo simulation of edge phantoms

For efficient simulations of edge phantoms in various geometries, the TrueBeam output was scored directly below the jaws. The resulting phase space was then implemented as a radiation source for the following edge phantom simulations. Particles emanate from the radiation source and propagate through air or the respective phantom material until they reach the scoring plane. The simulation geometry was adapted to mimic the experimental situation. As described above, phantoms were simulated either in contact or air gap geometry (Fig. 3.4). The edge phantom was modeled as a rectangular slab of the respective material and thickness and covered one half axis of the simulation geometry (Fig. 3.9). The distance between source and scoring plane equals the source-to-imager distance (SID) in an experimental setup. The phantom design is determined by the material and the phantom thickness t. The Monte Carlo simulations did not model the detector itself as they were meant to be applicable to any MV imaging device operating at a comparable beam quality.

In reality, due to the spatial extent of the aS1200 detector, the phantom sits on the front plate at a distance of 12 mm from the image plane.[92] Here, the scoring plane was defined at the image plane, assuming an idealized detector without spatial extent. Changes in the simulation results due to this simplification were found to be negligible.

An exemplary input file for the simulation of an edge phantom can be found in Appendix A.1.1. Apart from the geometry, the input file specifies the radiation transport parameters to be used during the simulation. These include, among others, the cut-off energies below which electron and photon transport are terminated.

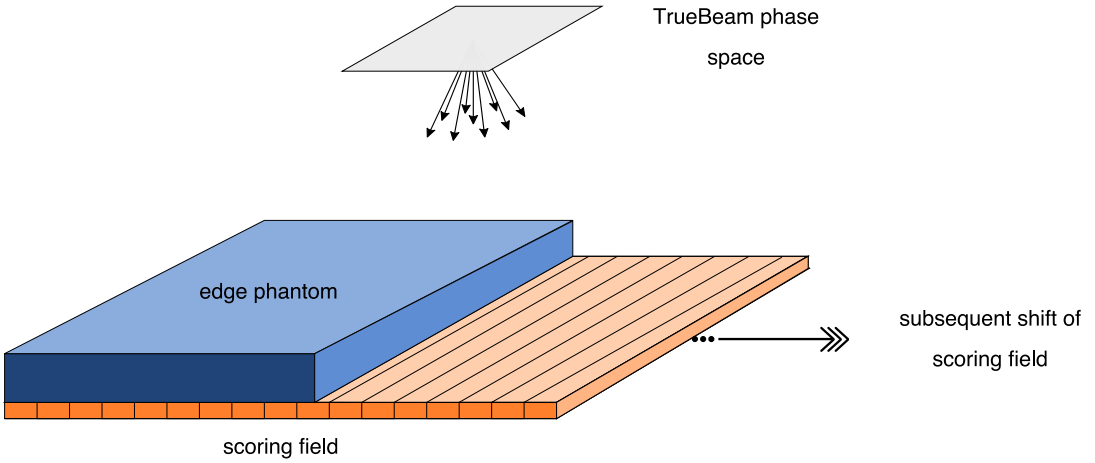

Figure 3.9: Exemplary geometry of the scoring field used for evaluation of phase space files. The photon fluence is scored in rectangular bins of 0.2 mm width and 20 cm length. Scoring multiple times while translating the scoring field relative to the phantom produces a finer sampled spread function.

For detailed information on the settings, please see Appendix A.1.2.

3.2.3 Scoring the photon fluence

The detector input signal received by the MV detector was assessed by detecting the photon fluence distribution at the image plane (=scoring plane). The outer boundary of the simulation geometry at the scoring plane was a square of 60 cm side length. Only the central region of interest (ROI) with a size of 8 cm $\times$ 20 cm was used for the subsequent analysis. This ensured a homogeneous scatter distribution by avoiding changes in the fluence close to the phantom or field edges. The photon fluence perpendicular to the edge was extracted from the phase space (the electron fluence was found to be negligible). This was achieved with the BEAMdp user code, which partitioned the particles in 400 strips, 0.2 mm $\times$ 20 cm in size (Fig. 3.9), resulting in a detector input signal of 80 mm length. The fluence within the open field is homogeneously distributed, so that it can be averaged over the width of 20 cm (parallel to the edge) to improve the statistics.

To obtain a more finely sampled detector input signal without compromising the statistical uncertainty in the individual bins, an oversampling technique was developed in analogy to the angled phantom used for MTF measurement. The photon fluence was scored 26 times, while the scoring field was moved perpendicular to the edge transition by increments of 1/26 of the bin width (compare Fig. 3.9). The 26 data sets were interlaced to produce a detector input signal with a sample spacing of 0.2 mm / 26 = 0.0077 mm. Sampling the spread function at a higher rate prevents aliasing effects, as the Nyquist frequency increases to 65 mm^{-1}. Regardless of the oversampling factor, the photon fluence is still integrated over 0.2 mm bin width. This averaging effect

introduces an additional unsharpness, with a sampling MTF as described in Eq. (2.38). The first zero in the sampling MTF appears at 5 mm^{-1} spatial frequency. As the frequency range of interest for clinically used MV detectors is limited to about 1 mm^{-1}, the calculated MTF can be corrected for the influence of the sampling aperture, i.e. divided by the sampling MTF (see Section 3.3.2).

3.2.4 Variance reduction techniques

The Monte Carlo simulations presented in this thesis require a high number of particle histories to obtain a low uncertainty in the resulting MTF. Even though all available particles in the TrueBeam phase space were used (a total of $2.5 \cdot 10^9$ particles), additional steps were necessary to further reduce the variance. BEAMnrc offers several variance reduction techniques which artificially increase the number of particles in a simulation. Appropriately combined, they can achieve efficiency gains of up to five orders of magnitude.[84] However, it is important to note that all these techniques can potentially impair the integrity of the underlying physics and should be used with caution.

Range rejection is a powerful technique to save calculation time during electron transport. With range rejection turned on, the algorithm calculates the range of a charged particle and determines whether the particle can leave the current region. If not, the particle history is terminated and the entire energy is deposited in the current region.[84] By forcing an electron that cannot leave the region to deposit its entire energy in one spot, the simulation neglects bremsstrahlung photons which might have been produced during subsequent interactions of the electron. Therefore, the use of range rejection requires careful analysis of the appropriate cutoff energy, i.e. the maximum energy of a charged particle at which range rejection is considered.

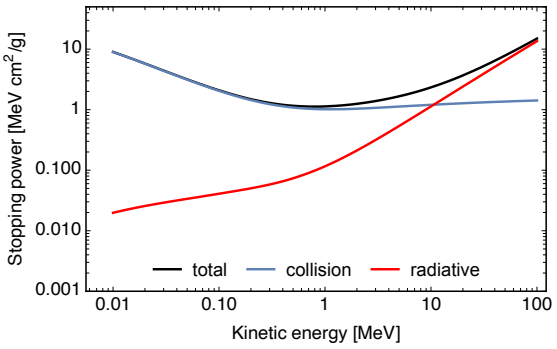

Figure 3.10: Collision, radiative and total stopping power of electrons in a lead absorber. Below 1 MeV, the stopping power is primarily based on collision interactions. Above 1 MeV, electron interactions produce substantial amounts of bremsstrahlung. Data according to NIST database.[93]

The stopping power of a lead phantom (Fig. 3.10) results almost entirely from collision interactions below 1 MeV kinetic energy. Electrons with higher energies can induce the production of bremsstrahlung photons. Setting the electron cut-off energy to 1 MeV in the edge phantom simulations will therefore eliminate electrons whose range would not have permitted them to reach the scoring plane and that only contributed negligible

quantities of bremsstrahlung. Comparisons of the photon spectrum at the exit surface of edge phantoms also found no significant difference between simulations conducted with and without range rejection at 1 MeV. Similar results can be obtained for tungsten phantoms. All phantom simulations in this thesis were therefore performed with range rejection for charged particles with energies below 1 MeV.

Running the simulation with more particle histories than present in the phase space source can be achieved with *particle recycling*. This way, each particle will be used several times before moving on to the next particle. Alternatively, the simulation can be repeated multiple times with different *initial random seeds*. Both options work well and are frequently used when the input phase space data is sparse. However, duplicating the available phase space particles only reduces the uncertainty introduced by the simulation. The overall uncertainty also depends on the latent variance of the phase space file, which is not influenced by particle recycling.[76] The main prerequisite for particle recycling is high particle interaction during the simulation. The simulation of the fluence distribution behind an edge phantom involves a high number of interactions in the phantom itself and basically no interactions at all in the open field which adjoins the phantom. The fluence distribution of the open field mercilessly displays the inherent variance of the phase space source. In this case, particle recycling or the use of different random seeds is ineffective and misleading, as it artificially reduces the standard deviation in the scoring bins without increasing the overall precision of the fluence distribution. Therefore, the edge phantom simulations were limited to the $2.5 \cdot 10^9$ particles present in the TrueBeam phase space.

Instead, an alternative solution was found to reduce the statistical variability of phantom simulations. Taking advantage of the simulation geometry and the isotropic fluence distribution of the photon beam, four simulations were run for each edge phantom design, with the TrueBeam phase space being subsequently rotated by 90° around the central axis (Fig. 3.11). The detector input signal was extracted for each simulation and the four results were averaged. Implemented via a short script, this is a simple yet effective strategy to perform the edge phantom simulations with an effective number of 10^{10} particle histories.

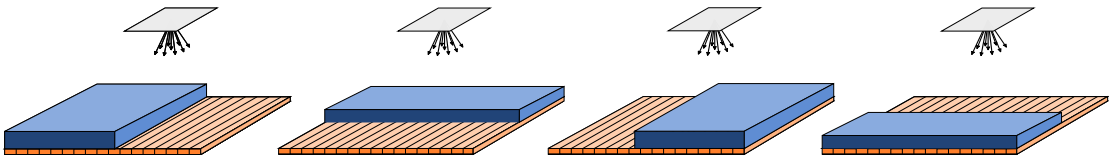

Figure 3.11: Rotating the simulation geometry relative to the scoring field results in four different particle distributions as simulation input, which when averaged reduce the latent variance in the TrueBeam phase space data.

3.3 Computational analysis of edge images

The analysis of both experimental and simulated edge images was performed with Mathematica, version 12.0.0.0, Wolfram Research.[94] The source code is included in Appendix A.2.

3.3.1 Analysis of experimental images

Medical imaging information is handled using the DICOM standard (Digital Imaging and Communications in Medicine). The PortalVision aS1200 produces 16 bit DICOM files, consisting of the image data and meta information. The image data was extracted and converted into 16 bit TIFF files, then cropped to the central region around the edge transition (300 px × 100 px). As discussed, linearization of image data can be omitted.

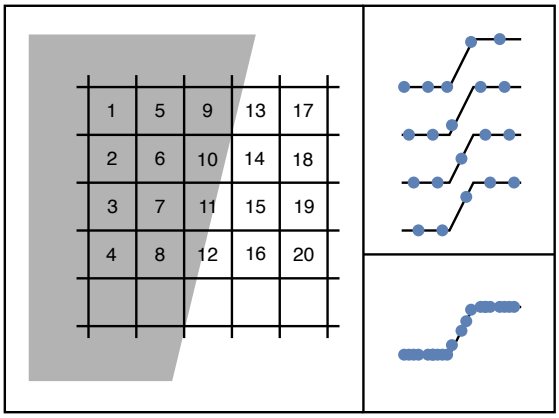

Figure 3.12: The subsampled ESF is produced by interlacing consecutive pixel rows. This example shows a shift of one pixel every four rows. The pixel numbering indicates the interlacing order. Adapted from Fujita et al.[71]

Oversampling technique The problem of aliasing effects in undersampled imaging systems was introduced in Section 2.5.1. Fujita et al. introduced an oversampling technique for MTF measurements which effectively reduces the sampling distance and thereby increases the Nyquist frequency.[71] Each pixel row in the image contains information about the edge transition. As the pixel aperture is larger than the spread of the impulse response, the edge transition typically takes place within the width of one pixel. By aligning the edge phantom at a slight angle with respect to the pixel array, the position of the edge transition shifts horizontally from one row to the next (Fig. 3.12). Consecutive row are interlaced to produce a subsampled ESF as indicated by the pixel numbering. The original ESF sampling distance Δ is reduced to $s = \Delta/N$, with N the oversampling factor, i.e. the number of rows over which the edge transition shifts horizontally by one pixel. With this oversampling technique, the Nyquist frequency is increased by a factor N, as $\xi_{Ny} = \frac{1}{2s} = N\frac{1}{2\Delta}$. Misinterpretation of spatial frequencies can therefore only occur for very high frequencies outside the range of interest, for which the MTF values are near zero. In accordance with IEC report 62220-1, the edge angle was kept between

1.5°-3°, which corresponds to an oversampling factor between 19 and 38.[16] Note that the averaging effect of the sampling aperture is still present in the subsampled ESF.

Determination of the edge angle The first step in the computational analysis is the determination of the edge angle. The edge position in each row is determined using linear interpolation. A linear regression of edge position versus row number returns the slope b, which can be used to determine the edge angle α and the average number of lines N_{av} that produce a horizontal shift of one pixel:[29]

$$N_{av} = \frac{1}{b} = \frac{1}{\tan(\alpha)}. \tag{3.2}$$

The oversampling factor N_{av} is rounded to the nearest integer N_{int}. The rounding error has been shown to be well below 1 % for our frequency range of interest and an edge angle around 2.0°.[29] Once the edge angle is known, the oversampled ESF is constructed as described above by interlacing N_{int} consecutive lines of the image (Fig. 3.13a).

Finite element differentiation The LSF (Fig. 3.13b) is obtained by *finite element differentiation*, using the symmetric central difference between neighboring pixels

$$f'(x) \approx \frac{f(x+s) - f(x-s)}{s}. \tag{3.3}$$

In Mathematica, this was realized by convolution of the ESF with a [0.5,0,-0.5] kernel. Finite element differentiation introduces a small error[28], for which a correction is applied in the frequency domain.

Fast Fourier Transform To calculate the MTF, a *Fast Fourier Transform* (FFT) is applied to the oversampled LSF. Prior to FFT, the length of the LSF was symmetrically truncated around the edge transition to a length of 2^{12} data points. Depending on the edge angle, this number of data points corresponds to a length of 5-7 cm in the image. As the LSF length can impact MTF accuracy[95], this step is further investigated in Section 4.1.1. The absolute value of the FFT result is normalized to the zero frequency value to obtain the presampled MTF (Fig. 3.13c). The frequency resolution of the MTF depends on the length of the LSF and therefore varies with the edge angle between measurements.

Figure 3.13: Illustration of the steps in the image analysis, based on a simulated edge image.

(a) ESF.

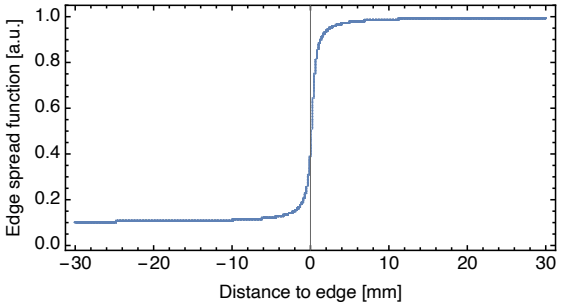

(b) LSF.

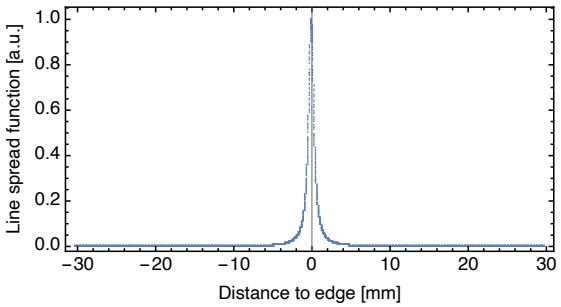

(c) MTF.

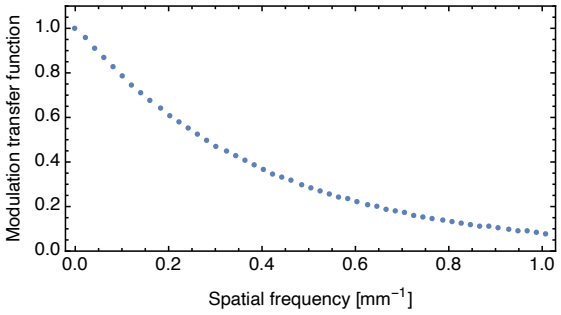

Corrections Finite element differentiation introduces a systematic error which depends on the subsampling distance s:[28]

$$\frac{\mathrm{MTF}_{estimated}}{\mathrm{MTF}_{true}} = \mathrm{sinc}\left(\frac{\pi\xi}{\xi_{Ny}}\right) \tag{3.4}$$

$$= \mathrm{sinc}\left(2\pi s\xi\right). \tag{3.5}$$

The previously calculated MTF is divided by this term to correct for the numerical differentiation.

The sampling points in the ESF were assumed to lie perpendicular to the edge. Due the edge angle α, the sampling distance between data points is actually smaller by a factor of $\cos(\alpha)$. The spatial frequency axis is therefore rescaled by the factor $1/\cos(\alpha)$.[16]

3.3.2 Analysis of Monte Carlo simulated images

Apart from the fact that the edge angle is already known, the analysis of the Monte Carlo simulated images is carried out as described above for experimental images. The photon fluence is scored 26 times, with the scoring field translated relative to the phantom (see Section 3.2.3). This results in an edge angle of 2.2°. The MTF is inevitably affected by averaging the signal over the width of the scoring bins (0.2 mm). To eliminate this influence from the results, the calculated MTF is divided by

$$\mathrm{MTF}_{\mathit{binning}} = |\mathrm{sinc}(\pi \cdot 0.2\,\mathrm{mm} \cdot \xi)|. \tag{3.6}$$

Each particle emitted from the source is tracked throughout the entire simulation. The phase space at the scoring plane contains a 32 bit LATCH variable for every particle, which provides information on the particle charge and, most importantly, on the geometric regions in which the particle has been or has interacted.[84] This allows to filter the final phase space based on the particle history. Using the LATCH variable, it is possible to distinguish between primary radiation (no interaction) and secondary radiation (created within phantom). The sum of primary and secondary radiation equaled the total radiation, which confirms that the particle selection worked correctly and all particles were taken into account.

Since the simulation did not model the detector but ended at the image plane, the MTF derived from the total photon fluence directly indicates the systematic error of a measurement with the given phantom, arising from the differences between the detector input signal and an ideal step function. Later on, this MTF is titled *phantom MTF*.

3.3.3 Verification of computational analysis

The results presented in following sections rely heavily on the correct implementation of the previously presented calculation steps. The Mathematica program written for analysis of experimental and Monte Carlo simulated edge images was therefore tested with a series of synthetic edge images, for which the true MTF was known. The synthetic edge images were based on the following analytical edge spread function:

$$\mathrm{ESF}_{\mathrm{sim}}(x) = \begin{cases} 1 - \frac{1}{2} \cdot \mathrm{e}^{-rx} & x \geq 0 \\ \frac{1}{2} \cdot \mathrm{e}^{+rx} & x < 0. \end{cases} \tag{3.7}$$

The parameter r defines the steepness of the ESF and thereby the detector response. When x is expressed in millimeters, a value of r=0.65 approximately matches the edge transition found in clinically used MV detectors.

Figure 3.14: This digital edge image with exaggerated edge transition was created from an analytical edge spread function.

The MTF corresponding to ESF_{sim} is Lorentzian shaped:

$$MTF_{sim}(\xi) = \frac{r^2}{r^2 + (2\pi\xi)^2}. \tag{3.8}$$

To construct a synthetic edge image, the values of ESF_{sim} were sampled and written to an array, including a shift of $\tan(\alpha)$ from row to row to produce the image of an edge with edge angle α (Fig. 3.14). The corresponding source code can be found in Appendix A.2. To obtain a more realistic edge image, the analytical edge spread function can be convolved with a rectangular function to mimic the effect of a sampling aperture, followed by the addition of Poisson or Gaussian noise to the primary signal.

The discrete MTF values calculated for three exemplary synthetic images showed excellent agreement with the theoretical MTFs (Fig. 3.15). MTF results presented in this thesis, whether from experiment or simulation, are always discrete data. However, as the frequency resolution of the MTFs is quite fine ($\approx$0.015 mm^{-1}), they are in most cases displayed with solid lines as a guide to the eye.

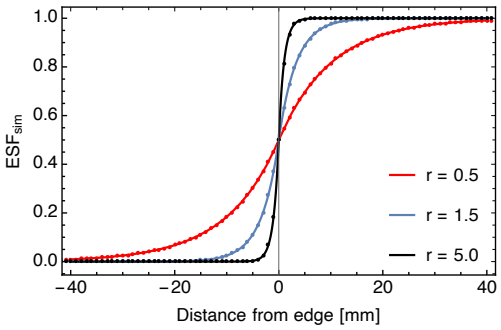

(a) Analytical edge spread function (solid line) and sampled data points used to create the edge images.

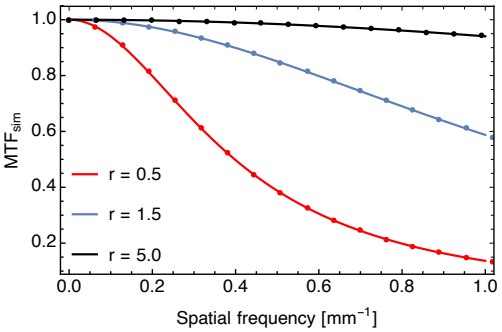

(b) Discrete MTF values obtained from Mathematica program and true MTF (solid line).

Figure 3.15: Analytical ESFs based on Eq. (3.7) with sharpness settings of r = 0.5, 1.5, 5.0 were turned into synthetic edge images, based on a sampling distance of 0.2 mm and 2.2° edge angle. The images were analyzed with the developed Mathematica program to reveal excellent agreement between the discrete (calculated) MTF values and the true (analytically obtained) MTF.

4 Results

This work starts with an experimental investigation of the impact of the edge phantom design on the MTF measurement. A method is devised which predicts the systematic error in the measurement based on Monte Carlo simulations. The influence of geometric unsharpness, absorption unsharpness and scatter at MV energies is investigated, before discussing suitable edge phantom designs for 6 MV beam quality.

4.1 MTF measurements on PortalVision aS1200

To isolate the influence of the edge phantom design, several phantoms were used to measure the detector MTF of a single MV imaging system (Varian PortalVision aS1200). Prior to that, the role of the analysis region of interest and the noise level in the edge image were addressed.

4.1.1 Defining the Region of Interest

The MTF is evaluated from a central region of interest (ROI) in the image, which contains the edge transition. The width of the ROI must be large enough to contain N_{int} rows, but has no further impact on the MTF result. The ROI length (=ESF length) determines the frequency resolution of the MTF and is set to a power of 2 before Fourier Transform. If the ROI length is set too small, the spatial frequency resolution of the MTF

will be coarse and possibly hide interesting details such as a low-frequency drop.[71,96] On the other hand, a very large ROI length creates a high resolution MTF, at the price of a higher noise level.[95]

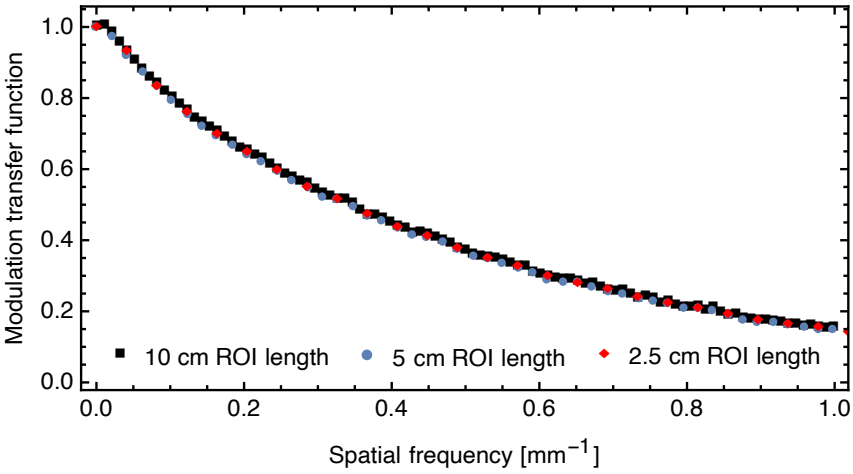

Figure 4.1: Experimentally determined detector MTF of Varian PortalVision aS1200, calculated from the image of a 5.0 cm thick lead edge phantom. Changes in the ROI length had no effect on the MTF, except for the frequency resolution.

The MTF was calculated from experimental edge images (5.0 cm lead in Fig. 4.1), using different ESF lengths of 2^{11}, 2^{12} and 2^{13} data points. These numbers are equivalent to ROI lengths of around 2.5 cm, 5.0 cm and 10.0 cm (varying slightly depending on the exact edge angle), which correspond to MTF spatial frequency resolutions of 0.04 mm^{-1}, 0.02 mm^{-1} and 0.01 mm^{-1}.

In the exemplary comparison in Figure 4.1, the MTFs show excellent agreement. The detector MTF evidently does not show a low-frequency drop, i.e. the image is free from long-range non-uniformities. The same was found for the three other phantom designs. The measured MTFs reported hereafter were calculated from either 2^{12} or 2^{13} data points, depending on the exact edge angle of the individual measurement. In most cases, they are displayed with solid lines as a guide to the eye.

4.1.2 The influence of noise in the edge image

Noise can enter into the image formation process in many ways, depending on the nature of the imaging system. Modern a-Si flat panel detectors introduce conversion noise due to the fluctuating amount of energy deposited per interacting x-ray photon in the scintillator, as well as electronic noise. In addition, like all x-ray imaging systems, they are affected by quantum noise caused by fluctuations in the incoming photon distribution.[97]

The MTF is by definition a noise-less quantity. Nevertheless, any edge image acquired with a detector will contain noise. The implications of noise on the MTF were first analyzed using synthetic edge images, for which the true MTF was known.

The noise in the MTF increases with spatial frequency (Fig. 4.2a), as the noise in the edge image is interpreted as a quick-changing signal lying over the actual edge signal. Depending on the level of noise in the image in

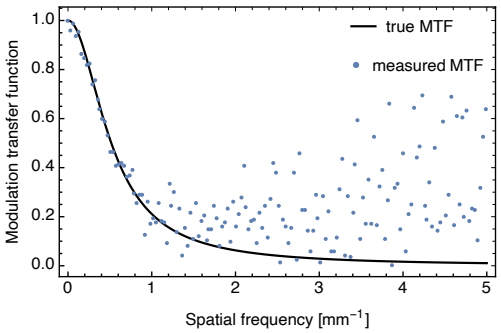

(a) Noise artificially inflates the measured MTF at higher spatial frequencies ("bias error").

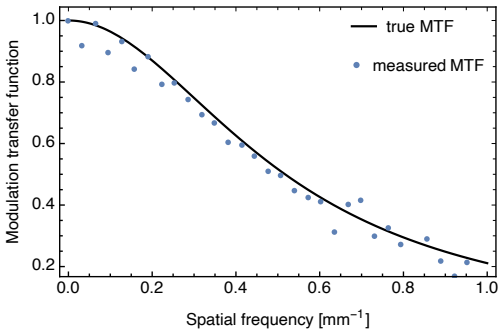

(b) Example of insufficient noise representation in the image. Odd data points are well aligned with the analytical solution, while even data points show a systematic offset.

Figure 4.2: Modulation transfer function (MTF) of a synthetic edge images (see Section 3.3.3) with added Gaussian noise ($\sigma = 3\%$ relative to signal range). Blue: MTF calculated from noisy edge image. Black: Analytical solution (true MTF).

relation to the signal range, there is the risk of a *positive bias error* in the MTF.[15,98] The bias error is an inevitable side effect of MTF calculation, as the MTF is defined as the absolute value of the optical transfer function. This way, a fluctuation that lowers the optical transfer function below zero still appears as a positive MTF value. This is especially effective at high spatial frequencies where the mean MTF tends towards zero.

In addition, some MTFs contained a conspicuous pattern, giving the impression of two MTFs lying side by side (Fig. 4.2b). While the first, third, fifth etc. data point are well aligned with the true MTF, the second, forth, sixth etc. data point show a systematic offset. This indicates that the length of the ROI used for analysis may not be sufficiently long to represent the noise spectrum.[15] The noisy edge signal can be thought to consist of two components; the ideal noise-free edge signal $esf(x)$ and the additional noise $n(x)$:

$$MTF(\xi) = \frac{\left|\mathscr{F}\left(\frac{\mathrm{d}}{\mathrm{d}x}esf(x)\right) + \mathscr{F}\left(\frac{\mathrm{d}}{\mathrm{d}x}n(x)\right)\right|}{\left|\mathscr{F}\left(\frac{\mathrm{d}}{\mathrm{d}x}esf(x)\right) + \mathscr{F}\left(\frac{\mathrm{d}}{\mathrm{d}x}n(x)\right)\right|_{\xi=0}} \tag{4.1}$$

The real part of $\mathscr{F}\left(\frac{\mathrm{d}}{\mathrm{d}x}esf(x)\right)$ alternates between positive and negative values. During MTF normalization, all data points are scaled with the same value, namely that of the (odd) zero frequency value. We assume for illustration purposes that the noise produces a constant positive offset $\mathscr{F}\left(\frac{\mathrm{d}}{\mathrm{d}x}n(x)\right) > 0$. In this case, the absolute value of the real part of the Fourier transform is increased for positive (odd) values and reduced for negative (even) values. During normalization, the absolute values in even data points are reduced even further, as they are scaled to the (increased) zero frequency value. The combined effect of taking the absolute value and scaling to zero frequency value in Eq. (4.1) leads to a significant deviation from the true MTF in every second data point.

At the beginning of the measurements on the PortalVision aS1200, the amount of noise in the edge image

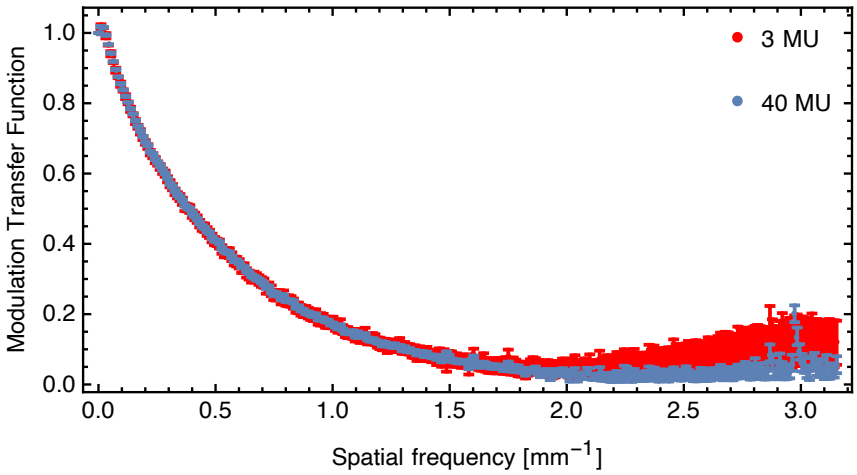

Figure 4.3: Mean MTF obtained from 3.3 cm lead phantom, measured with 3 MU and 40 MU exposure per image. Deviations from bias error start at around 2 mm^{-1}. (Error bars indicate standard error of the mean.)

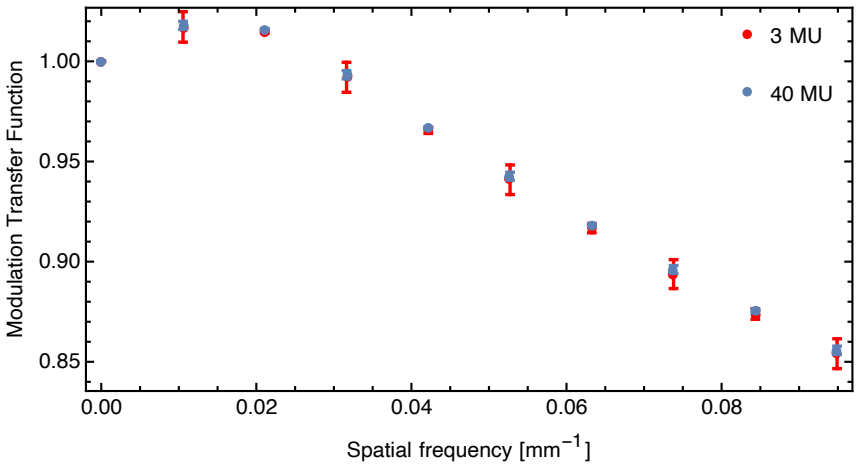

Figure 4.4: Mean MTF obtained from 3.3 cm lead phantom, measured with 3 MU and 40 MU exposure per image. Magnified for low spatial frequencies. Errors bars indicate the standard deviation, which is higher in even data points.

was analyzed to avoid both the bias error and erroneous scaling in even data points. The noise level can be adjusted via the exposure setting, i.e. the number of monitor units (MU) used to acquire an image. Ensembles of 100 edge images were acquired at 3 MU, which is typical for patient imaging, and a higher exposure of 40 MU.

When comparing the mean MTF values obtained from the ensembles, the bias error becomes apparent for spatial frequencies of 2 mm^{-1} and higher (Fig. 4.3). This behavior was found for all investigated phantom designs. The meaningful spatial frequency range for state-of-the-art MV detectors reaches only up to 1 mm^{-1}, for higher spatial frequencies the contrast is negligible. In this range, the RMS difference of the mean MTF values calculated from 3 MU and 40 MU exposures is below 0.6 %, indicating that the measurement is not subject to a bias error. The presentation of MTF results in the following sections is therefore limited to the spatial frequency range up to 1 mm^{-1}.

The noise representation in the data was analyzed by comparing the MTF standard deviation in even and odd data points, again based on ensembles of 100 images. As described above, even data points may be scaled

inaccurately depending on the noise distribution in the individual image, which increases the standard deviation of these MTF values. At very low spatial frequencies up to 0.1 mm^{-1}, the standard deviation in even data points is about four times higher than the standard deviation in odd data points, both for 3 MU and 40 MU images (Fig. 4.4). The effect gradually disappears at higher frequencies, as the overall variability in the data points increases. As expected, edge images acquired with 40 MU provide a much lower standard deviation, e.g. 0.2 % at 0.1 mm^{-1} compared to 0.8 % for 3 MU exposure. However, an exposure of 3 MU can also be used, provided that the MTF is calculated as the mean MTF from a sufficiently large ensemble of edge images so that the fluctuations in even data points are equally distributed around the mean. In the following experimental study, all edge images were acquired with 40 MU.

4.1.3 Experimental study of measurement accuracy

MTF measurements reported in the literature were conducted with different phantoms and on different detectors, which prevents a comparison of the results. To determine whether the design of the edge phantom influences the measured detector MTF, an experimental study was carried out with different phantoms on a single detector.

The MTF of a Varian PortalVision aS1200 was measured with four lead phantoms of 1.3 cm, 3.3 cm, 5.0 cm and 10.0 cm thickness. Since the range of previously reported phantoms went from 0.5 mm thin tantalum to 40 cm thick steel, all four edge phantoms would be deemed suitable according to the literature. Except for the phantom design, the measurement conditions were kept constant. The measurement uncertainty was assessed by acquiring ensembles of 100 edge images per phantom and determine the mean MTF along with the standard error of the mean (SEM). The standard error increases with spatial frequency and varies with the phantom thickness, but was found to be below 0.002 for all measurements with 40 MU exposure. When the phantom was repositioned 10 times to determine whether an additional setup error was introduced, the mean MTF values equally showed a standard error of 0.002. Given that the pixel pitch enters the MTF calculation with three significant figures, the mean MTF values presented in this thesis can safely be specified with an uncertainty of ± 0.01. As the error bars would be smaller than the symbol size, they are omitted from the following plots. Due to the high frequency resolution of the MTF ($\Delta_\xi \approx 0.015\,mm^{-1}$), the data points are joined with a line.

As seen in the edge spread functions (Fig. 4.5), the transmission through the phantoms was 53 % (1.3 cm lead), 24 % (3.3 cm lead), 12 % (5.0 cm lead) and 3 % (10.0 cm lead). By comparison, a 1 mm tungsten edge reduces the transmission to 0.1 % at kV radiations qualities RQA 3 to RQA 9.[47] The central region around the edge transition also reveals differences in the shape of the curves. As the phantom thickness increases, so does the width of the transition area and thereby the slope of the ESF.

Due to the differentiation step, the different absorption levels will not be reflected in the MTF. The MTF

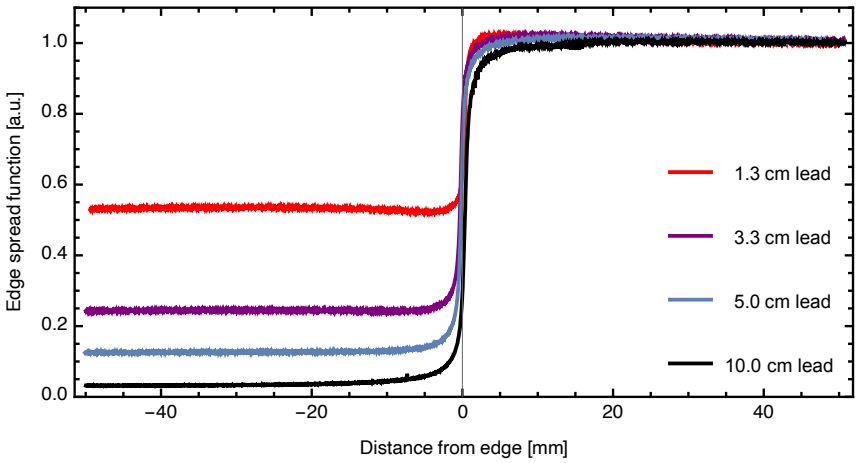

Figure 4.5: Mean ESF of four edge phantoms on Varian PortalVision aS1200 detector, obtained from ensembles of 100 edge images each.

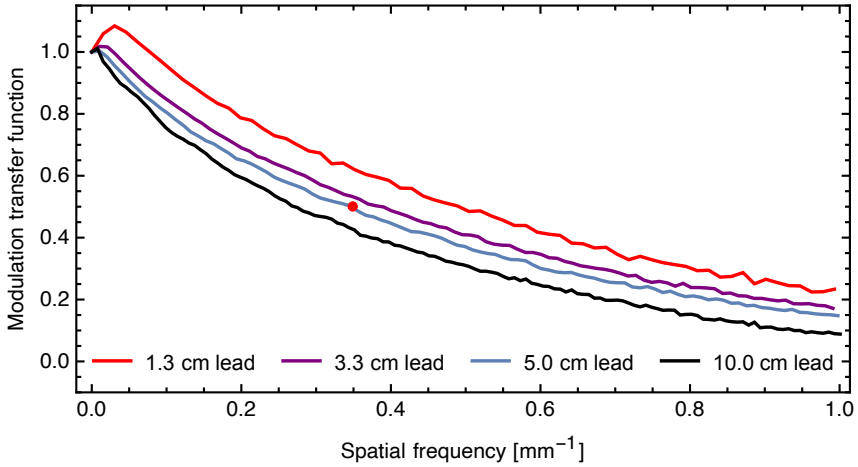

Figure 4.6: MTF of the Varian PortalVision aS1200 detector, acquired with edge phantoms made of lead with a thickness of 1.3 cm, 3.3 cm, 5.0 cm and 10.0 cm. Red dot indicates MTF_{50} specified by the manufacturer.

only depends on the relative slope that describes the edge transition. The measured detector MTFs (Fig. 4.6) showcase profound discrepancies between the four phantoms. Generally speaking, a thicker phantom results in overall lower MTF values. The differences between the MTFs increase with spatial frequency. If, as an example, the 5.0 cm lead phantom is set as the reference MTF, the other phantoms cause deviations in MTF at 1 mm^{-1} of more than 50% in both directions. The spatial frequency at which the modulation has dropped to 50 %, MTF_{50}, was determined at 0.49 mm^{-1}, 0.39 mm^{-1}, 0.35 mm^{-1} and 0.27 mm^{-1} from thinnest to thickest phantom. The manufacturer specifies the MTF_{50} at 0.35 mm^{-1}. It is unknown under which measurement conditions this value was determined, but it can be noted that it best matches the MTF measured with 5.0 cm lead. Another striking feature is the MTF peak value of 1.08 produced at around 0.05 mm^{-1} by the 1.3 cm lead phantom. This is surprising in so far as the detector MTF should not be able to take values greater than unity by definition. The effect is less pronounced, but still visible, for the 3.3 cm lead phantom. This overshoot strongly indicates that the underlying detector input signal is not a genuine step function.

To briefly paraphrase, measuring the MTF of a single MV detector with different phantoms has revealed notable differences which can only be attributed to the phantom's design. From measurement alone, it is impossible to determine which result is closest to the "true" detector MTF. The measurement accuracy can only be assessed if the detector input signal is known. This is investigated in the following sections, using Monte Carlo simulations of edge phantoms.

4.2 The detector input signal and the phantom MTF

Measuring the presampled detector MTF is based on providing a well-defined input for the detector and observing the result. For MV systems, there appear to be several difficulties to achieve such a detector input. The edge spread function of the detector is defined as the detector response to a step function input $\mathrm{H}(x)$:

$$\mathrm{ESF}_{det}(x) = \mathrm{H}(x) \star \mathrm{PSF}_{det}(x) \tag{4.2}$$

In reality, the edge image is acquired based on a detector input signal, $\mathrm{DIS}(x)$, provided by the edge phantom. If the phantom design is unsuitable for the given beam quality, the detector input signal will deviate from the required step function shape. The three most likely influences on the detector input signal are geometric unsharpness and absorption unsharpness, both of which can be described by a convolution operation, and scatter. We can therefore express the detector input signal as the convolution of a step function with a point spread function for both geometric and absorption unsharpness, $\mathrm{PSF}_{blur}(x)$, to which a scatter point spread function, $\mathrm{PSF}_{scat}(x)$, is added:

$$\mathrm{DIS}(x) = \mathrm{H}(x) \star \mathrm{PSF}_{blur}(x) + \mathrm{PSF}_{scat}(x) \tag{4.3}$$

The measured edge spread function is then the response to the detector input signal:

$$\mathrm{ESF}_{meas}(x) = \mathrm{DIS}(x) \star \mathrm{PSF}_{det}(x) \tag{4.4}$$

If the detector input signal deviates from a step function, the MTF evaluated from this edge spread function will not be the true detector MTF:

$$\mathrm{MTF}_{meas}(\xi) \neq \mathrm{MTF}_{det}(\xi) \tag{4.5}$$

Min et al. have proposed that the phantom whose ESF most closely resembles an ideal step function is most likely to give accurate MTF results.[66] This is not entirely correct. Without knowing the detector response, it is impossible to infer from the ESF that the detector input signal is suitable. Part of this work was the development of the following technique to quantify the measurement error resulting from the phantom design: The detector input signal can be analyzed in the same way as a measured edge spread function, i.e. differentiated, Fourier transformed and scaled to the zero frequency value. We will call the resulting frequency spectrum the *phantom*

MTF:

$$\mathrm{MTF}_{phantom}(\xi) = \frac{\left|\mathscr{F}\left(\frac{\mathrm{d}}{\mathrm{d}x}\mathrm{DIS}(x)\right)\right|}{\left|\mathscr{F}\left(\frac{\mathrm{d}}{\mathrm{d}x}\mathrm{DIS}(x)\right)\right|_{\xi=0}} \tag{4.6}$$

In case of an ideal step function input, the phantom MTF will be unity at all spatial frequencies. If the detector input signal deviates from the step-like profile, the difference between the phantom MTF and unity will display the systematic error introduced by the phantom design. We will employ this tool to determine the achievable accuracy of an MTF measurement. Note that the phantom MTF is not an MTF as defined by linear-systems theory and does not describe a subsystem in the imaging chain. It is simply the differentiated and Fourier transformed input signal.

As each image acquired with a detector entails the convolution with the detector point spread function, the detector input signal cannot be extracted by measurement. However, it can be obtained from Monte Carlo simulations. By simulating the particle transport through the measurement geometry, the photon distribution in the image plane - equivalent to the detector input signal - can be scored. The remainder of this thesis describes the influence of the phantom design on the MTF measurement accuracy by analyzing the detector input signal produced by each phantom.

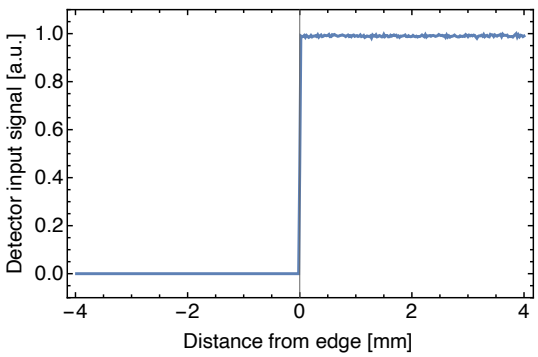

(a) The detector input signal (= photon fluence) of the idealized edge phantom follows the desired step function shape.

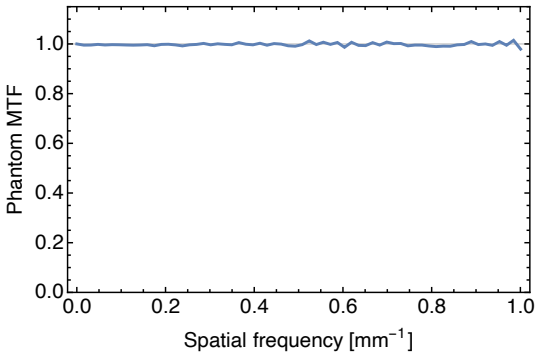

(b) The phantom MTF shows a constant value of unity, which indicates that the phantom does not introduce a systematic error in the MTF measurement.

Figure 4.7: Monte Carlo simulation of a thin, completely absorbing edge phantom placed in direct contact with the detector.

For a quick demonstration of the above procedure, the simulation and analysis of an ideal edge phantom is included at this point. The ideal edge phantom is thin, highly absorbing and placed in direct contact with the detector during MTF measurement. This situation was recreated in a Monte Carlo simulation by taking a 1 mm thick lead phantom and idealizing it to show complete absorption. This was achieved by setting the electron and photon cut-off energies within the geometric boundaries of the phantom to a value higher than the maximum

particle energy generated by the linear accelerator. Any particle that enters the phantom will terminate its history immediately. Thus, the phantom is completely absorbing and does not produce any secondary particles. Placed just in front of the scoring plane, this phantom design leads to a perfect step-function input signal (Fig. 4.7a). Analysis of the signal reveals a phantom MTF which is unity at all spatial frequencies, proof-of-principle that the simulated phantom does in fact behave ideal (Fig. 4.7b).

The Monte Carlo simulations of real phantoms presented in the following sections will be conducted in a similar fashion. Note that from here on, the detector itself is no longer part of the investigation. The simulations model the particle transport up to the imaging plane, but do not include the detector. The analysis is focussed exclusively on the detector input signal, which makes the results applicable to any detector operating with a comparable beam quality. This not only includes other EPIDs, but also 2D ionization chamber arrays used for quality assurance of linear accelerators.

The developed method to quantify the systematic measurement error via the phantom MTF was used to analyze the behavior of the four lead phantoms used on the PortalVision aS1200 detector. Monte Carlo simulations revealed the photon fluence at the imaging plane, which is equivalent to the detector input signal. The signals were processed to determine the phantom MTF for each phantom.

The uncertainty of a simulation is expressed by the standard error of the mean (SEM) specified for each data point in the detector input signal (see Eq. (3.1)). The relationship between noise in the detector input signal and noise in the MTF is non-linear[99], which makes it difficult to estimate the standard error in the phantom MTF. However, the uncertainty in the detector input signals obtained from Monte Carlo simulations was about one order of magnitude lower than the uncertainty in the measured edge spread functions. It is therefore possible to specify the uncertainty in the phantom MTF with ± 0.01, analogous to the uncertainty in the measured detector MTF. Once again, the error bars are not displayed as they would be smaller than the symbol size and the data points are joined with a line ($\Delta_\xi \approx 0.016\,\mathrm{mm}^{-1}$).

The Monte Carlo simulations of the phantoms give access to the photon fluence as it is "seen" by the detector (Fig. 4.8). It is immediately apparent that the phantoms produce very different detector input signals. While it is natural that the level of absorption varies, there are two conspicuous details about the shape of the signals: Firstly, there are distortions around the edge transition that are similar to the behavior of an edge enhancement effect. These distortions are most pronounced in the thinnest phantom, and gradually decline with phantom thickness. Secondly, the signal of the 10.0 cm lead phantom shows an ideal step directly below the phantom, but is sloped coming from the side of the open field.

The corresponding phantom MTFs show the systematic error which is present in the MTF measurements

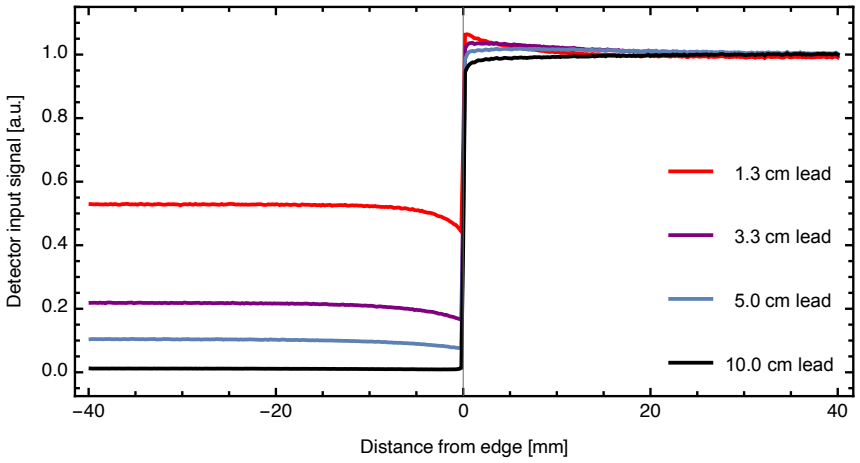

Figure 4.8: Detector input signal (= total photon fluence) created by the four experimentally investigated lead edge phantoms (1.3 cm, 3.3 cm, 5.0 cm and 10.0 cm thickness) at the imaging plane (SID 180 cm). Obtained from Monte Carlo simulations.

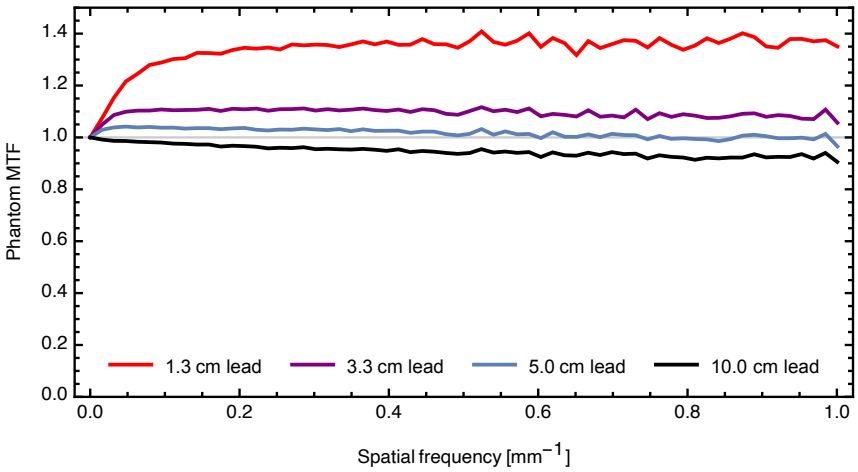

Figure 4.9: Phantom MTFs of the four experimentally investigated lead edge phantoms (1.3 cm, 3.3 cm, 5.0 cm and 10.0 cm thickness) in direct contact with the detector at SID 180 cm.

by the deviation from unity (Fig. 4.9). The illuminating conclusion we can draw from this comparison is that the detector MTF can be both over- and underestimated, depending on the design of the phantom. For the four phantoms shown here, the error ranges roughly from -9 % to +35 % and shows a dependence on spatial frequency. Looking back, the discrepancies between the measured MTFs in the experimental study (Fig. 4.6) appear to match the systematic errors seen in this analysis, with thinner phantoms producing overall higher MTF values. The 5.0 cm lead phantom looks most promising in terms of accuracy. This would fit in with the agreement found between the MTF measured with this phantom and the manufacturer-specified MTF_{50}.

The question is: What are the underlying physical effects that contribute to the signal distortions? Based on the answer, it may be possible to devise phantom designs that achieve higher measurement accuracy. Three effects have been mentioned that have the potential to influence the detector input signal. They are 1) geometric unsharpness from the finite source size, 2) absorption unsharpness from varying absorption lengths in a thick phantom and 3) scatter produced within the phantom. In order to distinguish between the effects, the detector input signal was separated into primary and secondary radiation. If the primary radiation, which had no interaction with the phantom, deviates from the desired step function, this must be due to geometric unsharpness or absorption unsharpness. The secondary radiation, on the other hand, will showcase the distribution of secondary particles produced within the phantom, e.g. by Compton scattering.

4.3.1 Analysis of primary radiation

During a Monte Carlo simulation, the history of each particle is recorded in terms of how and where it has interacted (see *LATCH variable* in Section 3.3.2). This information was used to filter the phase space and score only that part of the detector input signal which stems from primary photons. The fluence component attributable to primary radiation was analyzed similar to the total fluence.

At first glance, the primary radiation of all four phantoms appears to be very close to a step-function profile (Fig. 4.10). Obvious differences arise from the change in transmission, which ranges from 34 % for 1.3 cm lead over 10 % and 4 % for 3.3 cm and 5.0 cm lead, respectively, to 0.3 % for 10.0 cm lead. Less obvious is the gradual change in shape: The magnified view of the edge transition reveals how the profile gradually slopes with increased phantom thickness. The central region of the detector input signal transforms from a right angle (1.3 cm lead) to a shoulder curve (10.0 cm lead). This effect only occurs on the open field side of the edge transition. Coming from the phantom side, the transition appears as a right angle. Furthermore, the primary radiation below the phantoms forms a plateau that appears constant throughout.

Although the detector input signals appeared to be quite similar apart from the absorption levels, the differences between the phantoms become apparent in the phantom MTFs (Fig. 4.11). At very low spatial frequencies up to 0.1 mm^{-1}, the measurement results coincide with the true detector MTF. However, with higher spatial frequencies, the measured MTFs increasingly underestimate the true MTF. Over the frequency range analyzed here, the decline is approximately linear. The systematic error at 1 mm^{-1} spatial frequency grows from -3 % for 1.3 cm lead to -9 % for 10.0 cm lead.

Can these findings be explained by geometric and/or absorption unsharpness? If the beam divergence led to significant changes in the absorption length within the central region of 80 mm over which the MTF is evaluated, then this would be shown by sloping tails in the signal profile - which are not present. On the other hand, the observed slope in the central region fits the description of geometric unsharpness: While the phantom exit plane is in contact with the detector, the thickness of the phantom causes the entrance plane to be elevated to a certain height. Thus, the projection of the entrance plane could be influenced by extrafocal radiation even though the phantom is in direct contact with the detector. In a way, the situation bears resemblance to the introduction of an air gap, only that half of the air gap is filled with phantom material. This would also explain

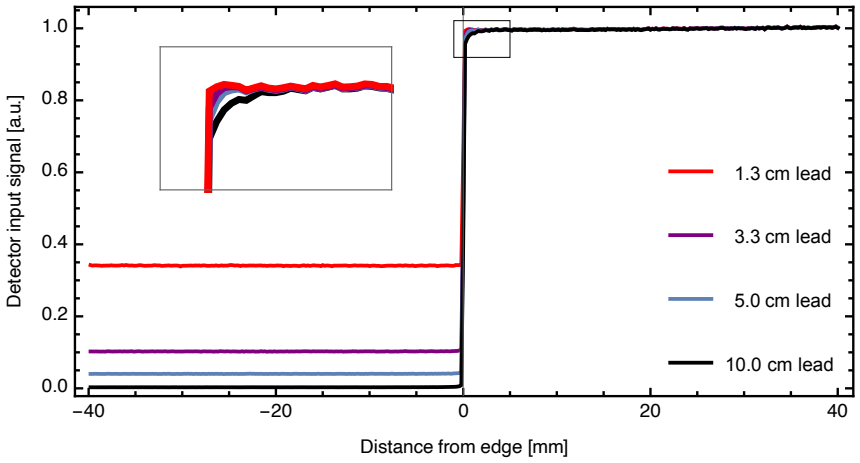

Figure 4.10: Detector input signal attributable to primary radiation for four edge phantoms at 6 MV beam quality (obtained from Monte Carlo simulations). Magnified view reveals small deviations from the desired step-function profile that appear with increasing phantom thickness.

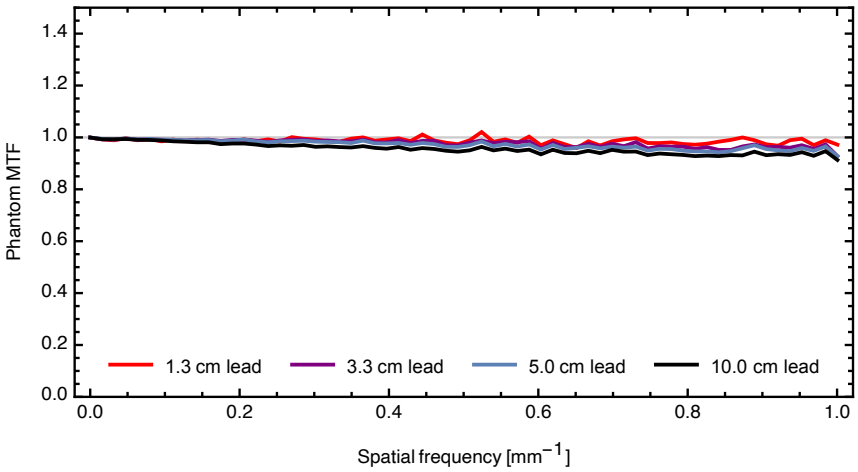

Figure 4.11: Phantom MTF derived from primary radiation alone, excluding the influence of scatter or bremsstrahlung. The measured MTF underestimates the true MTF. The systematic error increases with phantom thickness and spatial frequency.

why the effect is only visible in the open field: Extrafocal radiation which originates from the side of the open field will pass through the phantom, whereby most of it will be absorbed. Thus, the results indicate that the primary component of the detector input signal is dominated by geometric rather than absorption unsharpness.

To prove this point, the simulation for the 10.0 cm lead phantom, which showed the largest deviations in primary radiation and in which the influence of geometric unsharpness would be most pronounced, was repeated. This time, the TrueBeam linear accelerator was modeled as a point source with an underlying 6 MV spectrum instead of using TrueBeam phase space data. The idea is that geometric unsharpness can only occur in a system with a finite source size, while absorption unsharpness stems from the beam divergence and must be present in both simulations.

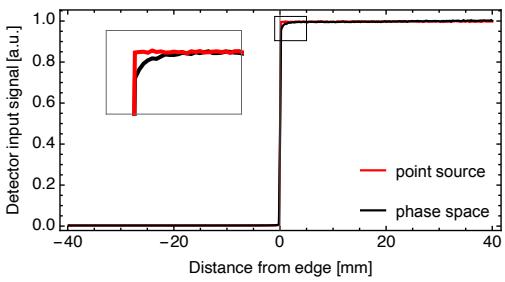

(a) Comparison of detector input signals. The implementation of a point source eliminates geometric unsharpness from the simulation.

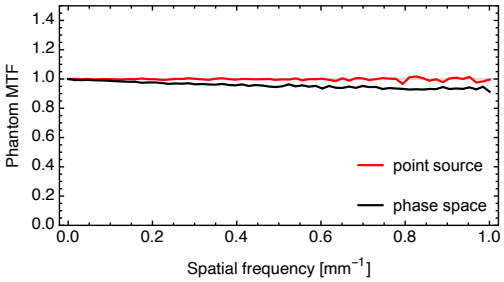

(b) The phantom MTF from the point source implementation results in a constant value of unity, which shows that the signal is free from absorption unsharpness.

Figure 4.12: Monte Carlo simulation of 10.0 cm lead edge phantom in contact geometry (SID 180 cm, 6 MV beam quality). The accelerator is modeled as a point source or using a full phase space.

The fluence distribution behind the 10.0 cm lead phantom features a picture-perfect edge transition without the slightest slope when the photon beam is modeled as a point source (Fig. 4.12a). Evidently, the distortion

observed in the simulation with the complete phase space must stem from extrafocal radiation, as the only difference between the simulations is the size of the focal spot. The phantom MTF obtained by the point source simulation is unity over the spatial frequency range of interest, the deviations lie within the statistical uncertainty (Fig. 4.12b). This verifies the hypothesis that the influence of absorption unsharpness on MTF measurement accuracy is insignificant. The detector input signal is evidently not influenced by differences in the absorption length within the phantom.

To finalize the discussion about absorption unsharpness, we can do a back-of-the-envelope calculation to estimate the maximum change in absorption length in the given geometry. The ROI for MTF calculation is 4 cm in each direction from the edge transition. Assuming a point source at the source-to-imager distance (SID) of 180 cm, the maximum angle due to beam divergence is $\varphi = \arctan(\frac{4\,\mathrm{cm}}{180\,\mathrm{cm}}) \approx 1.3°$. The minimum absorption length is the phantom thickness t. The maximum absorption length t' is given by $t' = \frac{t}{\cos(\varphi)}$. The relative difference in absorption length amounts to $t'/t = 1.0003$ in the present geometry, which is insignificant. As it is independent of the phantom thickness, the result holds true even if a phantom with 40 cm thickness or more were to be used. To induce a potentially meaningful change of 5% in the absorption length, the SID would have to be reduced to an unreasonable (and impractical) value of 12 cm. We can therefore definitely conclude that the influence of absorption unsharpness on the detector input signal is negligible and need not be considered while optimizing the phantom design with regard to MTF measurement accuracy.

The simulation presented here also solves an existing conflict with prior work: In this thesis, first the fundamental considerations and then the experimental study in Section 4.1.3 pointed to the fact that the phantom design has significant influence on the result of an MTF measurement. This stood in contrast to statements made by Sawant et al., who saw no differences in the outcome of simulations conducted for 5 cm, 10 cm and 19 cm tungsten, as well as 10 cm, 20 cm and 40 cm steel phantoms.[33] In the study outline, the authors note that the linear accelerator was modeled as a point source. This effectively removed the influence of geometric unsharpness from the simulation and gave the impression that phantom thickness was of no consequence to the measurement accuracy. The results shown here illustrate that Monte Carlo simulations for any situation in which geometric unsharpness cannot be excluded ought to be implemented using the full phase space rather than a point source. The conclusion drawn by the authors, namely that changes in the thickness of a phantom have no effect on the measurement result, is not valid as it is based on incorrect simulations. Similar conclusions can be drawn for simulations with a parallel beam[58,64], which not only removes the influence of geometric unsharpness, but also absorption unsharpness.

Geometric unsharpness in linear accelerators It was established that the deviations of primary radiation are caused by geometric unsharpness. The last question to be answered here is whether geometric un-

sharpness in linear accelerators follows the geometrical definition given in Eq. (2.40). In principle, the formula should be valid for any radiation source, provided that it is defined by sharp boundaries and produces a uniform photon distribution. Rossmann and Lubberts have demonstrated the applicability for an x-ray tube emitting 70 kVp radiation.[39] As of yet, there have been no reports of the geometric unsharpness introduced by an MV imaging system on a clinical linear accelerator.

Additional simulations were performed to mimic the theoretical situation of an infinitesimally thin, radiopaque edge phantom, positioned somewhere between source and detector. The phantom was idealized as described before by setting the electron and photon cut-off energies to a value higher than the maximum particle energy. In addition to the 80 mm trace with 0.2 mm resolution from which the phantom MTF is calculated, the detector input signal was sampled at a finer spacing of 0.02 mm in the central region of 8 mm around the edge transition. To induce penumbras of significant width, the geometries were created with comparatively high magnification factors. The source-to-imager distance was fixed to SID 180 cm. Three phantom-to-imager distances of d=20 cm, d=36 cm and d=60 cm were simulated, creating ratios of $d/D = 1/8$, $d/D = 1/4$ and $d/D = 1/2$, respectively.

Based on the theory, the detector input signal ought to show a linear transition between two plateaus. The simulation results show that the detector input signal progresses along a shoulder curve instead of a linear transition (Fig. 4.13a). This suggests that the source emits an inhomogeneous photon distribution and has blurred boundaries. Further indication for this is the overall trend of the signal, visible in the regions left and right from the transition, which fail to establish a plateau. Apparently, the unsharpness extends wider than the scored 8 mm region, possibly introduced by scatter from the collimating system. To quantify the unsharpness, the penumbra w was subsequently calculated as the width over which the edge transition changes from 20 % to 80 %. For the geometries $d/D = 1/8$, $d/D = 1/4$ and $d/D = 1/2$, the calculation returned penumbras of 0.16 mm, 0.31 mm and 0.60 mm width, respectively. These values demonstrate that the central region of the edge transition scales approximately linear with d/D, despite the overall sigmoid shape of the signal. As the exact source size f is unknown, the width of the penumbras cannot be verified. However, using the formula in reverse to calculate the source size from the penumbras returns a value around 1.25 mm, which fits into the plausible range of 1-2 mm for linear accelerators.

The phantom MTFs are clearly devoid of any sinc pattern (Fig. 4.13b). This is understandable, as the detector input signal deviates so much from the theoretical shape and the discontinuities at the boundaries of the penumbra are replaced by gradual slopes. Consequently, the phantom MTFs drop to zero somewhere around $\xi_0 = 1/w$ and remain thus for higher spatial frequencies. All phantom MTFs drop rapidly at the beginning of the curve, until about 0.1 mm^{-1} spatial frequency. A low frequency drop like this stems from long-range deviations (e.g. scatter[100] or veiling glare[101]). Here it will be the result of the overall trend of the detector input

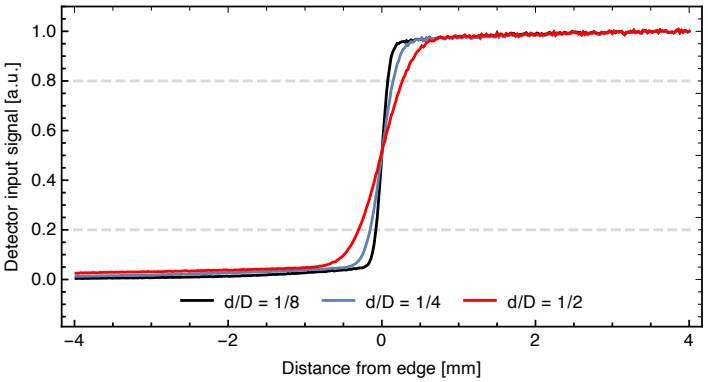

(a) The central region of the transition scales approximately linear with d/D.

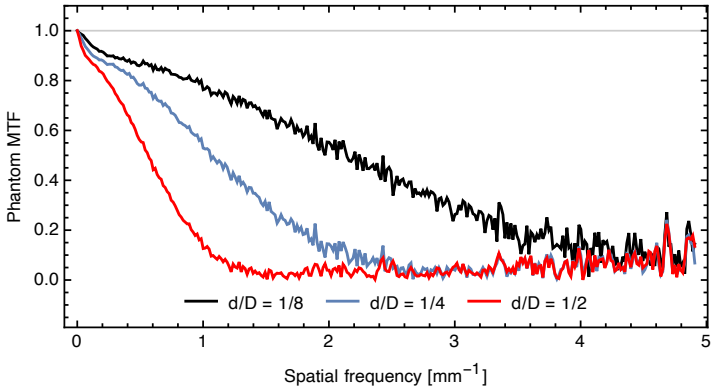

(b) The MTF attributable to geometric unsharpness does not exhibit a sinc pattern.

Figure 4.13: Geometric unsharpness introduced by Varian TrueBeam 6 MV radiation. Simulation of an ideal edge phantom with negligible thickness and complete absorption in air gap geometry. SID fixed to 180 cm, phantom-to-imager distance d was varied.

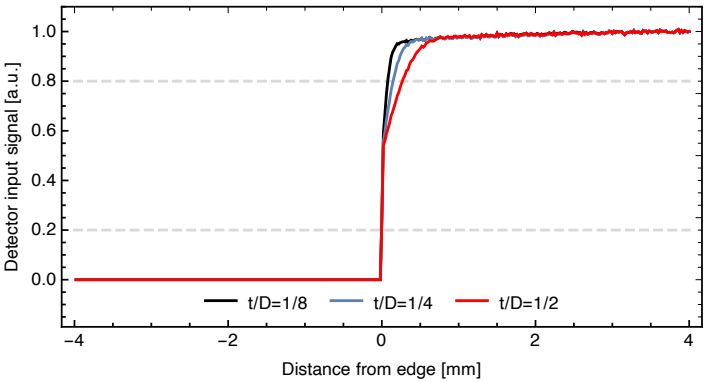

(a) A thick, idealized phantom creates a one-sided unsharpness. The distribution in the open field equals that of a thin phantom at distance in air gap geometry (Fig. 4.13a).

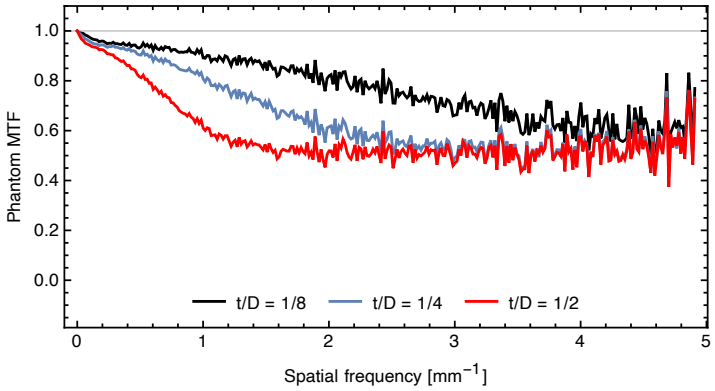

(b) The right angle present in the detector input signal offers high-frequency components which increase the MTF values.

Figure 4.14: Simulation of a thick, completely absorbing phantom in contact geometry (Varian TrueBeam 6 MV photon beam, SID 180 cm). The phantom thickness t equaled the phantom-to-imager distance d in the previous simulation (Fig. 4.13).

signal. To summarise, it can be noted that the radiation source of a linear accelerator is less sharply defined than the focal spot of an x-ray tube, so that the geometric definition given by Eq.(2.40) can only serve as a rough approximation.

In a second study, the above simulations were repeated with the phantom extending all the way to the image plane, i.e. mimicking the MTF measurement with a thick edge phantom (d=t=20 cm, 36 cm, 60 cm) in contact geometry.

The detector input signal in the area below the phantom is ideal due to complete absorption (Fig. 4.14a). In the open field, the signal exactly matches the distribution created by a thin phantom at the same distance d from the imager. In consequence, the penumbras are half as large as determined above and shifted off-center. The overall effect could be described as a "one-sided" geometric unsharpness. The semi-ideal detector input signal creates an interesting outcome in the phantom MTF (Fig. 4.14b): For one thing, the MTF values are larger at all spatial frequencies. Furthermore, the phantom MTFs do not drop to zero as before, but stabilize at a value of 0.5. This can be attributed to the sharp edge in the signal distribution below the phantom, which provides previously missing high frequency components. The results of this study will regain importance when discussing strategies for optimizing the MTF measurement accuracy.

4.3.2 Analysis of secondary radiation

The above exercise was repeated with secondary radiation, only scoring those particles which originated from within the phantom. To determine the influence on the accuracy from scatter alone, the scatter distribution of each phantom was added to an idealized primary distribution, which showed the same absorption level as the original primary distribution, but featured a perfect step-function profile. The phantom MTF thus shows the systematic error that occurs from secondary radiation alone, without the influence of geometric unsharpness.

The distribution of secondary radiation is found to depend strongly on the phantom thickness (Fig. 4.15). For the 1.3 cm lead phantom, the distribution resembles a step function, with the direction of the step inverted compared to the primary signal. Photons are mainly forward scattered to the detector, but the profile extends several centimeters into the area of the open field. This distribution is closest to the reports by Neitzel et al.[47] for partially absorbing edge phantoms at kV radiation qualities (compare Section 2.5.4). With larger phantom thickness, the entire shape of the distribution changes: The level of forward scattered phantoms is reduced, indicating that part of the radiation created within the phantom is absorbed before it reaches the detector plane. On the other hand, the amount of photons scattered into the open field is actually higher in thicker phantoms. In addition, we can observe that the scatter distribution expands further into the open field.

There are two possible origins for the photons detected in the open field. They can stem from scatter events taking place near to the edge, or they might arise from backscatter which is created as extrafocal radiation hits the

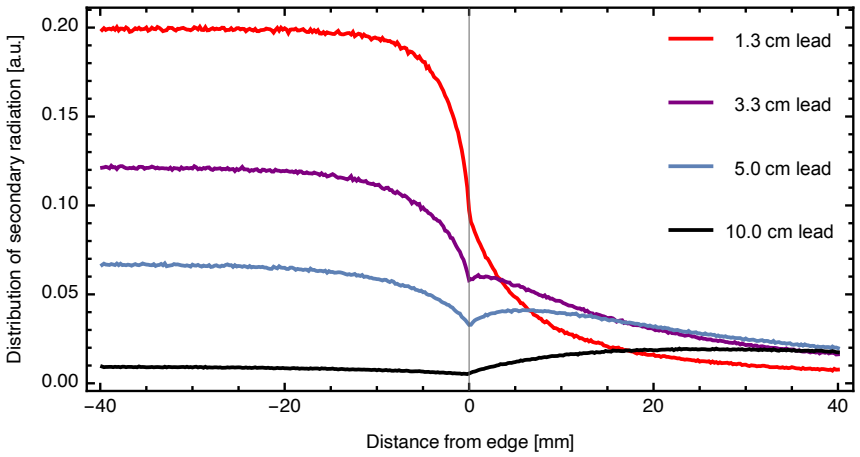

Figure 4.15: Distribution of secondary radiation below lead edge phantoms of 1.3 cm, 3.3 cm, 5.0 cm and 10.0 cm thickness. Left side: below phantom. Right side: open field.

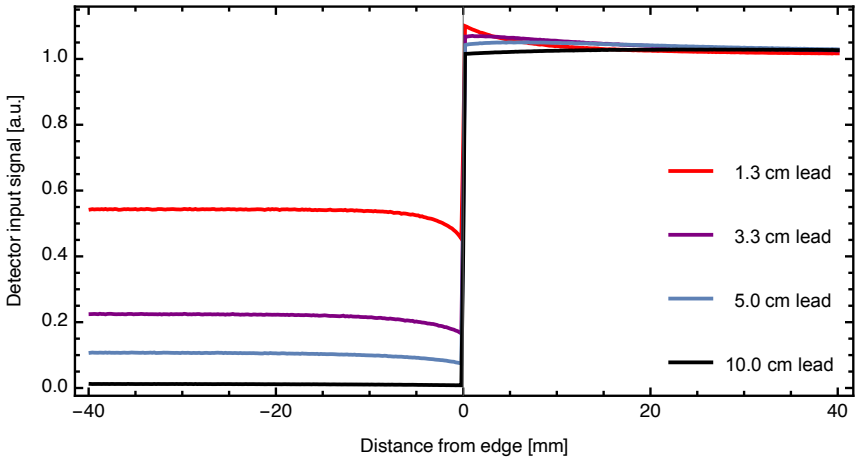

Figure 4.16: Detector input signal of lead edge phantoms, based on above scatter distribution and idealized primary distribution (eliminating influence of geometric unsharpness).

side wall of the phantom. An additional simulation with a point source (no extra-focal radiation, no backscatter) showed no difference to the previous result, so that backscatter can be considered negligible. When the phantom thickness increases, the upper part of the phantom is at a larger distance from the detector. Photons from scatter events near the edge propagate with an angular distribution, according to the photon energy, so that the distance of the scatter origin from the detector determines the width of the scatter distribution. The increasing amount of scatter in the outer region of the open field is therefore understandable.

Once the signal from secondary radiation is added to an idealized primary signal, it becomes evident how the scatter contorts the primary signal for thin phantoms (Fig. 4.16). Since the distribution of secondary radiation for the 1.3 cm lead phantom is more or less inverse to the absorption profile given by primary radiation, the sum of both components forms the observed edge enhancement. Although less pronounced, the effect is still clearly visible for 3.3 cm and 5.0 cm lead. The scatter distribution of the 10.0 cm phantom showed that most forward-scattered particles are absorbed within the phantom, but photons scattered sideways will reach further

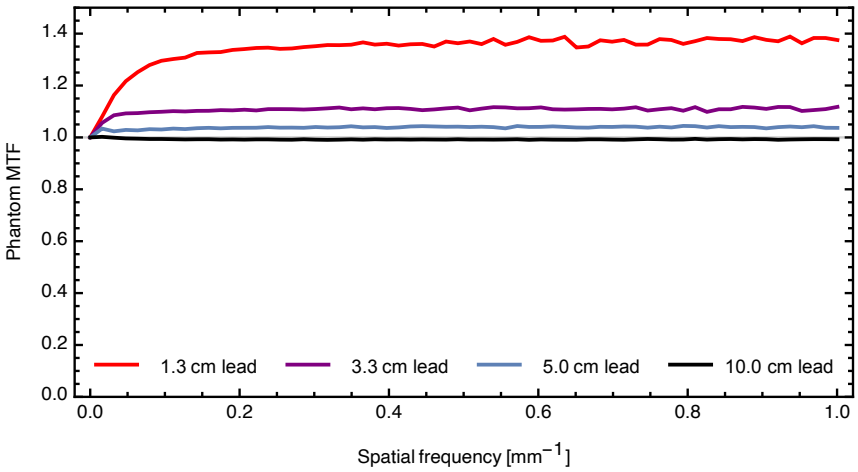

Figure 4.17: Phantom MTF derived from secondary radiation (in addition to idealized primary radiation), excluding geometric unsharpness. The measured MTF overestimates the true MTF in the presence of scatter or bremsstrahlung.

out. Here, this is seen in a small upwards trend of the signal over the width of the open field.

Although the scatter distributions are quite heterogeneous in shape, their effect on the MTF is similar: When the distribution behaves as an inverse step function and creates distortions around the edge transition, the measured MTF overestimates the true MTF. The systematic error shows a build-up to values above 1.0 and afterwards remains constant with spatial frequency. This is in accordance with the results reported by Neitzel et al. (Section 2.5.4). The effect can be observed for the 1.3 cm, 3.3 cm and 5.0 cm phantom, where the error amounts to 38 %, 12 % and 4 %, respectively. The exception is the thick 10.0 cm lead phantom, where the scatter distribution was not inverse to the profile of the corresponding primary radiation. In this case, there is no edge enhancement effect and the measured MTF is slightly smaller than the true MTF (-0.7 %).

The MTF is very sensitive to changes in the distribution of secondary radiation. The systematic errors are overall larger and more divergent compared to the errors introduced by geometric unsharpness. The theoretical model presented by Neitzel et al. cannot be used with 6 MV radiation, as the scatter distribution is very different from the one observed at kV radiation qualities. However, it was confirmed that, if present in significant quantities, scatter will lead to a pronounced MTF overestimation. Therefore, whenever the values of a measured detector MTF exceed the zero frequency value of 1.0, this is a strong indication that the detector input signal is impaired by scatter.

4.3.3 Systematic error introduced by lead phantoms

The individual analysis of primary and secondary radiation showed that while absorption unsharpness can be neglected, MTF measurements will be subject to influences from geometric unsharpness and scatter, possibly at a large scale. Unfortunately, the effects of geometric unsharpness and scatter are diametrically opposing. While geometric unsharpness is reduced when a thinner phantom is used, a thicker phantom would be more suitable

to prevent scatter. This implies that a compromise must be found to achieve the highest overall measurement accuracy.

The trade-off between geometric unsharpness and scatter becomes evident when the detector input signal and the phantom MTF are shown along with the respective contributions (Fig. 4.18 and Fig. 4.19). The phantom MTF for 1.3 cm lead is dominated by deviations from secondary radiation, while geometric unsharpness is negligible (Fig. 4.19a). The opposite applies for the 10.0 cm thick phantom, where the influence of secondary radiation is negligible and the total MTF coincides with the MTF component from primary radiation (Fig. 4.19d). Between these extremes, a balance can be established, as the overestimation from secondary radiation is compensated by the effects of geometric unsharpness. However, as the impact from secondary radiation is constant with spatial frequency, while the impact of geometric unsharpness increases with spatial frequency, the compensation can only be effective within a certain spatial frequency range.

The absolute systematic error introduced to the MTF measurement by the 1.3 cm lead phantom amounts to a constant value of +35 % after the initial build-up. For 10.0 cm lead, the systematic error increases steadily with spatial frequency to a value of -9 % at 1 mm^{-1}. The phantoms with an intermediate thickness of 3.3 cm and 5.0 cm lead show both the initial build-up, as well as the decrease with spatial frequency (Table 4.1). Each phantom introduces a deviation of several percent at some point within the spatial frequency range up to 1 mm^{-1}. In contrast, the systematic error due to phantom design at kV energies can be limited to 0.1 %. [47] Judging by the significant differences in the outcome between these phantoms, it should be legitimate to question the comparability of detector MTFs reported in the literature.

	Phantom MTF 0.1 mm^{-1}	**Phantom MTF 0.5 mm^{-1}**	**Phantom MTF 1.0 mm^{-1}**
Lead, 1.3 cm	1.29	1.35	1.35
Lead, 3.3 cm	1.11	1.09	1.06
Lead, 5.0 cm	1.04	1.01	0.97
Lead, 10.0 cm	0.98	0.94	0.91

Table 4.1: Phantom MTF at selected spatial frequencies derived from Monte Carlo simulations for four experimentally investigated edge phantoms at 6 MV beam quality and SID 180 cm. The MTF values indicate the systematic measurement error introduced by the phantom design by their deviation from unity.

The results confirm the hypothesis that the phantom design can have substantial influence on the measured detector MTF. Looking back at the MTF measurement on the PortalVision aS1200 (see Section 4.1.3), the phantom MTFs mimic the characteristics observed in the measured detector MTFs, most notably the MTF peak values greater than 1.0, the overall decrease of MTF value with phantom thickness and the increase of the measurement differences with spatial frequency.

The absolute values of the phantom MTF at select spatial frequencies confirm that the most accurate measurement result was obtained with the 5.0 cm lead phantom. In the spatial frequency range up to 1 mm^{-1}, this phantom introduces a maximum error of less than 5 %.

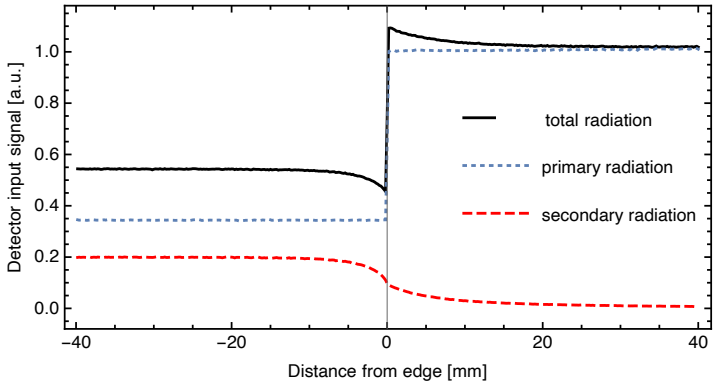

(a) Lead phantom, 1.3 cm thick.

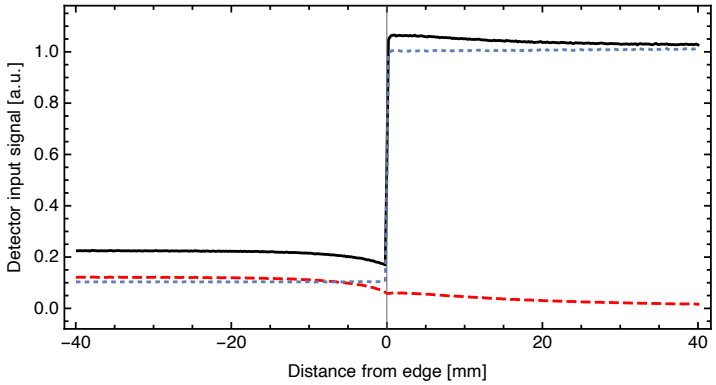

(b) Lead phantom, 3.3 cm thick.

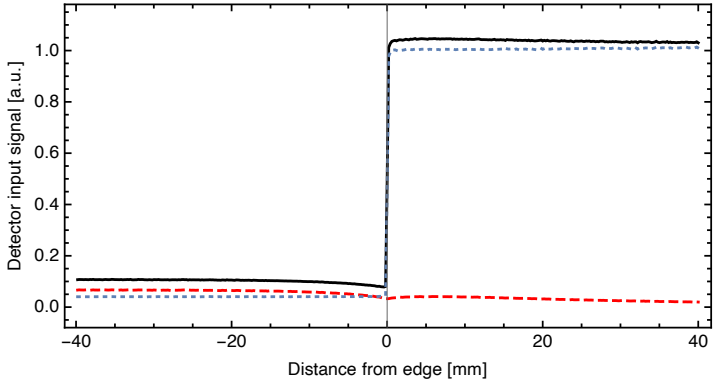

(c) Lead phantom, 5.0 cm thick.

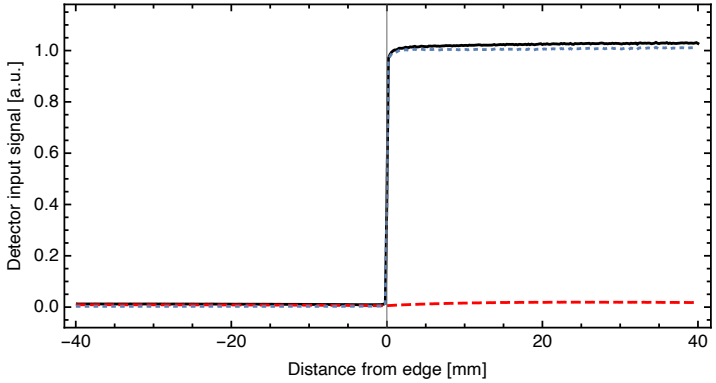

(d) Lead phantom, 10.0 cm thick.

Figure 4.18: Detector input signal produced by edge phantoms made of lead with a thickness of (a) 1.3 cm, (b) 3.3 cm, (c) 5.0 cm and (d) 10.0 cm at 6 MV beam quality in SID 180 cm. Total photon fluence (black), fluence from primary radiation (blue), and fluence from secondary radiation (red) were obtained by Monte Carlo simulation.

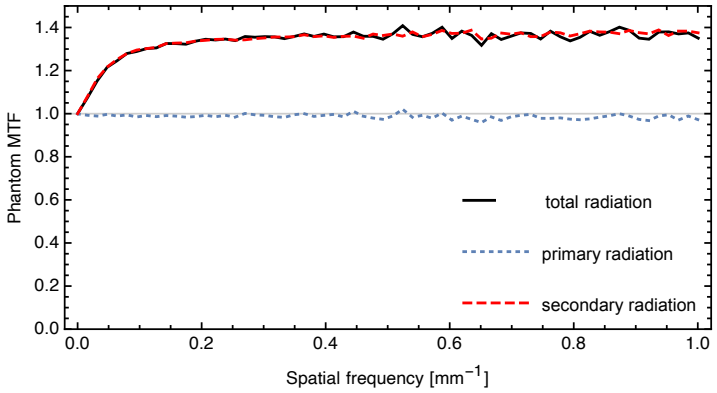

(a) Lead phantom, 1.3 cm thick.

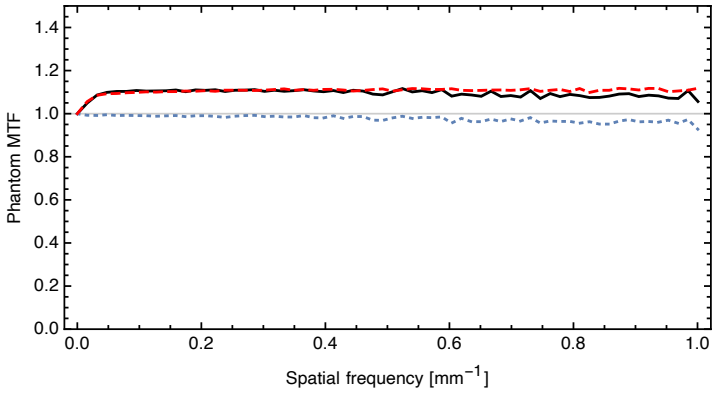

(b) Lead phantom, 3.3 cm thick.

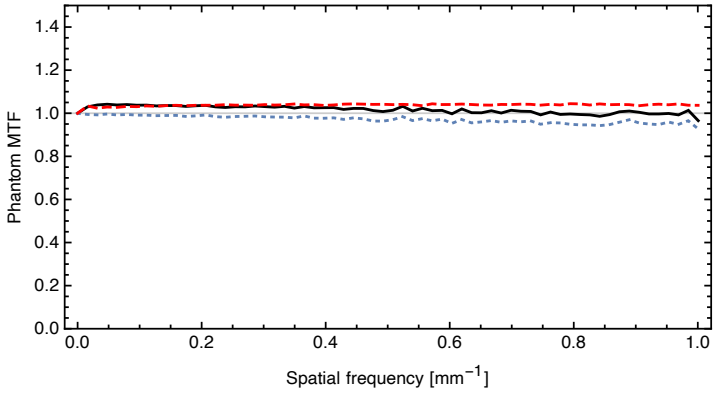

(c) Lead phantom, 5.0 cm thick.

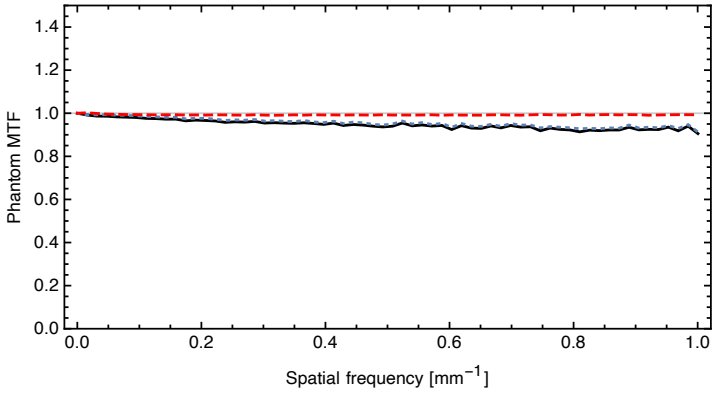

(d) Lead phantom, 10.0 cm thick.

Figure 4.19: Phantom MTFs of (a) 1.3 cm, (b) 3.3 cm, (c) 5.0 cm and (d) 10.0 cm thick lead edge phantoms at 6 MV beam quality in SID 180 cm. The total phantom MTF is composed of the components from primary and secondary radiation, showing the influence of geometric unsharpness and scatter, respectively. Compensation effects can favourably affect the systematic error over a limited spatial frequency range.

4.4 Improving measurement accuracy

The knowledge gained about geometric unsharpness and scatter at MV energies can be used to develop ideas for further improvement of the MTF measurement accuracy. Three approaches are discussed and quantified in this section: changes to the design of the phantom, changes to the measurement geometry and post-processing of measured data.

4.4.1 Changing the phantom design

In making changes to the phantom design, the goal is to find those particular conditions for which the detector input signal is closest to an ideal step function. So far, the presented simulations were limited to the four experimentally investigated lead phantoms. Additional simulations of different phantom designs were carried out, based on the newly found interdependencies between phantom design and phantom MTF.

Lead phantoms

The phantom which provided the highest accuracy so far was 5.0 cm thick lead. Simulations of slightly thicker and thinner phantoms were analyzed to gauge how sensitive the systematic error is with regard to phantom thickness.

	Phantom MTF 0.1 mm^{-1}	**Phantom MTF 0.5 mm^{-1}**	**Phantom MTF 1.0 mm^{-1}**
Lead, 4.0 cm	1.07	1.05	1.01
Lead, 4.5 cm	1.05	1.02	0.98
Lead, 5.0 cm	**1.04**	**1.01**	**0.97**
Lead, 5.5 cm	**1.02**	**0.99**	**0.96**
Lead, 6.0 cm	1.02	0.98	0.95

Table 4.2: Phantom MTF at selected spatial frequencies derived from Monte Carlo simulations of lead edge phantoms, assuming 6 MV beam quality and SID180 cm. The MTF values indicate the systematic measurement error introduced by the phantom design.

The phantom MTFs highlight that 5.0 cm was already the optimum thickness for a lead edge phantom (Table 4.2). Reducing the thickness to 4.5 cm inflates the systematic error to 5 % at low spatial frequencies of 0.1 mm^{-1} due to the higher amount of secondary radiation. For 4.0 cm, this value increases to 7 %. Meanwhile, a phantom thickness of 6.0 cm raises the error to a value of 5 % at 1 mm^{-1} due to geometric unsharpness. To keep the systematic error below 5 %, the thickness of the lead phantom should be between 5.0 cm and 5.5 cm.

Tungsten phantoms

Further improvement of the measurement accuracy would be possible with a phantom material that offers higher absorption compared to lead. At constant phantom thickness, a phantom with higher absorption produces a similar amount of geometric unsharpness, but less scatter. When the phantom thickness is reduced, the same level of scatter can be established, but the geometric unsharpness is reduced. Balancing these two options may reveal a scenario with an overall improved performance.

A material commonly used for situations that require high absorption of MV radiation is tungsten. For example, the collimating jaws as well as the leaves constituting the multi-leaf collimator in the treatment head of a medical linear accelerator are made from tungsten. A comparison of lead and tungsten at a selection of photon energies within the 6 MV spectrum shows similar values for the x-ray mass attenuation coefficient (Table 4.3). However, there is a significant change in the density which causes the total attenuation to be higher for a tungsten phantom compared to a lead phantom of the same thickness.

Once more, the greatest deviations occur for thin phantoms, in which the influence of secondary radiation is very strong. For thicker phantoms, the change is more gradual with a smaller difference between 10 cm and 20 cm phantom thickness than between 5 cm and 10 cm thickness. The simulation results show that it is possible to limit the measurement error further by switching the phantom material to tungsten. The higher density allows for a slightly thinner phantom which still induces less scattered radiation. The sweet spot is reached at a thickness of 4.0 cm, where the error is 3 % at maximum (Fig. 4.20). Slight variations of 0.5 cm thickness more or less than the optimum increase the error to 5 % or 4 %, respectively. Significant further improvement of the accuracy with a different edge phantom design seems unlikely, as it would require a higher beam attenuation without an increase in the phantom thickness. Platinum, osmium and iridium offer a slightly higher x-ray ab-

	Pb	**W**	**Pt**
Mass attenuation coefficient (cm^2/g)			
0.4 MeV	$2.32 \cdot 10^{-1}$	$1.93 \cdot 10^{-1}$	$2.12 \cdot 10^{-1}$
1.0 MeV	$7.10 \cdot 10^{-2}$	$6.62 \cdot 10^{-2}$	$6.86 \cdot 10^{-2}$
2.0 MeV	$4.61 \cdot 10^{-2}$	$4.43 \cdot 10^{-2}$	$4.52 \cdot 10^{-2}$
6.0 MeV	$4.39 \cdot 10^{-2}$	$4.21 \cdot 10^{-2}$	$4.31 \cdot 10^{-2}$
Density (g/cm^3)	11.4	19.3	21.5

Table 4.3: The total attenuation provided by a phantom is defined by the mass attenuation coefficient and the density. A tungsten phantom will provide higher attenuation than a lead phantom of similar thickness. This holds true for all photon energies within the 6 MV beam spectrum. Data according to NIST database. [102,93]

	Phantom MTF 0.1 mm^{-1}	Phantom MTF 0.5 mm^{-1}	Phantom MTF 1.0 mm^{-1}
Tungsten, 1.0 cm	1.28	1.36	1.34
Tungsten, 2.0 cm	1.14	1.13	1.12
Tungsten, 3.0 cm	1.06	1.05	1.02
Tungsten, 3.5 cm	1.04	1.02	0.98
Tungsten, 4.0 cm	**1.02**	**1.00**	**0.97**
Tungsten, 4.5 cm	1.00	0.98	0.95
Tungsten, 5.0 cm	1.00	0.97	0.93
Tungsten, 10.0 cm	0.98	0.94	0.90
Tungsten, 20.0 cm	0.97	0.92	0.88

Table 4.4: Phantom MTF at selected spatial frequencies derived from Monte Carlo simulations for several tungsten edge phantoms at 6 MV beam quality and SID 180 cm. The MTF values indicate the systematic measurement error introduced by the phantom design.

sorption than tungsten. However, the changes in mass attenuation coefficients and density were found to be too small to be relevant for MTF accuracy. Naturally, the above results are limited to the spatial frequency range of up to 1 mm^{-1}. Within this range, the 4.0 cm tungsten phantom offers the best compromise between MTF overestimation from scatter and MTF underestimation from geometric unsharpness (Fig. 4.20). If the performance of MV detectors were to improve to such an extent that MTF frequencies above 1 mm^{-1} became relevant, it would be necessary to extend this analysis. Within the scope of this work, the 4.0 cm tungsten phantom was found to provide the highest measurement accuracy of all phantom designs.

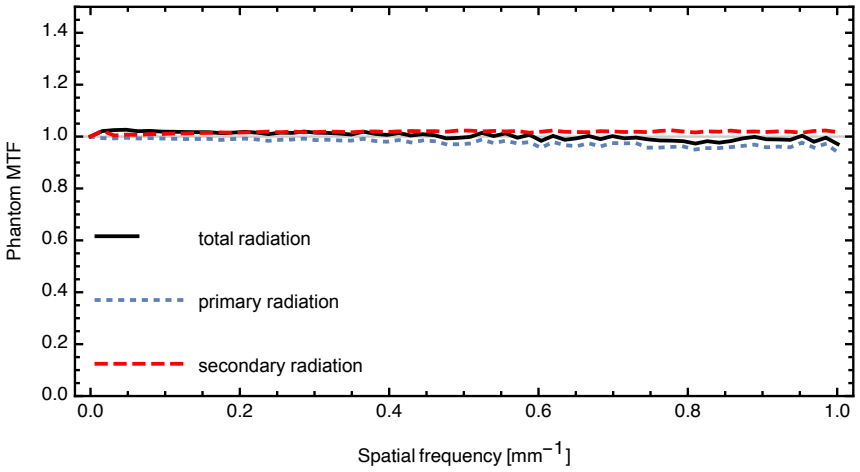

Figure 4.20: Phantom MTF of 4.0 cm tungsten edge phantom with components from primary and secondary radiation. In the frequency range up to 1 mm^{-1}, the systematic error from this phantom design is below 3 %.

4.4.2 Changing the measurement geometry

Apart from the design of the phantom, the measurement geometry can also have an effect on the measured MTF. As previously mentioned, measurements are usually conducted with the phantom in direct contact with the detector and the largest possible distance between the detector and the radiation source. The following section discusses to which degree the measurement geometry can be adjusted to improve the accuracy of an MTF measurement and whether the results obtained so far can be translated to a medical linear accelerator with different dimensions.

Using an air gap to reduce scatter

Most reports of MTF measurements at MV energies featured thick phantoms, in which the influence of scatter was limited by re-absorption of the secondary particles. In contrast, Star-Lack et al. reported positive results for a tantalum edge phantom of merely 0.5 mm thickness. The phantom was positioned 10 cm in front of the detector, deliberately creating an air gap between edge phantom and detector to reduce scatter.[64] If the technique is effective, it would allow the use of much thinner phantoms at MV energies, for example the same 1 mm tungsten edge which is used at kV energies.

The use of an air gap is a known radiographic technique which can be helpful in specific cases, e.g. pediatrics.[103] Its effect is similar to that of an anti-scatter grid, but it does not lead to an increased patient dose.[104] In theory, scattered radiation can be described as scatter point spread functions which emanate from every point on the phantom's exit surface (compare Section 2.5.4). The idea behind the air gap technique is to change the scatter distribution that reaches the detector by increasing the distance between the detector and the scatter point sources. This leads to a radial expansion of the scatter point spread functions as the photons are distributed more broadly following their angular distribution, so that strongly scattered photons will potentially leave the geometry without ever reaching the detector.[47]

The air gap technique is generally thought to be more effective at low energies, where most photons are scattered to the side rather than in forward direction.[105] Furthermore, elevating the phantom will undoubtedly introduce geometric unsharpness. The effect of an air gap was therefore investigated by simulating a 1.0 cm tungsten phantom at various distances from the detector. The air gap is defined as $d + t$, i.e. the distance between detector and phantom entrance plane.

In direct contact, the 1.0 cm tungsten phantom has demonstrated an MTF overestimation of about 35 % due to excessive scatter (compare Table 4.4). When the phantom is elevated, the formerly step-like profile of the scattered radiation is stretched out (Fig. 4.21). The scatter distribution in the central area around the edge transition is thereby somewhat homogenized. This means that the contribution of scatter to the detector input

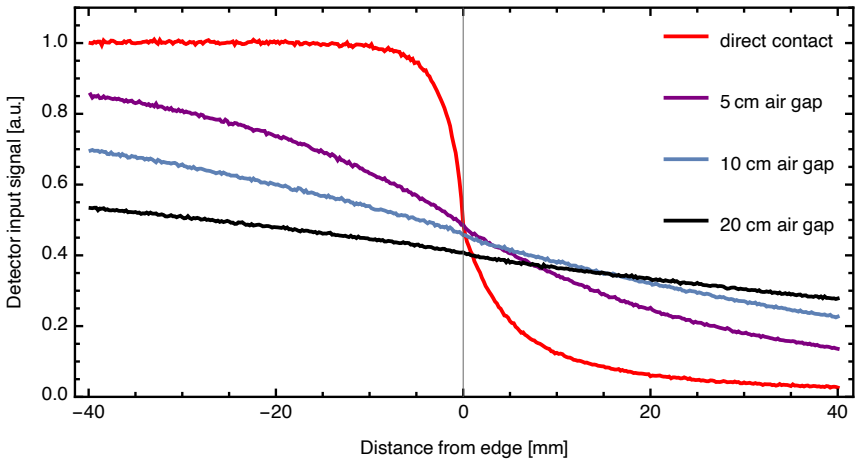

Figure 4.21: Monte Carlo simulated distribution of scattered radiation produced by a 1.0 cm thick tungsten edge phantom, positioned in direct contact with the detector or elevated to create a distance of 5 cm, 10 cm or 20 cm between the phantom entrance plane and the detector.

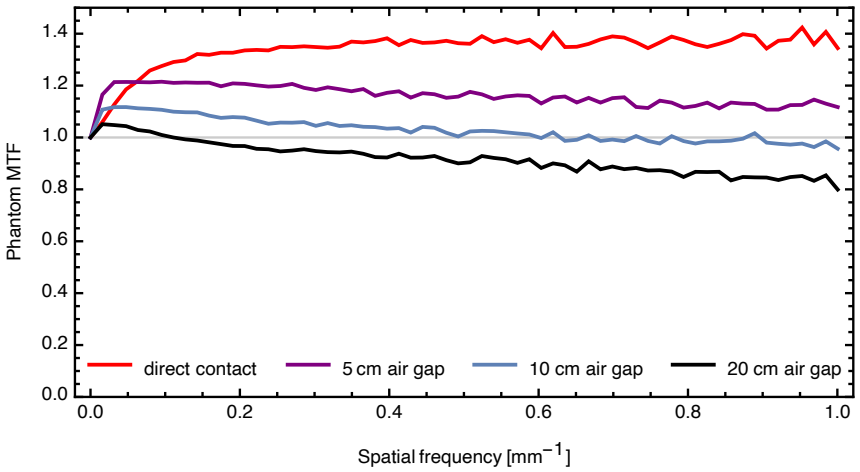

Figure 4.22: Phantom modulation transfer function indicating the systematic error introduced by an edge phantom of 1.0 cm tungsten, in direct contact with the detector or separated by an air gap of 5.0 cm, 10.0 cm or 20.0 cm from the detector.

signal is more similar to a linear transition or even a constant offset rather than a step-profile. The resulting improvement in MTF measurement accuracy is visible in the reduced overshoot of the phantom MTF (Fig. 4.22). On the other hand, the geometric unsharpness introduced by the air gap causes the measured MTF to decrease with spatial frequency.

Comparing the four geometries reveals that it is not possible to achieve an acceptable compromise between scatter and geometric unsharpness by adjusting the measurement geometry. The original publication by Star-Lack et al. contained results from Monte Carlo simulations which at first glance contradict these findings. However, a closer look at the analysis shows that the reported simulation suffered from similar shortcomings as already discussed above, namely incomplete modeling of the accelerator output. In this case, the radiation was approximated as a parallel beam, which, just like a point source, cannot simulate geometric unsharpness. Therefore, the introduction of an air gap appeared to be an effective technique.

The above results are in agreement with the previous investigation of geometric unsharpness (Section 4.3.1).

It had been shown that the systematic error due to geometric unsharpness is smaller for a phantom with thickness d in contact geometry, rather than a much thinner phantom at a distance d from the detector. This is mirrored here in the sub-par trend of the phantom MTFs over the spatial frequency range of interest. When given the choice, the use of a thick phantom in contact geometry is always the more favorable option in terms of MTF measurement accuracy.

Applicability to Elekta machines with SID 160 cm

Apart from the distance between phantom and detector, it is the source-to-imager distance (SID) which determines the geometry of an MTF measurement. A change of the SID does not affect the scatter distribution, but it will influence the amount of geometric unsharpness which is present in the detector input signal. Increasing the SID reduces the geometric unsharpness in the image, which is why it is advisable to perform MTF measurements at the greatest possible SID. In a clinical environment, however, the SID is limited by the travel range of the MV detector arm. The Monte Carlo simulations presented in this thesis are based on an SID of 180 cm, which is the greatest realizable SID for TrueBeam machines. The Elekta iViewGT system, another popular MV portal imager, has a fixed SID of 160 cm. Exemplary Monte Carlo simulations and measurements were performed to assess the applicability of the previously obtained results to Elekta machines.

According to the simulation, the 5.0 cm lead phantom is equally suitable for MTF measurements at SID 160 cm (Fig. 4.23a). The same was found for the 4.0 cm tungsten phantom. The deviations from the true MTF for these phantoms are below 5 % and below 3 %, respectively, just as in SID 180 cm geometry. For additional verification, the MTF measurement on the PortalVision aS1200 detector was repeated at SID 160 cm, using the 5 cm lead phantom. As predicted by the phantom MTF, the measurement results are in agreement (Fig. 4.23b). The RMS difference increases from 0.3 % at 0.1 mm^{-1} to merely 1.6 % at 1.0 mm^{-1}.

These findings do not imply that all data presented above is the same for SID 160 cm geometry. In particular, we can expect differences for very thick phantoms, in which the influence of geometric unsharpness is greatest. However, the phantoms that were identified to give the highest accuracy at SID 180 cm, namely 5.0 cm lead and 4.0 cm tungsten, will return equally accurate MTF measurement results at SID 160 cm.

4.4.3 Postprocessing by deconvolution

This work has sought and presented edge phantom designs that introduce the smallest possible systematic error on the MTF measurement. In the absence of a suitable phantom, it would be possible to use any other phantom design to compare several imaging systems to each other. While the absolute MTF values are corrupted and do not represent the true MTF, the *relative* relationship between MTFs measured *with the same phantom* is intact.

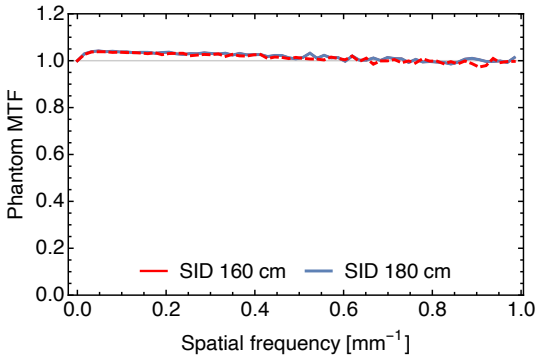

(a) Phantom MTFs of 5.0 cm lead edge phantom, obtained from Monte Carlo simulations.

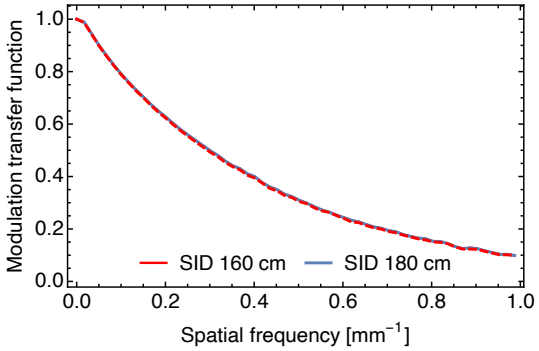

(b) Measurement of 5.0 cm lead edge phantom, performed with Varian PortalVision aS1200 detector.

Figure 4.23: Comparison of MTF measurement accuracy in SID 160 cm versus SID 180 cm geometry at 6 MV beam quality, exemplary for 5.0 cm lead edge phantom.

Sometimes it is still necessary to relate measurements which were acquired with different detectors and different phantoms. For example, one might want to compare measured data to previously published results which were acquired with a different phantom design.

Continuing the concept of the detector input signal established in Section 4.2 (see Eq. (4.4)), the phantom MTF relates the measured to the true detector MTF by a multiplication in the spatial frequency domain. When the phantom MTF is known, the operation could be reversed:

$$\mathrm{ESF}_{meas}(x) = \mathrm{DIS}(x) \star \mathrm{PSF}_{det}(x) \tag{4.7}$$

$$\mathrm{MTF}_{meas}(\xi) = \mathrm{MTF}_{phantom}(\xi) \cdot \mathrm{MTF}_{det}(\xi) \tag{4.8}$$

$$\mathrm{MTF}_{det}(\xi) = \frac{\mathrm{MTF}_{meas}(\xi)}{\mathrm{MTF}_{phantom}(\xi)} \tag{4.9}$$

Scatter as an additive component in the imaging process generally prevents a deconvolution (Eq. (4.3)). In this approach however, scatter is part of the detector input signal, which - as a whole - is convolved with the point spread function of the detector. It should therefore be possible to unify the measured MTFs by eliminating the respective systematic errors.

Each of the experimentally obtained MTFs was divided by its respective phantom MTF. Compared to the initial measurement (Fig. 4.6), deconvolution with the phantom MTF has reduced the differences between the measured MTFs and thereby potentially reduced the systematic error in the detector MTF. However, the correction has not been entirely effective. The MTF from 10.0 cm lead appears to underestimate the true MTF at high spatial frequencies. A second deviation is visible in the MTF from 1.3 cm lead at frequencies around 0.2 mm^{-1}. The MTFs from 3.3 cm and 5.0 cm lead, however, agree over the entire spatial frequency range. The

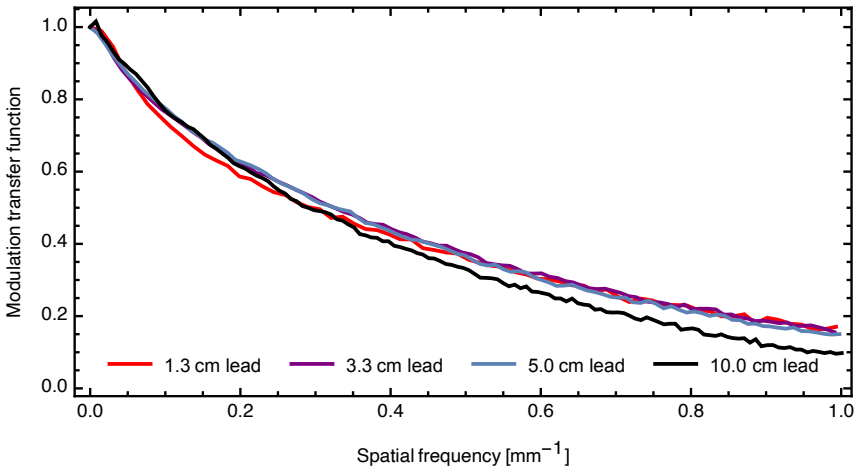

Figure 4.24: Detector MTF of the Varian PortalVision aS1200 detector, corrected for the systematic error introduced by the individual phantom designs.

discrepancies may stem from both measurement and simulation. It was assumed that the detector has equal sensitivity for scattered and primary incident radiation. This may not be true, as the detector is likely to exhibit some form of angular dependence. In this case, the effect would be most pronounced for the 1.3 cm phantom, for which the scatter fraction is highest. On the other hand, the accuracy of the phantom MTF depends on the faithful reproduction of the radiation source in the Monte Carlo simulation. As demonstrated before, the use of a point source leads to an entirely different result compared to the implementation of the complete accelerator head phase space. The TrueBeam phase space used for the simulations in this thesis was optimized to achieve dosimetric equivalence in water, for which the source size is only one of many fitting parameters. It is possible that the Monte Carlo simulations model the source size inadequately. As geometric unsharpness is very sensitive to the size of the radiation source, it is possible that this causes the deviation for the 10.0 cm lead phantom. So far, neither the detector sensitivity for scattered radiation, nor the source representation in phase space data has been investigated. The results seen here are therefore only proof of principle that the phantom MTF could be useful in correcting MTF measurements via deconvolution. As long as the results cannot be brought to sufficient agreement, it is sensible to measure the MTF with phantoms which are close to the optimum design, e.g. 5.0 cm lead or 4.0 cm tungsten.

5 Conclusion

This thesis investigated the accuracy of MTF measurements at MV energies conducted with edge phantoms. The experimental study showed that the measured MTF strongly depends on the design of the edge phantom. Insufficient absorption of the incident MV radiation causes the photon fluence behind the phantom to deviate from the ideal step-function shape. Consequently, the measured MTF is not the true MTF.

A novel method was developed which determines the MTF measurement accuracy based on Monte Carlo simulations of the detector input signal. The corresponding MTF, called the phantom MTF, reveals the systematic error by its deviation from unity. The results are applicable to all MV imaging devices used with a comparable beam quality, including EPIDs as well as 2D ion chamber arrays.

It was found that the detector input signal is impaired by geometric unsharpness and scatter, while the influence of absorption unsharpness is negligible. Geometric unsharpness is introduced to the measurement as the entrance plane of the phantom is elevated from the detector due to the phantom's thickness. It leads to an underestimation of the MTF, which increases with spatial frequency and phantom thickness. The interaction of the photon beam with the edge phantom produces scatter, part of which is re-absorbed before it reaches the detector. The presence of scatter leads to an overestimation of the MTF, which remains constant with spatial frequency.

These two factors must be balanced to achieve the highest overall measurement accuracy: Increasing the phantom thickness will prevent excessive scattering, while decreasing the thickness will reduce the geometric

unsharpness. For 6 MV beam quality, an SID of 180 cm and the usable frequency range up to 1 mm^{-1}, an edge phantom made from 5.0 cm thick lead will return the MTF with an accuracy of 5 %. Alternatively, the error can be kept within 3 % when using a 4.0 cm thick tungsten edge.

Other phantoms can be used for a relative comparison of different MV imaging systems. However, it must be noted that the measured values do not reflect the true MTF and cannot be compared to published results which were obtained with a different phantom. To some extent, the influence of a non-ideal phantom can be compensated by deconvolution of the measured MTF with the phantom MTF. However, this procedure requires a very good reconstruction of the radiation source within the Monte Carlo simulation, which might not be possible and is difficult to verify. If in doubt, it is always preferable to measure the MTF with an edge phantom that induces a small systematic error on the measurement.

Although this study was limited to 6 MV beam quality, the newly developed technique to quantify the systematic error using the phantom MTF is applicable to all systems for which the photon beam can be accurately modeled. Higher energies will presumably present an even greater challenge for MTF measurements, but are of secondary interest for imaging applications due to the low tissue contrast. Instead, some Varian machines offer a 2.5 MV beam for improved image quality and lower imaging dose. [106] As of yet, no data is available to model the 2.5 MV beam in Monte Carlo simulations, but it would be interesting to conduct a similar analysis at this beam quality.

The modulation transfer function stands alongside other metrics which quantify the performance of an imaging system, such as the noise power spectrum and the detective quantum efficiency. While this work has contributed to the technical side of MTF measurement, it is embedded in a greater question: As stated in a key publication by Kurt Rossmann, who left the Kodak Laboratories in 1967 to join the Department of Radiology at the University of Chicago, the central problem of radiographic image quality is the relationship between the physical and the diagnostic image quality. [107] Diagnostic accuracy, the ultimate goal of a radiologic examination, requires not necessarily the most faithful reproduction of the object, but the transfer of diagnostically important information, which can be different depending on the objects or lesions of clinical interest. The radiological process does not end with the displaying of an image. It includes the eye, as well as the brain of the radiologist. [108] The observer performance and surrounding anatomic structures influence the diagnostic task along with the physical image quality. The ICRU report 41 [109], published in 1986, is still relevant today when it states that the relationships between diagnostic accuracy and these factors are “complex and not well understood at present”.

References

[1] S. Mukherjee, *The Emperor of All Maladies*. A Biography of Cancer, Simon and Schuster, Inc., 2011.

[2] W. H. McBride, H. R. Withers, and D. Schaue, "Biologic Basis of Radiation Therapy," in *Perez and Brady's Principles and Practice of Radiation Oncology* (E. C. Halperin, D. E. Wazer, C. A. Perez, and L. W. Brady, eds.), pp. 87–111, Wolters Kluwer, Sept. 2018.

[3] M. Goitein, "Radiation in the Treatment of Cancer ," in *Radiation Oncology: A Physicist's-Eye View*, pp. 1–11, Springer New York, 2007.

[4] M. Lederman, "The early history of radiotherapy: 1895–1939," *International Journal of Radiation Oncology*Biology*Physics*, vol. 7, no. 5, pp. 639–648, 1981.

[5] W. Schlegel, "New Technologies in 3D Conformal Radiation Therapy: Introduction and Overview," in *New Technologies in Radiation Oncology* (W. Schlegel, T. Bortfeld, and A.-L. Grosu, eds.), pp. 1–6, Springer Berlin Heidelberg, 2006.

[6] Y. Zhang and J. Wang, "Kilovoltage and Megavoltage Imaging in Radiotherapy," in *Handbook of X-ray Imaging* (P. Russo, ed.), pp. 897–916, CRC Press, 2018.

[7] Y. El-Mohri, J. Yorkston, K. W. Jee, M. Maolinbay, K. L. Lam, and J. H. Siewerdsen, "Relative dosimetry using active matrix flat-panel imager (AMFPI) technology," *Medical Physics*, vol. 26, pp. 1530–1541, Aug. 1999.

[8] E. Peli, "Contrast in complex images," *Journal of the Optical Society of America*, vol. 7, pp. 2032–2040, Oct. 1990.

[9] J. C. Dainty and R. Shaw, "Fourier Transforms, and the Analysis of Image Resolution and Noise," in *Image science: principles, analysis and evaluation of photographic type imaging processes*, pp. 190–231, Academic Press, 1974.

[10] W. H. Press, "Fast Fourier Transform," in *Numerical Recipes*, pp. 600–639, Cambridge University Press, Sept. 2007.

[11] K. Rossmann, "Point spread-function, line spread-function, and modulation transfer function: tools for the study of imaging systems," *Radiology*, vol. 93, pp. 257–272, Aug. 1969.

[12] I. A. Cunningham, "Applied Linear-Systems Theory," in *Handbook of Medical Imaging: Physics and psychophysics* (J. Beutel, H. L. Kundel, and R. L. Van Metter, eds.), pp. 79–160, SPIE Press, Jan. 2000.

[13] M. L. Giger and K. Doi, "Investigation of basic imaging properties in digital radiography. I. Modulation transfer function," *Medical Physics*, vol. 11, pp. 287–295, May 1984.

[14] G. D. Boreman, "MTF in Optical Systems," in *Modulation Transfer Function in Optical and Electro-optical Systems*, pp. 1–30, SPIE Press, 2001.

[15] E. C. Yeadon, R. A. Jones, and J. T. Kelly, "Confidence Limits for Individual Modulation Transfer Function Measurements Based upon the Phase Transfer Function," *Photographic Science and Engineering*, vol. 14, no. 2, pp. 153–156, 1970.

[16] IEC 62220-1:2003, "Medical electrical equipment - Characteristics of digital X-ray imaging devices - Part 1: Determination of the detective quantum efficiency," 2003.

[17] E. W. H. Selwyn, "The photographic and visual resolving power of lenses. Part I. Visual Resolving Power.," *The Photographic Journal*, vol. 88B, pp. 6–12, 1948.

[18] O. H. Schade, "Electro-optical specifications for television systems," *RCA Review*, vol. 9, pp. 246–286, June 1948.

[19] J. W. Coltman, "The Specification of Imaging Properties by Response to a Sine Wave Input," *Journal of the Optical Society of America*, vol. 44, no. 6, pp. 468–471, 1954.

[20] K. Rossmann, "Measurement of the Modulation Transfer Function of Radiographic Systems Containing Fluorescent Screens," *Physics in Medicine and Biology*, vol. 9, no. 4, pp. 551–557, 1964.

[21] R. T. Droege and R. L. Morin, "A practical method to measure the MTF of CT scanners," *Medical Physics*, vol. 9, pp. 758–760, Sept. 1982.

[22] A. Gopal and S. S. Samant, "Use of a line-pair resolution phantom for comprehensive quality assurance of electronic portal imaging devices based on fundamental imaging metrics," *Medical Physics*, vol. 36, pp. 2006–2015, June 2009.

[23] A. Gopal and S. S. Samant, "Validity of the line-pair bar-pattern method in the measurement of the modulation transfer function (MTF) in megavoltage imaging," *Medical Physics*, vol. 35, pp. 270–279, Jan. 2008.

[24] K. Rossmann, "Modulation Transfer Function of Radiographic Systems Using Fluorescent Screens," *Journal of the Optical Society of America*, vol. 52, pp. 774–777, July 1962.

[25] K. Doi, "Kurt Rossmann, Ph.D. (1926–1976): pioneer in image quality evaluation and radiologic imaging research," *Radiological Physics and Technology*, vol. 6, pp. 1–6, Nov. 2012.

[26] K. Rossmann, "Image-forming quality of radiographic screen-film systems: the line spread-function.," *The American journal of roentgenology, radium therapy, and nuclear medicine*, vol. 90, pp. 178–183, July 1963.

[27] G. D. Boreman, "MTF Measurement Methods," in *Modulation Transfer Function in Optical and Electro-optical Systems*, pp. 69–84, SPIE Press, 2001.

[28] I. A. Cunningham and A. Fenster, "A method for modulation transfer function determination from edge profiles with correction for finite-element differentiation," *Medical Physics*, vol. 14, pp. 533–537, July 1987.

[29] E. Buhr, S. Günther-Kohfahl, and U. Neitzel, "Accuracy of a simple method for deriving the presampled modulation transfer function of a digital radiographic system from an edge image," *Medical Physics*, vol. 30, pp. 2323–2331, Aug. 2003.

[30] E. Samei, N. T. Ranger, J. T. Dobbins III, and Y. Chen, "Intercomparison of methods for image quality characterization. I. Modulation transfer function," *Medical Physics*, vol. 33, pp. 1466–13, Apr. 2006.

[31] R. T. Droege and B. E. Bjärngard, "Metal screen-film detector MTF at megavoltage x-ray energies," *Medical Physics*, vol. 6, no. 6, pp. 515–518, 1979.

[32] R. T. Droege, "A megavoltage MTF measurement technique for metal screen-film detectors," *Medical Physics*, vol. 6, no. 4, pp. 272–279, 1979.

[33] A. Sawant, Y. El-Mohri, and L. E. Antonuk, "Slit design for efficient and accurate MTF measurement at megavoltage x-ray energies," *Medical Physics*, vol. 34, pp. 1535–1545, May 2007.

[34] K. Doi, K. Strubler, and K. Rossmann, "Truncation errors in calculating the MTF of radiographic screen-film systems from the line spread function," *Physics in Medicine and Biology*, vol. 17, no. 2, pp. 241–250, 1972.

[35] S. N. Friedman and I. A. Cunningham, "Normalization of the modulation transfer function: The open-field approach," *Medical Physics*, vol. 35, pp. 4443–4449, Oct. 2008.

[36] I. A. Cunningham and B. K. Reid, "Signal and noise in modulation transfer function determinations using the slit, wire, and edge techniques," *Medical Physics*, vol. 19, pp. 1037–1044, July 1992.

[37] M. G. Herman, J. M. Balter, D. A. Jaffray, K. P. McGee, P. Munro, S. Shalev, M. Van Herk, and J. W. Wong, "Clinical use of electronic portal imaging: Report of AAPM Radiation Therapy Committee Task Group 58," *Medical Physics*, vol. 28, pp. 712–737, May 2001.

[38] G. D. Boreman, "MTF in Electro-Optical Systems," in *Modulation Transfer Function in Optical and Electro-optical Systems*, pp. 31–58, SPIE Press, 2001.

[39] G. Lubberts and K. Rossmann, "Modulation Transfer Function Associated with Geometrical Unsharpness in Medical Radiography," *Physics in Medicine and Biology*, vol. 12, no. 1, pp. 65–77, 1967.

[40] T. S. Curry, J. E. Dowdey, and R. C. Murry, "Geometry of the Radiographic Image," in *Christensen's Physics of Diagnostic Radiology*, pp. 219–241, Lippincott Williams & Wilkins, 1990.

[41] M. Sure, W. W. Baus, A. Hellerbach, M. Hoevels, and H. Treuer, "Determination of focal spot size for linear accelerators: comparison of experiment and simulation ," in *Biomedical Engineering / Biomedizinische Technik*, pp. 1–5, Aug. 2017.

[42] W. R. Hendee and E. R. Ritenour, "Influences on Image Quality," in *Medical Imaging Physics*, pp. 265–280, John Wiley and Sons, Apr. 2003.

[43] K. Rossmann and H. E. Seemann, "Detail visibility in radiographs: theoretical study of the effect of x-ray absorption in the object on the edge sharpness of radiographic images.," *The American journal of roentgenology, radium therapy, and nuclear medicine*, vol. 85, pp. 366–371, Feb. 1961.

[44] K. Rossmann, "Detail visibility in radiographs: an experimental and theoretical study of geometric and absorption unsharpness.," *The American journal of roentgenology, radium therapy, and nuclear medicine*, vol. 87, pp. 387–393, Feb. 1962.

[45] P. Munro and D. C. Bouius, "X-ray quantum limited portal imaging using amorphous silicon flat-panel arrays," *Medical Physics*, vol. 25, pp. 689–702, May 1998.

[46] G. Hajdok, J. J. Battista, and I. A. Cunningham, "Fundamental x-ray interaction limits in diagnostic imaging detectors: Spatial resolution," *Medical Physics*, vol. 35, pp. 3180–3193, June 2008.

[47] U. Neitzel, E. Buhr, G. Hilgers, and P. R. Granfors, "Determination of the modulation transfer function using the edge method: Influence of scattered radiation," *Medical Physics*, vol. 31, pp. 3485–3491, Nov. 2004.

[48] J. M. Boone and J. A. Seibert, "An analytical model of the scattered radiation distribution in diagnostic radiology," *Medical Physics*, vol. 15, no. 5, pp. 721–725, 1988.

[49] J. M. Boone and J. A. Seibert, "Monte Carlo simulation of the scattered radiation distribution in diagnostic radiology," *Medical Physics*, vol. 15, no. 5, pp. 713–720, 1988.

[50] K. Rossmann, "Detail visibility in radiographs: an experimental and theoretical study of geometric and absorption unsharpness.," *The American journal of roentgenology, radium therapy, and nuclear medicine*, vol. 87, pp. 387–393, Feb. 1962.

[51] K. Rossmann, G. Lubberts, and H. M. Cleare, "Measurement of the Line Spread-Function of Radiographic Systems Containing Fluorescent Screens," *Journal of the Optical Society of America*, vol. 54, pp. 187–190, Feb. 1964.

[52] R. T. Droege and B. E. Bjärngard, "Influence of metal screens on contrast in megavoltage x-ray imaging," *Medical Physics*, vol. 6, no. 6, pp. 487–493, 1979.

[53] P. Munro, J. A. Rawlinson, and A. Fenster, "Therapy imaging: A signal-to-noise analysis of metal plate/film detectors," *Medical Physics*, vol. 14, pp. 975–984, Nov. 1987.

[54] P. Munro, J. A. Rawlinson, and A. Fenster, "Therapy imaging: A signal-to-noise analysis of a fluoroscopic imaging system for radiotherapy localization," *Medical Physics*, vol. 17, pp. 763–772, Sept. 1990.

[55] J.-P. Bissonnette, D. A. Jaffray, A. Fenster, and P. Munro, "Optimal radiographic magnification for portal imaging," *Medical Physics*, vol. 21, pp. 1435–1445, Sept. 1994.

[56] T. Falco and B. G. Fallone, "Characteristics of metal-plate/film detectors at therapy energies. I. Modulation transfer function," *Medical Physics*, vol. 25, pp. 2455–2462, Dec. 1998.

[57] Y. El-Mohri, K.-W. Jee, L. E. Antonuk, M. Maolinbay, and Q. Zhao, "Determination of the detective quantum efficiency of a prototype, megavoltage indirect detection, active matrix flat-panel imager," *Medical Physics*, vol. 28, pp. 2538–2550, Dec. 2001.

[58] F. Cremers, T. Frenzel, C. Kausch, D. Albers, T. Schönborn, and R. Schmidt, "Performance of electronic portal imaging devices (EPIDs) used in radiotherapy: Image quality and dose measurements," *Medical Physics*, vol. 31, pp. 985–996, May 2004.

[59] A. Sawant, L. E. Antonuk, Y. El-Mohri, Q. Zhao, Y. Wang, Y. Li, H. Du, and L. Perna, "Segmented crystalline scintillators: Empirical and theoretical investigation of a high quantum efficiency EPID based on an initial engineering prototype CsI(Tl) detector," *Medical Physics*, vol. 33, pp. 1053–1066, Apr. 2006.

[60] S. S. Samant and A. Gopal, "Analysis of the kinestatic charge detection system as a high detective quantum efficiency electronic portal imaging device," *Medical Physics*, vol. 33, pp. 3557–3567, Sept. 2006.

[61] S. S. Samant and A. Gopal, "Study of a prototype high quantum efficiency thick scintillation crystal video-electronic portal imaging device," *Medical Physics*, vol. 33, pp. 2783–2791, Aug. 2006.

[62] J. Rottmann, D. Morf, R. Fueglistaller, G. Zentai, J. Star-Lack, and R. Berbeco, "A novel EPID design for enhanced contrast and detective quantum efficiency," *Physics in Medicine and Biology*, vol. 61, pp. 6297–6306, Aug. 2016.

[63] J. R. D. Earnhart and E. L. Chaney, "Modulation transfer function for a large-area amorphous silicon image receptor," *Physics in Medicine and Biology*, vol. 42, pp. 2531–2540, July 1997.

[64] J. Star-Lack, D. Shedlock, D. Swahn, D. Humber, A. Wang, H. Hirsh, G. Zentai, D. Sawkey, I. Kruger, M. Sun, E. Abel, G. Virshup, M. Shin, and R. Fahrig, "A piecewise-focused high DQE detector for MV imaging," *Medical Physics*, vol. 42, pp. 5084–5099, Aug. 2015.

[65] J.-W. Min, K.-W. Kim, Y.-H. Seoung, J.-M. Kim, I.-S. Choi, H.-W. Jeong, S.-Y. Son, S.-Y. Kim, D.-W. Lee, and B.-Y. Choe, "Performance of an edge block used in a configuration detector: Image quality measurements," *Journal of the Korean Physical Society*, vol. 64, pp. 732–739, Mar. 2014.

[66] J.-W. Min, K.-W. Kim, J.-M. Kim, I.-S. Choi, H.-W. Jeong, S.-Y. Son, G.-M. Back, J.-H. Jung, J.-Y. Jung, and B.-Y. Choe, "Evaluation of the modulation transfer function of megavoltage X-rays," *Journal of the Korean Physical Society*, vol. 65, pp. 1969–1975, Dec. 2014.

[67] S.-Y. Son, B.-Y. Choe, J.-W. Lee, J.-M. Kim, H.-W. Jeong, H.-G. Kim, W.-S. Kim, K.-Y. Lyu, J.-W. Min, and K.-W. Kim, "Evaluation of an edge method for computed radiography and an electronic portal imaging device in radiotherapy: Image quality measurements," *Journal of the Korean Physical Society*, vol. 65, pp. 1976–1984, Dec. 2014.

[68] Y.-H. Hu, J. Rottmann, R. Fueglistaller, M. Myronakis, A. Wang, P. Huber, D. Shedlock, D. Morf, P. Baturin, J. Star-Lack, and R. Berbeco, "Leveraging multi-layer imager detector design to improve low-dose performance for megavoltage cone-beam computed tomography," *Physics in Medicine and Biology*, vol. 63, p. 035022, Feb. 2018.

[69] Y.-H. Hu, D. Shedlock, A. Wang, J. Rottmann, P. Baturin, M. Myronakis, P. Huber, R. Fueglistaller, M. Shi, D. Morf, J. S. Lack, and R. I. Berbeco, "Characterizing a novel scintillating glass for application to megavoltage cone-beam computed tomography," *Medical Physics*, vol. 46, pp. 1323–1330, Mar. 2019.

[70] A. Sawant, L. E. Antonuk, Y. El-Mohri, Y. Li, Z. Su, Y. Wang, J. Yamamoto, Q. Zhao, H. Du, J. Daniel, and R. Street, "Segmented phosphors: MEMS-based high quantum efficiency detectors for megavoltage x-ray imaging," *Medical Physics*, vol. 32, pp. 553–565, Feb. 2005.

[71] H. Fujita, D. Y. Tsai, T. Itoh, K. Doi, J. Morishita, K. Ueda, and A. Ohtsuka, "A simple method for determining the modulation transfer function in digital radiography," *IEEE Transactions on Medical Imaging*, vol. 11, pp. 34–39, Mar. 1992.

[72] Varian Medical Systems, "TrueBeam System: Specifications," tech. rep., Aug. 2013.

[73] B. M. C. McCurdy, K. Luchka, and S. Pistorius, "Dosimetric investigation and portal dose image prediction using an amorphous silicon electronic portal imaging device," *Medical Physics*, vol. 28, pp. 911–924, June 2001.

[74] I. Kawrakow, E. Mainegra-Hing, D. W. O. Rogers, F. Tessier, and B. R. B. Walters, "The EGSnrc Code System: Monte Carlo simulation of electron and photon transport," Tech. Rep. PIRS-701, National Research Council Canada, 2017.

[75] M. H. Kalos and P. A. Whitlock, "A Bit of Probability," in *Monte Carlo Methods*, pp. 7–34, Wiley, 2008.

[76] B. R. B. Walters, I. Kawrakow, and D. W. O. Rogers, "History by history statistical estimators in the BEAMcode system," *Medical Physics*, vol. 29, pp. 2745–2752, Dec. 2002.

[77] J. Sempau, A. Sánchez-Reyes, F. Salvat, H. O. ben Tahar, S. B. Jiang, and J. M. Fernández-Varea, "Monte Carlo simulation of electron beams from an accelerator head using PENELOPE," *Physics in Medicine and Biology*, vol. 46, pp. 1163–1186, Apr. 2001.

[78] M. J. Berger, "Monte Carlo calculation of the penetration and diffusion of fast charged particles," in *Methods in Computational Physics, Vol.* (B. Alder, S. Fernbach, and M. Rotenberg, eds.), pp. 135–215, 1963.

[79] D. W. O. Rogers, "Fifty years of Monte Carlo simulations for medical physics," *Physics in Medicine and Biology*, vol. 51, pp. R287–R301, June 2006.

[80] U. Fano, "Note on the Bragg-Gray Cavity Principle for Measuring Energy Dissipation," *Radiation Research*, vol. 1, p. 237, June 1954.

[81] I. Kawrakow, "Accurate condensed history Monte Carlo simulation of electron transport. I. EGSnrc, the new EGS4version," *Medical Physics*, vol. 27, pp. 485–498, Mar. 2000.

[82] I. Kawrakow, "Accurate condensed history Monte Carlo simulation of electron transport. II. Application to ion chamber response simulations," *Medical Physics*, vol. 27, pp. 499–513, Mar. 2000.

[83] D. W. O. Rogers and C. M. Ma, "BEAM: A Monte Carlo code to simulate radiotherapy treatment units," *Medical Physics*, vol. 22, pp. 503–524, May 1995.

[84] D. W. O. Rogers, B. R. B. Walters, and I. Kawrakow, "BEAMnrc Users Manual," Tech. Rep. PIRS-0509(A), National Research Council Canada, Feb. 2017.

[85] Varian Medical Systems, "TrueBeam Monte Carlo Data Package," Tech. Rep. Confidential Information, Varian Medical Systems, Mar. 2014.

[86] A. Rodrigues, D. Sawkey, F.-F. Yin, and Q. Wu, "A Monte Carlo simulation framework for electron beam dose calculations using Varian phase space files for TrueBeam Linacs," *Medical Physics*, vol. 42, pp. 2389–2403, Apr. 2015.

[87] S. Ali, A. Q. Jandga, and A. Hussain, "Evaluation of Golden Beam Data for the Commissioning of 6 and 18 MV Photons Beams in Varian Linear Accelerator," *International Journal of Biomedical and Biological Engineering*, vol. 9, Jan. 2015.

[88] B. R. B. Walters, I. Kawrakow, and D. W. O. Rogers, "DOSXYZnrc Users Manual," Tech. Rep. PIRS-794, National Research Council Canada, Feb. 2017.

[89] H. C. E. McGowan, B. A. Faddegon, and C. M. Ma, "STATDOSE for 3D dose distributions ," Tech. Rep. PIRS-0509(F), National Research Council Canada, Jan. 2020.

[90] C. M. Ma, J. S. Li, T. Pawlicki, S. B. Jiang, J. Deng, M. C. Lee, T. Koumrian, M. Luxton, and S. Brain, "A Monte Carlo dose calculation tool for radiotherapy treatment planning," *Physics in Medicine and Biology*, vol. 47, pp. 1671–1689, May 2002.

[91] I. A. Popescu, C. P. Shaw, S. F. Zavgorodni, and W. A. Beckham, "Absolute dose calculations for Monte Carlo simulations of radiotherapy beams," *Physics in Medicine and Biology*, vol. 50, pp. 3375–3392, July 2005.

[92] Varian Medical Systems, "TrueBeam/ TrueBeam STx STB-II-536 DMI Upgrade," Tech. Rep. IPA-HT-STBII536-A, Varian Medical Systems, Mar. 2015.

[93] M. J. Berger, J. S. Coursey, M. A. Zucker, and J. Chang, "ESTAR, PSTAR, and ASTAR: Computer Programs for Calculating Stopping-Power and Range Tables for Electrons, Protons, and Helium Ions," `http://physics.nist.gov/Star` *(accessed December 5, 2017)*.

[94] Wolfram Research, Inc., *Mathematica*. Champaign, Illinois, 12.0 ed., 2019.

[95] U. Neitzel, S. Günther-Kohfahl, G. Borasi, and E. Samei, "Determination of the detective quantum efficiency of a digital x-ray detector: Comparison of three evaluations using a common image data set," *Medical Physics*, vol. 31, pp. 2205–2211, July 2004.

[96] A.-K. Carton, D. Vandenbroucke, L. Struye, A. D. A. Maidment, Y.-H. Kao, M. Albert, H. Bosmans, and G. Marchal, "Validation of MTF measurement for digital mammography quality control.," *Medical Physics*, vol. 32, pp. 1684–1695, June 2005.

[97] J. H. Siewerdsen, L. E. Antonuk, Y. El-Mohri, J. Yorkston, W. Huang, J. M. Boudry, and I. A. Cunningham, "Empirical and theoretical investigation of the noise performance of indirect detection, active matrix flat-panel imagers (AMFPIs) for diagnostic radiology," *Medical Physics*, vol. 24, pp. 71–89, Jan. 1997.

[98] E. S. Blackman, "Effects of Noise on the Determination of Photographic System Modulation Transfer Functions," *Photographic Science and Engineering*, vol. 12, no. 5, pp. 244–250, 1968.

[99] A. González-López, "Effect of noise on MTF calculations using different phantoms," *Medical Physics*, vol. 45, pp. 1889–1898, Mar. 2018.

[100] H. Illers, "Measurement of the modulation transfer function of digital X-ray detectors with an opaque edge-test device," *Radiation Protection Dosimetry*, vol. 114, pp. 214–219, May 2005.

[101] J. C. Le Heron and J. L. Poletti, "Measurement of x-ray image intensifier sharpness in the x-ray department.," *Physics in Medicine and Biology*, vol. 33, pp. 93–104, Jan. 1988.

[102] M. J. Berger, J. H. Hubbell, S. M. Seltzer, J. Chang, J. S. Coursey, R. Sukumar, D. S. Zucker, and K. Olsen, "XCOM: Photon Cross Section Database," `http://physics.nist.gov/xcom` *(accessed December 5, 2017)*.

[103] U. Neitzel, "Grids or air gaps for scatter reduction in digital radiography: A model calculation," *Medical Physics*, vol. 19, pp. 475–481, Mar. 1992.

[104] H. Aichinger, J. Dierker, S. Joite-Barfuß, and M. Säbel, "Scattered Radiation," in *Radiation Exposure and Image Quality in X-Ray Diagnostic Radiology*, pp. 45–56, Springer Science & Business Media, 2004.

[105] S. C. Bushong, "Scatter Radiation," in *Radiologic Science for Technologists*, pp. 186–206, Elsevier, 2016.

[106] G. X. Ding and P. Munro, "Characteristics of 2.5 MV beam and imaging dose to patients," *Radiotherapy and Oncology*, vol. 125, pp. 541–547, Dec. 2017.

[107] K. Rossmann and B. E. Wiley, "The Central Problem in the Study of Radiographic Image Quality," *Radiology*, vol. 96, pp. 113–118, July 1970.

[108] K. Rossmann, "The spatial frequency spectrum: a means for studying the quality of radiographic imaging systems," *Radiology*, vol. 90, pp. 1–13, Jan. 1968.

[109] K. Doi, P. C. Bunch, G. Holje, M. Pfeiler, and R. F. Wagner, "Report 41: Modulation Transfer Function of Screen-Film Systems," *Journal of the International Commission on Radiation Units and Measurements*, Aug. 1986.

[110] B. R. B. Walters and I. Kawrakow, "Technical note: Overprediction of dose with default PRESTA-I boundary crossing in DOSXYZnrc and BEAMnrc," *Medical Physics*, vol. 34, pp. 647–650, Jan. 2007.

[111] D. W. O. Rogers, "Low energy electron transport with EGS," *Nuclear Instruments and Methods in Physics Research*, vol. 227, no. 3, pp. 535–548, 1984.

[112] A. F. Bielajew and D. W. O. Rogers, "Electron Step-Size Artefacts and PRESTA," in *Monte Carlo Transport of Electrons and Photons* (T. M. Jenkins, W. R. Nelson, and A. Rindi, eds.), pp. 115–137, Springer US, 1988.

[113] A. F. Bielajew, C.-S. Chui, and R. Mohan, "Improved Bremsstrahlung Photon Angular Sampling in the EGS4 Code System," Tech. Rep. Report PIRS-0203, National Research Council of Canada, 1989.

[114] H. W. Koch and J. W. Motz, "Bremsstrahlung Cross-Section Formulas and Related Data," *Reviews of Modern Physics*, vol. 31, pp. 920–955, Oct. 1959.

[115] S. M. Seltzer and M. J. Berger, "Bremsstrahlung spectra from electron interactions with screened atomic nuclei and orbital electrons," *Nuclear Instruments and Methods in Physics Research*, vol. 12, pp. 95–134, Aug. 1985.

[116] S. M. Seltzer and M. J. Berger, "Bremsstrahlung energy spectra from electrons with kinetic energy 1 keV–10 GeV incident on screened nuclei and orbital electrons of neutral atoms with Z = 1–100," *Atomic Data and Nuclear Data Tables*, vol. 35, no. 3, pp. 345–418, 1986.

[117] M. J. Berger, M. Inokuti, H. H. Anderson, H. Bichsel, J. A. Dennis, D. Powers, S. M. Seltzer, and J. E. Turner, "Report 37: Stopping Powers for Electrons and Positrons," *Journal of the International Commission on Radiation Units and Measurements*, Dec. 1984.

[118] O. Klein and Y. Nishina, "Über die Streuung von Strahlung durch freie Elektronen nach der neuen relativistischen Quantendynamik von Dirac," *Zeitschrift für Physik*, vol. 52, pp. 853–868, Oct. 1928.

[119] R. Ribberfors, "Relationship of the relativistic Compton cross section to the momentum distribution of bound electron states," *Physical Review B*, vol. 12, pp. 2067–2074, Sept. 1975.

[120] J. W. Motz, H. A. Olsen, and H. W. Koch, "Pair Production by Photons," *Reviews of Modern Physics*, vol. 41, pp. 581–639, Oct. 1969.

[121] L. Storm and H. I. Israel, "Photon cross sections from 1 keV to 100 MeV for elements Z=1 to Z=100," *Atomic Data and Nuclear Data Tables*, vol. 7, pp. 565–681, June 1970.

[122] F. Sauter, "Über den atomaren Photoeffekt in der K-Schale nach der relativistischen Wellenmechanik Diracs," *Annalen der Physik*, vol. 403, pp. 454–488, Jan. 1931.

[123] D. E. Cullen, S. T. Perkins, and J. A. Rathkopf, "The 1989 Livermore Evaluated Photon Data Library (EPDL)," Tech. Rep. UCRL-ID-103424, Lawrence Livermore National Lab., CA (USA), Mar. 1990.

A Appendix

A.1 Monte Carlo Code

A.1.1 BEAMnrc sample input file

This is an exemplary input file for BEAMnrc, describing a 5 cm thick tungsten phantom in contact geometry being irradiated by a 6 MV photon beam (implemented via phase space file). The scoring plane (=image plane) is situated at SID 180 cm.

```
Tungsten edge phantom, t= 50 mm, SID 1.8m
AIR521ICRU
0, 0, 0, 0, 0, 3, 1, IWATCH ETC.
2553335660, 33, 97, 50, 0, 0, 0, 0, NCASE ETC.
0, 21, 1, 0, 0, 0, 0, 0, 0, 0, IQIN, ISOURCE + OPTIONS
/Users/.../EGSnrc/Varian-PHSP/TrueBeam-v2-6X.1.IAEAphsp
0, 0, 0.521, 0.01, 0, 1, 1, 0 , ECUT,PCUT,IREJCT,ESAVE
0, 0, 0, 0, 0, PHOTON FORCING
1, 2, SCORING INPUT
1, 1
```

```
400,
0, DOSE COMPONENTS
0.0, Z TO FRONT FACE
### start of CM SLABS with identifier SOURCE ###
30, RMAX
Source slab
1, NSLABS
0, ZMIN
44.41, 0.521, 0.01, 0, 1, 0
AIR521ICRU
### start of CM JAWS with identifier PHANTOM ###
30, RMAX
Edge
1, # PAIRED BARS OR JAWS
X
175, 180, 30, 30, 0, 0,
0, 0, 0, 0,
0.521, 0.01, 0, 2,
W521ICRU
######end of all CMs######
############
:Start MC Transport Parameter:
Global ECUT= 0.521
Global PCUT= 0.01
Global SMAX= 10
ESTEPE= 0.25
XIMAX= 0.5
Boundary crossing algorithm= EXACT
Skin depth for BCA= 3
Electron-step algorithm= PRESTA-II
Spin effects= On
Brems angular sampling= KM
Brems cross sections= NIST
```

```
Bound Compton scattering= Norej
Compton cross sections= XCOM
Pair angular sampling= Simple
Pair cross sections= BH
Photoelectron angular sampling= Off
Rayleigh scattering= On
Atomic relaxations= On
Electron impact ionization= Off
Photon cross sections= xcom
Photon cross-sections output= Off
:Stop MC Transport Parameter:
############
```

A.1.2 Radiation transport parameters

The following radiation transport algorithms and parameters were used for all Monte Carlo simulations described in this thesis. Unless stated otherwise, information in this section is drawn from the BEAMnrc user manual [84], where a more comprehensive description can be found.

`Electron step algorithm = PRESTA-II` This transport algorithm controls the lateral and longitudinal corrections to account for elastic scattering in a condensed history step. The most recent (and most accurate) algorithm is `PRESTA-II`, while `PRESTA` allows compatibility with EGS4. It is especially advisable to use `PRESTA-II` for low energy applications, where elastic scattering is not negligible.

`Boundary crossing algorithms = EXACT, Skin depth = 3` BEAMnrc uses condensed history steps to limit the CPU time. When electrons cross the boundary between two regions, this would lead to severe errors. Therefore, a boundary crossing algorithm (BCA) governs the transport of the electrons across region boundaries. The two available options are `PRESTA-I` and `EXACT`. It has been shown that the use of `PRESTA-I` can lead to an overestimation of the dose in certain geometries [110], so that `EXACT` has become the default algorithm. When using `EXACT`, the electron transport is switched to single scattering mode as soon as the electrons are within a specified perpendicular distance from a region boundary. This distance is called skin depth and is given in units of the mean free path length.

`Global ECUT = 0.521, Global PCUT = 0.01` The values `ECUT` and `PCUT` are the globally defined electron and photon cut-off energies in MeV, respectively. They represent the minimum total energy below which no radiation transport takes place. When the energy of a particle falls below this threshold during the simulation, the particle history will be terminated. As a rule of thumb, `ECUT` should be chosen so that the electron range at this energy is less than a third of the smallest dimension in the dose scoring region. [111,112] We set the cut off energies as 0.521 MeV for electrons and 0.01 MeV for photons. In tungsten, the CSDA range of electrons with 10 keV kinetic energy is $7.49 \cdot 10^{-4}$ g/cm^2 according to the NIST database. [93] The density of tungsten is 19.3 g/cm^3, so the electron range is approximately $4 \cdot 10^{-5}$ cm, which is well below the smallest dimension of 0.1 cm used in our simulation. Note that `ECUT` includes the electron rest mass.

`Global SMAX = 10` This option determines the maximum electron step length in cm. Depending in the transport and the boundary crossing algorithm that is used, this value must be adjusted. For use with `EXACT BCA` and `PRESTA-II`, a maximum electron step length of 10 cm is recommended.

It is worth noting that only the maximum step size is globally defined. The actual step size during the simulation is influenced by the boundary crossing algorithm, depending on the position of the particle within the simulation geometry. It will be shortened in the vicinity of an interface and lengthened as the particle propagates away from the interface.

`ESTEPE = 0.25` This parameter determines the maximum energy loss in a condensed history step and thus influences the step width of the condensed history technique. The maximum fractional energy loss per electron step should be 0.25, unless `PRESTA-I` is used.

`Spin effects = On` If this option is turned on, the electron transport algorithm uses elastic scattering cross-sections that take into account relativistic spin effects. Including spin effects leads to more accurate results and is especially important whenever backscatter calculations are needed.

`Brems angular sampling = KM` When a bremsstrahlung photon is created, the photon angle is sampled from a formula by Koch and Motz.[113,114] The user can choose between the entire equation (`KM`) or the leading term only (`Simple`) to be used, which can be sufficient at high energies.

`Brems cross sections = NIST` The total bremsstrahlung cross sections are listed in the PEGS data file. This option determines the differential cross-section for bremsstrahlung interactions. The setting NIST specifies that differential cross sections from the NIST bremsstrahlung cross section data base[115,116] are used, which are recommended for calculating radiative stopping powers by the ICRU.[117] Alternatively, the Bethe-Heitler cross sections[114] with Coulomb corrections above 50 MeV can be used.

`Bound Compton scattering = Norej` This input determines whether binding effects and Doppler broadening are simulated in Compton scattering events. If it is turned `Off`, the differential cross sections are defined by the Klein-Nishina formula.[118] If it is turned `On`, the impulse approximation[119] is added to the Klein-Nishina formula. With the option `Norej`, the total bound Compton cross sections are used, which is the most accurate method.

`Compton cross sections = XCOM` When the bound Compton cross sections are used (`Bound Compton scattering = Norej`), the user can choose a suitable database. In this work, the XCOM database[102] from NIST was used in all simulations.

`Pair angular sampling = Simple` The positron/electron emission angles in a pair production event can be fixed (`Off`) or drawn from an equation derived by Motz et al.[120], either entirely (`KM`) or, as recommended, using the first term only (`Simple`).

`Pair cross sections = BH` The cross sections used for pair production events can either be from Bethe-Heitler (`BH`) or cross sections from NRC which are modified for very low energies (`NRC`).

`Rayleigh scattering = On` For simulations that feature photon energies below 1 MeV, Rayleigh scattering is not negligible and should be turned `On`. The cross sections are drawn from Storm and Israel.[121]

`Atomic relaxations = On` Subsequent to photoelectric or Compton events, atoms can relax to their ground state by emission of fluorescent photons, Auger electrons or Coster-Kronig electrons. For low energy applications, atomic relaxations should be turned `On`. If this option is turned off, no relaxations processes take place, e.g. during a photoelectric event the entire photon energy is transferred to the photoelectron.

`Photoelectron angular sampling = Off` Photoelectrons can inherit the direction of the incident photon by turning this option `Off`. It is possible to use Sauter's formula[122] instead (`On`), but as this is only valid for K-shell photo-absorption, it should be used with caution.

`Photon cross sections = XCOM` The user can choose between the three provided data sets `Storm-Israel`[121], `EPDL` from Lawrence Livermore[123] or `XCOM` from Berger and Hubbell[102], or provide own customized cross section data.

A.2 Mathematica Code

Determination of the edge angle

```
image = Import["... .tif", "Data"];                                    (* edge image *)
position = Array[f, Dimensions[image][[1]]];
For[i = 1, i < Dimensions[image][[1]] + 1, i++,
   linedata = image[[i]];
   average50 = Min[linedata] + (Max[linedata] - Min[linedata])/2;
   line = Interpolation[linedata, InterpolationOrder -> 1];
   sol = FindRoot[Evaluate[line][x] - average50,
            {x, 1, Dimensions[image][[2]]}];
   position[[i]] = x /. sol; ]
sol = FindFit[position, m*x + c, {m, c}, x]
α = Abs[ArcTan[m /. sol]]/Degree                          (* edge angle in degree *)
SamplingDirection = Sign[ArcTan[m /. sol]]
Nav = 1/Tan[α/360*2*π] // N
Nint = Round[1/Tan[Res/360*2*π]]                           (* oversampling factor *)
```

Construction of oversampled edge spread function

```
p = 430/1280                                                          (* pixel pitch *)
s = p/Nint                                                (* subsampling pixel pitch *)
length = Dimensions[image][[2]]*Nint
ESF = Array[f, length];
start = Round[Dimensions[image][[1]]/2] - (Nint + Mod[Nint, 2])/2
If[SamplingDirection < 0,                                          (* interweaving ESF *)
   For[i = 1, i < length + 1, i++,
      ESF[[length + 1 - i]] = image[[start + Mod[i, Nint, 1] - 1,
      Ceiling[i/Nint]]]],
   For[i = 1, i < length + 1, i++,
      ESF[[i]] = image[[start + Nint - Mod[i, Nint, 1] + 1,
      Ceiling[i/Nint]]]]];
```

Finite elemente differentiation

```
LSF = ListConvolve[{1/2, 0, -1/2}, ESF];(* Finite element differentiation *)
LSF = Flatten[Append[Prepend[LSF, 0], 0]];
```

Fast Fourier Transform

```
M = 2 ^ Floor[Log[2,length]]
trunc = Ceiling[(length - M)/2] // N
LSFtrunc = Array[f, M];
For[i = 1, i < M + 1, i++, LSFtrunc[[i]] = LSF[[i + trunc]]] (* truncating to power
of 2 *)
MTF = Array[f, M];
MTF = Abs[Fourier[LSFtrunc, FourierParameters -> {-1, 1}]]; (* Fourier Transform *)
zerofreq = MTF[[1]];
MTF = 1/(zerofreq)*MTF;                                    (* normalizing *)
```

Corrections

```
finite[ξ_] = 1/Sinc[2πξ]                                   (* correction function *)
For[i = 1, i < M + 1, i++, MTF[[i]] = MTF[[i]]*finite[(i - 1)/M]]
Cos[α/360*2π]                                  (* spatial frequency axis scaling *)
```

Result

```
MTFtable = Table[{j/(M*s*Cos[Res/360*2 π]), MTF[[j + 1]]},
{j, 0, Round[1*(M*s*Cos[Res/360*2 π])]}]                   (* detector MTF *)
```

Synthetic edge image

```
r = 0.65;                                                  (* steepness parameter *)
α = 2.2°;                                                  (* edge angle *)
edge = Array[f, 200, 200];                                 (* image (size in px) *)
esf = Piecewise[{{1 - 1/2*Exp[-r*x], x >= 0},
          {1/2*Exp[r*x], x < 0}}];            (* analytical edge spread function *)
For[j = 1, j < Dimensions[edge][[1]] + 1, j++,
   For[i = 1, i < Dimensions[edge][[2]] + 1, i++,
      edge[[j, i]] = esf /. {x -> i - Round[Dimensions[edge][[2]]/2]
                  - j*Tan[α]}
   ]]
```

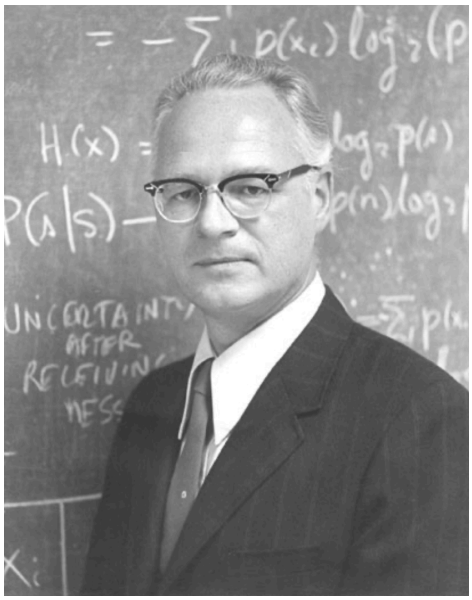

Kurt Rossmann, PhD, started his career at the Kodak Research Laboratories, where he introduced the concept of the modulation transfer function. He later transferred to the Department of Radiology at the University of Chicago, working in close collaboration with radiologists, because he wanted to understand the importance of image quality in clinical situations. [25]